Fall 12-2022

Weak Gravitational Lensing Analysis in Two Superclusters of Galaxies

Sarah B. Rice
University of Maine, sarah.b.rice@maine.edu

WEAK GRAVITATIONAL LENSING ANALYSIS IN TWO SUPERCLUSTERS OF GALAXIES

By

Sarah Beth Rice

B.A. Ohio Wesleyan University, 2010

A DISSERTATION

Submitted in Partial Fulfillment of the

Requirements for the Degree of

Doctor of Philosophy

(in Physics)

The Graduate School

The University of Maine

December 2022

Advisory Committee:

David Batuski, Professor of Physics and Astronomy, Advisor

Neil Comins, Professor of Physics and Astronomy

Charles Hess, Professor of Physics

Andre Khalil, Professor of Chemical and Biomedical Engineering

James McClymer, Associate Professor of Physics

WEAK GRAVITATIONAL LENSING ANALYSIS IN TWO SUPERCLUSTERS OF GALAXIES

By Sarah Beth Rice

Dissertation Advisor: D. J. Batuski

An Abstract of the Dissertation Presented
in Partial Fulfillment of the Requirements for the
Degree of Doctor of Philosophy
(in Physics)
December 2022

Observations of the Universe on very large scales have shown it to be filled with galaxy clusters and superclusters connected by walls and filaments of galaxies, with vast areas mostly devoid of luminous matter separating them. It is widely accepted that the amount of luminous matter does not provide the mass needed to hold galaxies and galaxy clusters together, and the nature of the missing "dark matter" is one of the most prominent astrophysical mysteries today. Since dark matter interacts with luminous matter gravitationally, it stands to reason that dark matter might organize itself in a similar manner to luminous matter, forming clumps and voids with filaments connecting them, but while there have been simulations showing that this is likely true, the observational efforts looking for dark matter filaments have been few and contradictory.

I present a weak gravitational lensing analysis of two particularly overdense galaxy superclusters, The Aquarius Supercluster (ASC) and the Microscopium Supercluster (MSC), in order to probe the mass distribution in these regions. Observations were performed on the DECam mounted on the Victor Blanco 4-m Telescope at the Cerro Tololo Inter-American Observatory (CTIO) in Chile. The image data was processed by the DECam Pipeline and then reduced with Source Extractor software. The images were broken into data broken into grid of varying mesh sizes, and two different maps of lensing

were created for each mesh size, with one being weighted by the frequency of objects with a given orientation, and the other weighted by the ellipticities of the objects with a given orientation. In order to interpret the lensing maps, model maps of the expected gravitational shear from the superclusters were created for comparison. The results show that the data matches the model much better for the MSC than the ASC. With a confidence level of 1-3σ for the majority of maps, it seems likely that we are detecting at least some weak gravitational lensing for the ASC. The higher levels of 1-8σ for the maps of the MSC region are strong evidence of gravitational lensing in this field. The difference between the two regions is suspected to be likely an effect of other clusters in the field of view. While the sky offers a fairly clean view of the MSC with only a couple of identified background clusters, the ASC region is cluttered with various other clusters. The results neither confirm nor preclude the existence of a filamentary structure of inter-cluster matter, but do suggest that any such filaments would likely be significantly less massive than the clusters themselves, which appear to dominate the region.

ACKNOWLEDGEMENTS

TABLE OF CONTENTS

LIST OF TABLES

LIST OF FIGURES

CHAPTER 1

INTRODUCTION

1.1 Galaxies and Clusters

The study of the large-scale structure of the Universe began nearly a century ago. In the early 20$^{\text{th}}$ century, scientists were locked in a debate that had been going since the mid-sixteenth century about whether the 'spiral nebulae' observed in space were clouds within the Milky Way, or separate 'island universes' - galaxies - themselves. The debate was settled by Edwin Hubble, who tackled the question by making detailed observations of the Andromeda galaxy, the closest neighboring large galaxy to our own. In 1919, he began studying it, observing the stars within. A few years later, he was able to use the variable stars he found inside it to calculate the distance to the Andromeda galaxy, proving that it is well beyond the borders of the Milky Way (Hubble, 1929b). This discovery opened the door to the study of extragalactic objects and distances.

Even before the debate about the nature of the 'spiral nebulae' was settled, others had argued in favor them being 'island universes,' or other galaxies akin to the Milky Way. One proponent of this theory was Vesto Slipher, who, along with some other scientists of the time, used spectroscopy to measure the velocities of many other galaxies. He noted that they were moving much faster than the stars in our galaxy, and thus were likely to be separate galaxies, since they could not be gravitationally bound to our galaxy at those speeds (Slipher, 1917). While doing this work, he noted that these 'nebulae' were also not evenly distributed across our sky, mentioning that they often appeared bunched together in clusters. He was not the first to notice that galaxies appeared clustered together on the sky, as that had been noted over a century prior by William Herschel (Herschel, 1786). However, Slipher and Hubble later combined the results of their research, and discovered that the farther away galaxies are, the faster they appeared to be receding, so they may have been the first to look at the distribution of galaxies in three dimensions. Hubble

published the resulting law,

$$v_r = H_0 r \tag{1.1}$$

in 1929, where v_r is the recession velocity, r is distance, and H_0 is "Hubble's constant," which relates those two variables (Hubble, 1929a). Since recession velocity cannot be directly measured, it must be calculated from a galaxy's redshift. For relatively close galaxies ($z << 0.1$), inserting cz is a reasonable approximation, such that

$$r = \frac{cz}{H_0}. \tag{1.2}$$

However, for more distant galaxies, the value provided by this approximation becomes too large, and another model must be used. One such model, found by incorporating the Doppler effect, yields

$$r = \frac{c(z+1)^2 - 1}{H_0(z+1)^2 + 1} \tag{1.3}$$

(Carroll and Ostlie, 2007). Cosmology provides another model in which the assumption of a flat, exponentially expanding universe dominated by the cosmological constant Λ yields

$$r = \frac{cz}{H_0(1+z)} \tag{1.4}$$

(Ryden, 2003).

In 1953, Gérard de Vaucouleurs noticed that galaxies around the Virgo cluster were confined to a supercluster disk, which he called a 'supergalaxy' (de Vaucouleurs, 1953). George Abell took this a step further, when in 1958 he published a method of categorizing galaxy clusters and a cluster catalog. He defined galaxy clusters as containing "at least fifty members that are not more than 2 mag. fainter than the third brightest member" within a radius of $1.5h^{-1}$ Mpc of the cluster center (Abell, 1958). Most of the galaxy clusters we know of today contain hundreds of galaxies within a diameter of 2 to 10 Mpc, are gravitationally bound and generally virialized, meaning that the size of the cluster is relatively stable, although the galaxies within are moving around. Abell noticed that the galaxy clusters that he studied also, in turn, had a tendency to cluster, and in 1961 he

released a catalog of these 'second-order clusters' or 'superclusters' (Abell, 1961). However, there remained skeptics, such as Zwicky, who were unconvinced of higher-order clustering, and the matter was not truly settled until Jaan Einasto and his colleagues provided redshift data for several superclusters, proving conclusively that the galaxy clusters did in fact cluster together (Gregory and Thompson, 1978; Einasto et al., 1980). Gregory & Thompson, in their 1978 paper examining the Coma/A1367 supercluster, concluded that it was likely that every rich cluster was part of a larger supercluster.

1.2 Dark Matter

In the 1930s, astrophysicists started looking more critically at the gravity that binds objects into systems. Jan Oort measured the motions of the stars in the Milky Way and published his results in 1932, and noted that the mass of the galactic plane must be greater than the total mass of visible material. He was the the first to find evidence for "dark matter," as he called it (Oort, 1932), although he felt that this matter could be explained by dim or hidden stars, and that better observations of the Milky Way could uncover these. In 1936, Sinclair Smith published a study on the Virgo cluster, where he argued in favor of it being a gravitationally bound structure (Smith, 1936). A year later, Fritz Zwicky published a dynamical analysis of the Coma cluster. He was the first to apply the virial theorem, which relates kinetic energy to potential energy, to a galaxy cluster, and in doing so, he discovered that there was not enough mass within the galaxies to hold the cluster together (Zwicky, 1937), and he is often credited with coining the term "dark matter" since, unlike Oort, he realized that the missing mass was too great to simply be overlooked stars, and that some other mysterious material or phenomenon must be responsible.

In the 1970s, the dark matter mystery deepened. Vera Rubin and Kent Ford published a paper about the rotation of the Andromeda galaxy (M31) in 1970, in which they pointed out that the orbital velocity of the galaxy did not decrease with radius as would be expected (Rubin and Ford, 1970). In 1972, a paper by Rood et al. made the

startling estimation that there was an "unseen mass about 7 times as large as the galaxies we see," which means that dark matter makes up roughly 85% of all matter in the Universe (Rood et al., 1972). In 1973, Jeremiah Ostriker and James Peebles provided a theoretical framework for Rubin's observations in a paper describing the results of a simulation they had done, which showed that flattened disk galaxies would not be stable without the existence of a large, massive halo (Ostriker and Peebles, 1973). Rubin and her colleagues followed up on their results by taking the spectra of 60 more spiral galaxies throughout the next decade and half, and discovered the same lack of decreasing velocities with increasing radius as they had found for M31, which they attributed to dark matter (Rubin et al., 1980, 1982, 1985).

1.3   Large Scale Structure

While the existence of clusters and superclusters of galaxies has been known for some time, a full look at the large-scale structure of the Universe didn't really get underway until the 1980s. In 1981, Kirshner at al. first noticed a large empty area in the constellation Boötes, seemingly almost devoid of galaxies (Kirshner et al., 1981). In 1982, Neta Bahcall and Raymond Soneira followed up on this with a study that found this void was surrounded by the Hercules and Corona Borealis superclusters, and suggested that voids in general may be bordered by overdense galaxy regions (Bahcall and Soneira, 1982). Batuski and Burns published a study in 1985 that reported the finding of a 300 h^{-1} Mpc filament of galaxies and galaxy clusters that included the Perseus-Pisces supercluster (Batuski and Burns, 1985). In 1986, Brent Tully published a paper in which he noticed that our own Virgo Supercluster was part of a much larger structure, which he called the Pisces-Cetus Supercluster Complex (Tully, 1986). In 1989, Margaret Geller and John Huchra released a study of the second data release from the Center for Astrophysics Redshift Survey, in which they uncovered a large filament of galaxies, which they called the "Great Wall" (Geller and Huchra, 1989). In 1992, Smoot et al. published a paper announcing that they

4

had used the data from the Cosmic Background Explorer to find the anisotropies in the cosmic microwave background radiation that were the seeds of large-scale structure (Smoot et al., 1992). The Two-degree-Field Galaxy Redshift Survey (2dFGRS) began in 1997, and results were published by Colless et al. in 2001 which revealed a network of filaments, walls, and voids in the nearby Universe (Colless et al., 2001). Numerous other large structures have been discovered since, some of the biggest spanning billions of lightyears across. The largest of these is likely the Hercules-Corona Borealis Great Wall, which spans a whopping 10 billion lightyears (Horváth et al., 2014; Horvath et al., 2020).

Scientists have also been able to model the formation of the cosmic web structure though simulations. These simulations show how the small anisotropies in the early Universe eventually evolve into the large-scale cosmic web structure we see today, using the ΛCDM model of the Universe. CDM stands for "cold dark matter," which refers to dark matter made of slowly moving particles, allowing them to clump together. Λ denotes the cosmological constant associated with dark energy, a phenomenon driving the acceleration of the expansion of the Universe. Like dark matter, dark energy is another mysterious unidentified component of our Universe, despite current estimates that it makes up $\sim 70\%$ of the total energy in the current observable Universe.

One of the most famous of these simulations is the Millennium Run, which was first conducted in 2005 by an international group of physicists known as the Virgo Consortium (Springel et al., 2005). This first run was, at the time, the largest simulation ever done about the formation of structure. It followed over 10 billion particles to model dark matter distribution in a cube of about 2 billion lightyears, and ended up showing the creation and evolution of roughly 10 million galaxies. They ran a second simulation in 2008, called the Millennium-II Simulation, in which they looked at cube of only 400 million lightyears, but with 125 times the mass resolution of the original simulation, which allowed them to represent observed galaxy populations more accurately (Boylan-Kolchin et al., 2009). In 2010, a third simulation was performed, called Millennium XXL (Angulo et al., 2012). This

modeled a cube of about 13 billion lightyears containing more than 300 billion particles, with each particle representing much more mass than before. The detailed model that resulted has helped cosmologists study galaxy distribution and dark matter halos, and see how the very rare and massive structures in our Universe may have formed.

The Millennium project is still being worked on today. However, they are not the only ones conducting such large simulations. In 2014, another noteworthy simulation called the Illustris project looked at modeling structure formation in a more detailed way by looking at a smaller volume with fewer particles, but attempting to treat the flow of gases more realistically (Vogelsberger et al., 2014; Genel et al., 2014). This allowed them a detailed examination of the gas content in the Universe, star and galaxy formation, how gas may affect the structure of dark matter, and how these structures may evolve over time.

1.4   Studying Dark Matter in Superclusters

Until recently, galaxy clusters were thought to be largest gravitationally bound structures in the Universe, because although superclusters of galaxies are the largest and most massive structures in the Universe, most of them have not been found to be gravitationally bound. However, evidence has been presented in recent years that particularly overdense galaxy superclusters may also hold the possibility of being gravitationally bound.

The most famous example of a gravitationally bound supercluster is the Shapley Supercluster (SSC). Numerous studies (Bardelli et al., 1993; Reisenegger et al., 2000; Proust et al., 2006; Muñoz and Loeb, 2008; Pearson and Batuski, 2013) have demonstrated significant bound structure within. The Corona Borealis Supercluster (CSC) is another candidate for containing bound structure (Postman et al., 1988; Small et al., 1998; Kopylova and Kopylov, 1998; Batiste and Batuski, 2013). The Aquarius Supercluster (ASC) and the Microscopium Supercluster (MSC) may also each be dense enough to be one of the few gravitationally bound superclusters (Batuski et al., 1995; Batiste, 2014).

Dark matter is one of the most prominent astrophysical mysteries today. The evidence for dark matter is found in the gravity holding individual galaxies together and in the gravity holding clusters of galaxies together, but it is yet unknown what dark matter might actually be. For this reason, it is important to characterize the behavior of both luminous and dark matter on many scales, in order to consider what effects the distribution of dark matter has on the distribution and morphological evolution of luminous matter. The Universe is known to be filled with "clumps and voids" in terms of luminous matter; in other words, luminous matter has been found to largely be confined to galaxy clusters and superclusters connected by walls and filaments of galaxies, with vast areas mostly devoid of luminous matter separating them. It is, therefore, not unreasonable to question whether dark matter might form similar filamentary structures. The presence or absence of dark matter filaments can be used to place constraints on theories of formation, and the mass fraction contained in filaments can be used to test mass-to-light ratios (Gray et al., 2002).

While there have been a number of works showing that galaxies themselves form walls and filaments between clusters, and simulations showing that dark matter ought to do the same, the observational efforts looking for dark matter filaments have been few and contradictory (Gray et al., 2002; Dietrich et al., 2005; Heymans et al., 2008). However, a 2013 study by Batiste & Batuski found evidence that the CSC is undergoing collapse, whereas the 2013 N-Body simulation by Pearson & Batuski indicates that there was not enough matter within the individual clusters for this to occur, which suggests the presence of a significant amount of inter-cluster dark matter. A 2014 paper by Pearson, Batiste, and Batuski suggests that the total mass of the CSC is likely around $1x10^{16}h^{-1}M_\odot$, while the masses of the clusters account for only around $6x10^{15}h^{-1}M_\odot$, leaving inter-cluster matter to make up for the remaining $4x10^{15}h^{-1}M_\odot$ (Pearson et al., 2014). Since the ASC and MSC are similar to the CSC in spatial density, these two superclusters provide excellent environments in which to look for this inter-cluster dark matter. There are three main ways of studying dark matter: by looking at x-ray emissions from hot gas trapped in
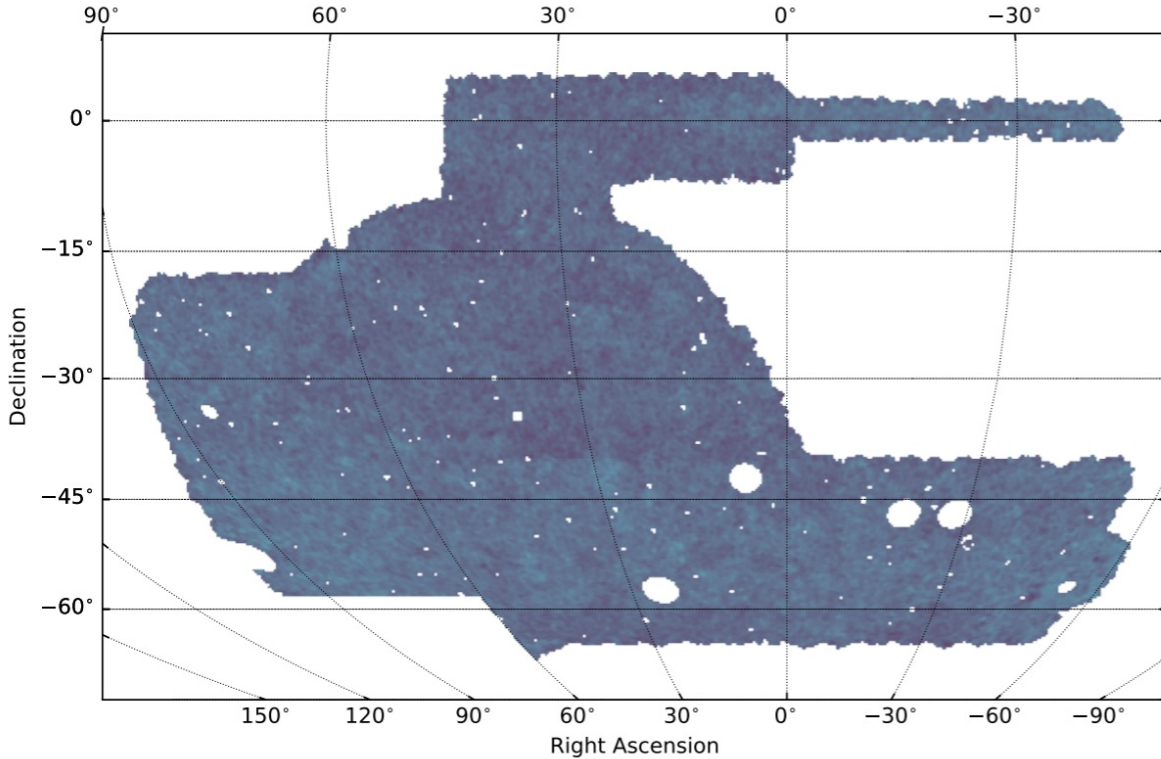
Figure 1.1: The region of sky covered by the Dark Energy Survey (Gatti et al., 2021).

clusters by dark matter, by looking at velocities of galaxies within a cluster, or by looking at gravitational lensing of light from background galaxies. It is this last approach that we take here.

1.5 Weak Lensing

Gravitational lensing is the deflection of photons from a background source as they pass by a clump of foreground matter. Due to this effect, the distant objects can appear to have a different position, size, or shape than they would if the photons had passed through a homogeneous universe. Deviations in position can only be determined in cases where the source's actual position is known, which sometimes occurs in cases of a strong lensing system that creates multiple images of the same object (Walsh et al., 1979; Gatti et al., 2021). Similarly, the distortion of the shape of a single galaxy would be equally difficult to identify. However, galaxy orientations should be random, and thus the orientations of large

numbers of galaxies should be isotropic. When these background galaxies are lensed by foreground matter, it induces an ellipticity in a preferred direction, called a "shear" and denoted by γ, and a change in apparent size, termed "convergence" and denoted by κ. The distortion δ is then

$$\delta = \frac{1 - q_c^2}{1 + q_c^2} \tag{1.5}$$

where

$$q_c = \frac{1 - \kappa - \gamma}{1 - \kappa + \gamma} \tag{1.6}$$

and is equal to the ellipticity of the image of a small circular source (Miralda-Escudé, 1991).

Thus by examining correlations of galaxy ellipticities, lensing from mass concentrations in the foreground can be inferred (Bartelmann and Schneider, 2001). The Dark Energy Survey (DES) Collaboration took this approach to create a dark matter mass map of the large area of sky they observed with the Dark Energy Camera (DECam) on the 4-m Blanco Telescope at the Cerro Tololo Inter-American Observatory (CTIO) in Chile (Jeffrey et al., 2021). However, the region of sky covered by the DES did not include the ASC or MSC (see Figure 1.1), and more time was spent imaging the ASC and MSC for this project than the DES Collaboration was able to devote to any equally-sized field, allowing more faint, distant background galaxies to be identified in our images.

This work is organized as follows: Chapter 2 presents a summary of previous work on the ASC and MSC. Chapter 3 describes the data collection program. Chapter 4 describes the data process and weak lensing analysis. Chapter 5 presents the model lensing, comparison with data, and statistical interpretation of the results. Finally, Chapter 6 draws conclusions and describes future work that may be undertaken to advance this work further.

CHAPTER 2

THE SUPERCLUSTERS

2.1   The Aquarius Supercluster

The Aquarius Supercluster (ASC) was first cataloged by George Abell as "SC 16" in his 1961 publication about second-order clustering (Abell, 1961). Due to it being a very rich supercluster, it was later targeted by Ciardullo et al. for a redshift survey, which showed a surprisingly high density of rich clusters in that area of the sky (Ciardullo et al., 1985). The 23 clusters in the $5° \times 5°$ region were found to have an almost uniform redshift distribution from $0.08 < z < 0.24$. The authors speculated that these clusters were not all part of one structure, but were in fact multiple structures at varying distances that happened to overlap on our sky.

In 1999, Batuski et al. followed up on this work with a more detailed redshift survey of rich galaxy clusters in the region. They found that the Aquarius supercluster was a collection of 14 clusters from $0.08 < z < 0.12$ with a spatial density of $20\bar{\rho}$, where $\bar{\rho}$ is the average spatial density of rich Abell clusters, and contained a "knot" of six clusters at $z \approx 0.11$, five of which were so closely spaced that the overdensity reached a remarkable $150\bar{\rho}$. (Batuski et al., 1999). This extremely high density suggested that the ASC might be gravitationally bound and undergoing collapse. The authors were the first to estimate the mass of the knotted structure, finding a lower limit of $6 \times 10^{15} h^{-1} M_\odot$. For comparison, the average galaxy cluster has a mass in the range of $1 \times 10^{14} h^{-1} M_\odot$ to $1 \times 10^{15} h^{-1} M_\odot$.

In 2002, Caretta et al. investigated further, using redshift measurements to study the distribution of clusters in a $10° \times 6°$ area in the Aquarius region. They were able to distinguish two separate superclusters in the region, a foreground one containing 5 clusters at $z \sim 0.086$, and a denser background one (which we now call the ASC) containing 14 clusters at $z \sim 0.11$. They also remarked on the high overdensity of the latter supercluster,

estimating a lower limit of $\sim 2 \times 10^{16} h^{-1} M_{\odot}$ for the mass. They also noted that it might be connected to a 40 h^{-1} Mpc filament extending from $z \sim 0.11$ to 0.14 (Caretta et al., 2002).

In 2004, Smith et al. performed a spectroscopic study on ~ 4000 galaxies in a $\sim 6.2°$ field in the Aquarius region. Their work also showed two separate superclusters overlapping in the sky, supporting the findings of Caretta et al., and further remarked that both superclusters seemed to have very high overdensities, similar to the SSC and CSC (Smith et al., 2004). They found a lower limit on the mass of each supercluster by assuming a dark matter halo around each cluster according to a density profile described in a 1997 paper by Navarro, Frenk, and White (Navarro et al., 1997), then calculating the mass in a sphere around each cluster so that the mean density inside the sphere equals 200 times the average density of the Universe, and summing the results. Then an upper limit for the area was found by integrating the Navarro, Frenk, and White profile over the whole region. The foreground supercluster was found to have a mass between $3.2 \times 10^{15} h^{-1} M_{\odot}$ and $8.3 \times 10^{16} h^{-1} M_{\odot}$, corresponding to an overdensity of $13\bar{\rho}$ and $330\bar{\rho}$. The background cluster was found to have a mass between $4.5 \times 10^{15} h^{-1} M_{\odot}$ and $8.3 \times 10^{16} h^{-1} M_{\odot}$, which corresponds to an overdensity of $17\bar{\rho}$ and $330\bar{\rho}$.

Pearson & Batuski published a paper in 2013 that examined the cores of four superclusters, including the ASC. They employed a method described by a 1996 paper by Carlberg et al. which uses galaxy redshifts to calculate the virial mass of a cluster to estimate mass of each of the clusters comprising the core of the supercluster (Carlberg et al., 1996). They then ran a simulation designed to assess the likelihood that any clusters were gravitationally bound based on those masses, finding that only A2541 and A2546 were likely to be a bound pair (Pearson and Batuski, 2013). However, in 2014, an observational analysis of the clusters was presented by Batiste which suggested there may be more extensive bound structure than what was predicted by Pearson & Batuski (Batiste, 2014). A possible explanation for the discrepancy between the two studies was that there may be

a significant amount of inter-cluster matter in the region, which would increase the likelihood of there being extensive bound structure.

2.2   The Microscopium Supercluster

The Microscopium Supercluster (MSC) was first identified in a 1993 paper by Zucca et al. as containing six $R \geq 1$ clusters (Zucca et al., 1993). A 1996 paper by Katgert et al. provided redshifts for each of the clusters and found them to be in the range of $0.81 \leq z \leq 0.88$, thus indicating that this was a structure of significant overdensity (Katgert et al., 1996). Batuski et al. (1999) examined this further, finding the overdensity of the supercluster to be $130\bar{\rho}$, making it yet another of the densest known superclusters in the Universe. By taking redshift values from K96 and using the velocity dispersions to estimate the masses of the clusters from the virial theorem, they were able to calculate a lower limit of $\sim 4 \times 10^{15} \ h^{-1} \ M_\odot$ for the mass of the MSC, but due to the sparse data for the region at the time, no further estimate of the mass was made.

As with the ASC, the MSC was also examined by Pearson & Batuski (2013) and Batiste (2014). While the analysis by Pearson & Batuski found that only clusters A3695 and A3696 were likely to be gravitationally bound, Batiste found evidence to support the possibility of A3696, A3677, and A3705 being bound to the structure as well, which once again raised the question of a possible inter-cluster matter component to account for the discrepancy in results (Pearson and Batuski, 2013; Batiste, 2014).

CHAPTER 3
DATA COLLECTION

In order to investigate the question of a significant inter-cluster matter component in both the ASC and MSC, a weak lensing approach was decided upon to probe the mass distribution in those regions. This requires an analysis of distant background galaxies of high apparent magnitude. Although galaxies display a range of ellipticities against the sky, their orientations should generally be distributed isotropically. However, when photons from a background source pass by a clump of foreground matter, the gravity can deflect the photons such that the objects appear slightly systematically elongated in some particular direction. This weak gravitational lensing shear can thus be used to identify regions of dense matter. Limited observational data has been taken on the ASC and MSC regions prior to this work. Many of those (Katgert et al., 1996; Batuski et al., 1999; Caretta et al., 2002; Smith et al., 2004) were spectroscopic studies and rather than photometric, and the photometric study by Batiste (2014) covered only portions of the clusters and did not reach a depth great enough for a weak lensing analysis, as the author had use of only a 1-m telescope with a small field of view. Therefore, an observing program was undertaken to image the wide and deep field of view needed for an examination of background objects behind the core of each supercluster.

Observations were performed on the DECam, a 62-CCD array (59.5 of which were functional) each with 2048×4096 pixels, built to carry out the Dark Energy Survey. The DECam was mounted on the Victor Blanco 4-m Telescope at the Cerro Tololo Inter-American Observatory (CTIO) in Chile. The array has a total of 520 megapixels covering a 2.7 deg^2 area. The observing program was initially conceived to cover an approximately $3° \times 3°$ area of the sky for each supercluster, to a depth of red magnitude $r \sim 26$. This would involve observing approximately four fields per supercluster, for two hours of exposure per field. The sixteen total hours required for observing would thus have
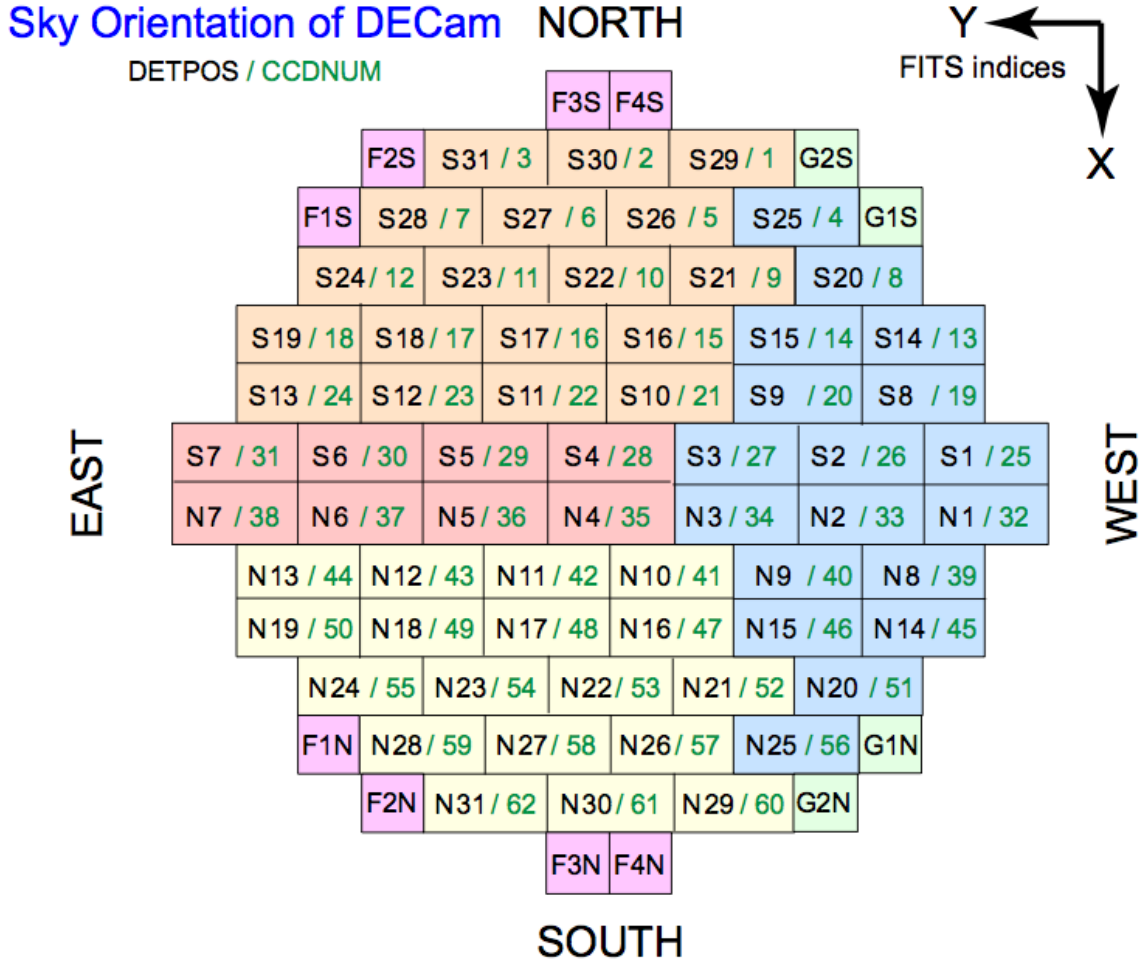
Figure 3.1: The layout of the DECam's CCD array.

taken four to six nights to cover, depending on weather conditions. However, due to limited
time on the telescope granted by the telescope allocation committee, the observing
program was redesigned to uniformly cover only a 3 deg^2 area at the projected core of each
supercluster. To fill in the gaps between CCDs (see Figure 3.3), a dithering pattern was
designed so that camera targeted 21 slightly different positions for each cluster, moving
approximately 4 seconds of right ascension between each position and 67.3 arcseconds of
declination every three positions. Two 160 second exposures in the r filter were taken at
each position. A similar though shorter program was designed to take exposures in the g
filter with remaining time so that color studies of the galaxies could be done. Assuming

14
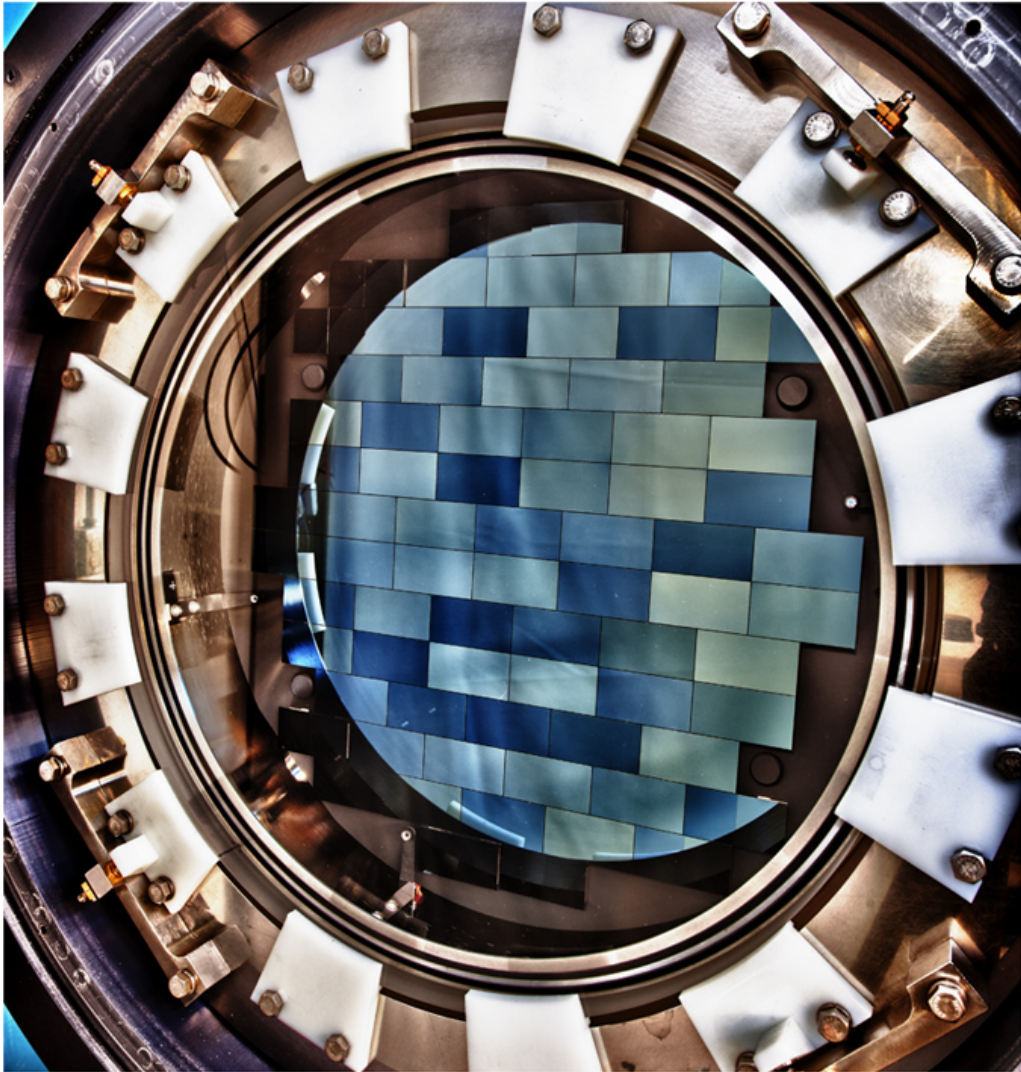
Figure 3.2: The DECam CCD array (DES, 2021).

that time would be granted in whole-night increments, telescope time was requested for July 2015, since our targeted areas would be closest to the meridian during mid-nights of this part of the year, but instead, the first halves of two nights were granted in August. On August 19th, unusable time during the earliest part of the night was able to be traded with another team in exchange for some of their time on a subsequent night. Our observations began a little later as our targets reached a height above the horizon such that the effects of the atmosphere on the light coming through would be reasonably low. During this first
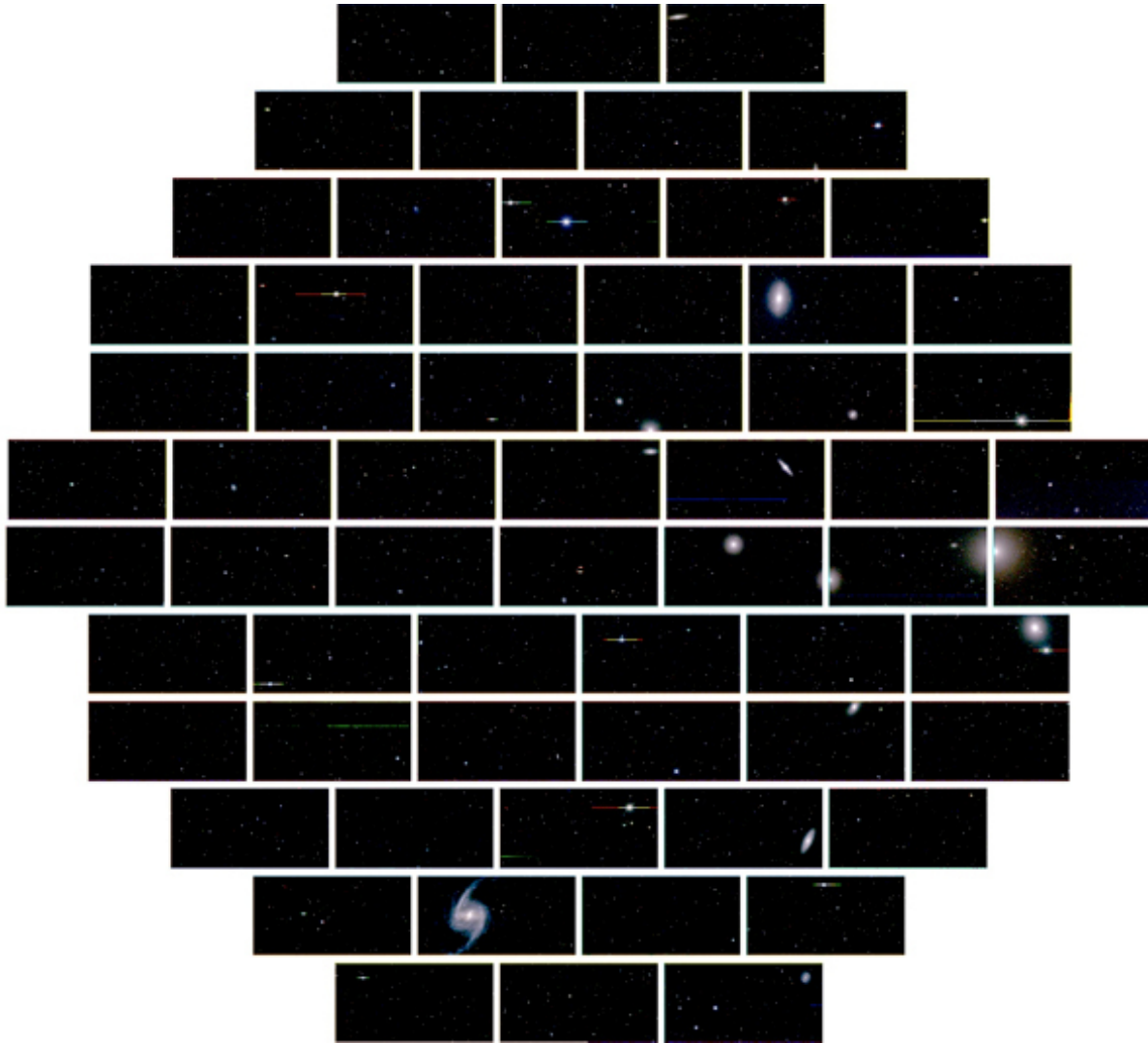
Figure 3.3: Spaces between the CCDs make it necessary to dither in order to fill in the gaps. (Image from First Light of DECam (DES, 2021).

night of observing, all of the data for the MSC and some of the data for the ASC was taken in the r filter. Unfortunately, no data was able to be taken on the second awarded night, August 20th, due to weather conditions. However, the observing team that time was traded with was able to complete the rest of the ASC observations in r on the night of August 24th. Due to the loss of the second night due to weather, no observations were able to be made with the g filter, and thus no information about the colors of the galaxies could be obtained from the gathered data.
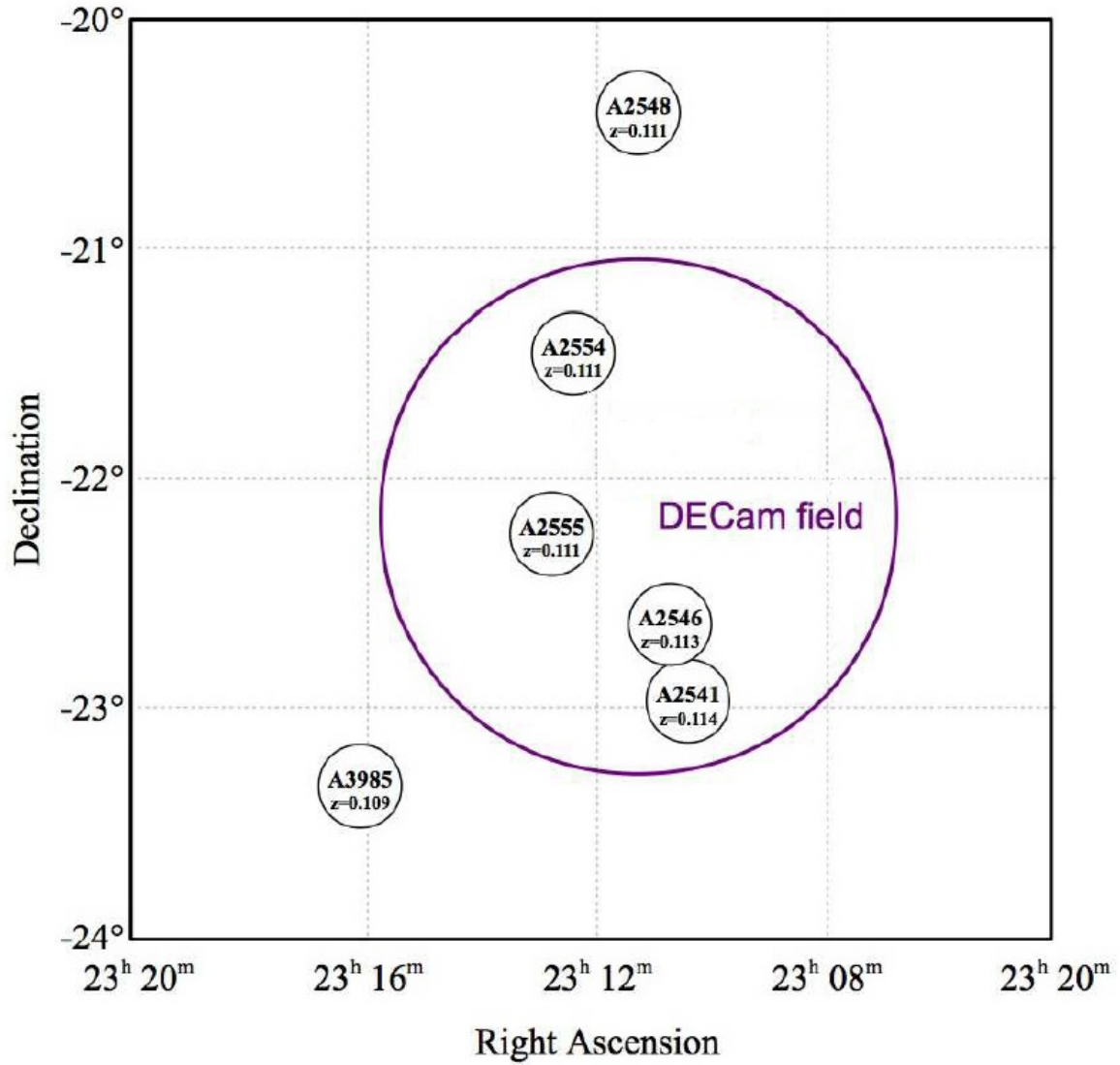
Figure 3.4: The targeted area of the ASC (Favia et al., 2014).
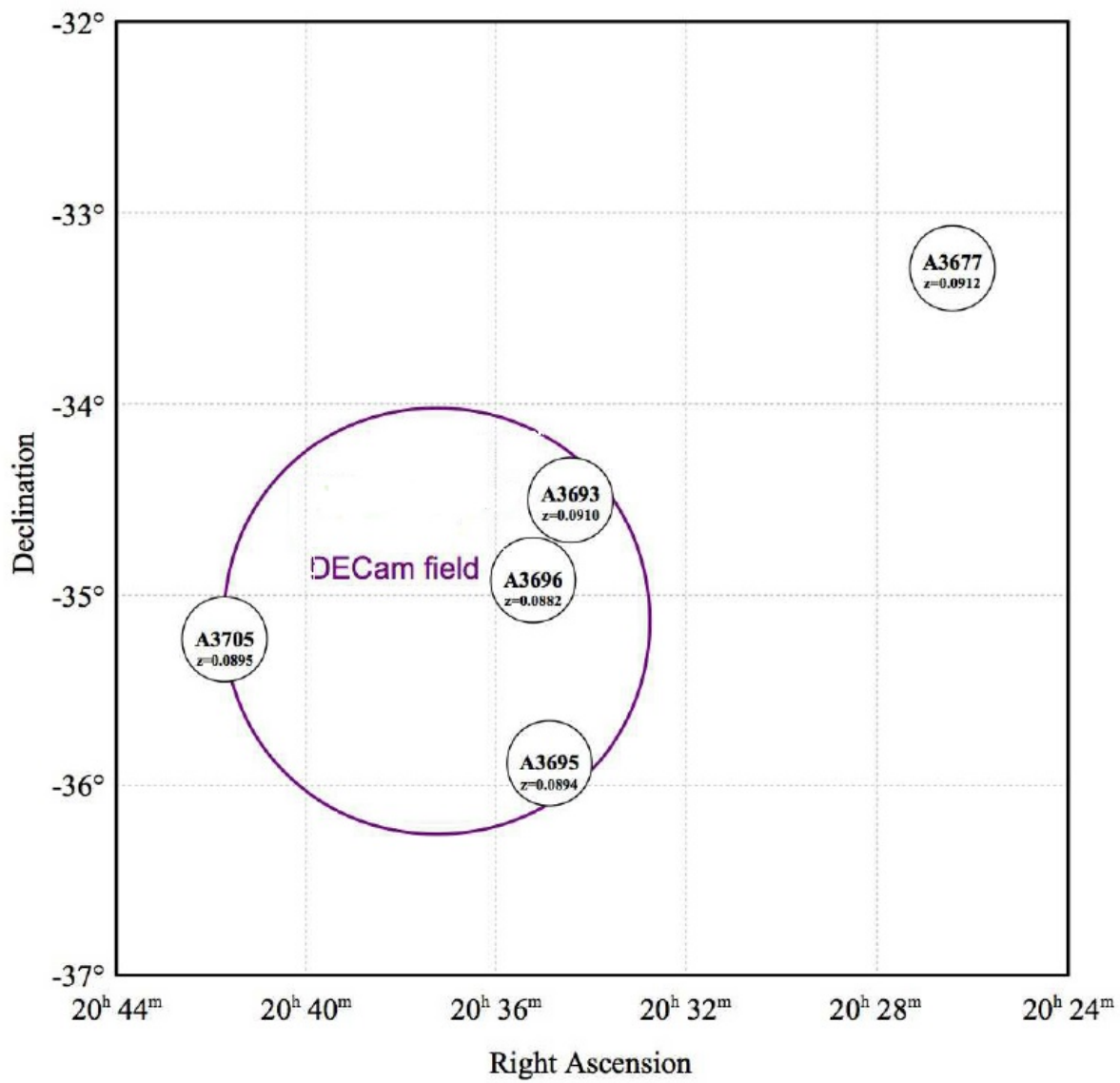
Figure 3.5: The targeted area of the MSC (Favia et al., 2014).

CHAPTER 4

DATA PROCESSING

Once the data was taken, it was necessary to reduce the data images before any weak lensing analysis can be performed. This process is carried out across several different stages.

4.1 Pipeline

The image data was first processed by the DECam Pipeline. The pipeline performs a number of standard photometric corrections (NOIRLab, 2014; Valdes et al., 2014; Morganson et al., 2018) , many of which are considered standard for CCD cameras:

1. Each CCD on the DECam has two amplifiers which process the signal output from each pixel, which can result in a cross-talk effect where the signal level read by one amplifier affects the value read by the other, which must be accounted for.

2. Corrections to the signal from the CCD camera are performed. These include a bias correction, which accounts for the noise signal reported by each pixel in the absence of any light, and a flat-field correction which accounts for the variations in responsiveness of different pixels. Electronic calibration bias uses covered parts of the CCDs to measure and correct any offset between the data, bias, and field images.

3. Any stars for which the pixels have become oversaturated and bled onto neighboring pixels are identified, as well as any bad pixels or cosmic rays, and these are masked and interpolated away.

4. Sky pattern removal involves removing the camera reflection and any other gradient patterns (for example, from the Moon) in order to make the sky background in the image uniform on large scales.

5. Astrometric calibration consists of using the Two Micron All-Sky Survey (2MASS) astrometric reference catalog (Skrutskie et al., 2006) to fit the world coordinate system to the image, thus assigning each pixel a right ascension and declination value, and the USNO-B1 catalog (Monet et al., 2003) is used to fit object brightness values to the standard magnitude system.

6. Pixel area correction and remapping is implemented to correct for any variations in pixel size on the sky and ensure that images can be lined up for stacking.

7. In the multi-exposure transient masking phase, the pipeline identifies transient objects (such as cosmic rays, satellites, asteroids, etc. - essentially anything significantly different in one image than in others of the same region) and masks them.

8. Exposures of the same area and taken on the same night are then aligned and added together to produce a final stacked image.

Since all of the data for the MSC was taken on the first observing night, a completely processed and stacked image was provided by the pipeline. Since the data for ASC was split across two nights, a stacked image was provided for each night, and Image Reduction and Analysis Facility (IRAF) software (Tody, 1986) was used to stack the two images into a single final image.

4.2 Object Identification

Once a stacked image for each supercluster was obtained, the next phase was to identify and classify each object contained within the field, which was done with Source Extractor software. SExtractor is a reduction software that builds a catalog of objects from astronomical images and is particularly suited for large-scale galaxy surveys (Institut d'Astrophysique de Paris, 2017), making it an excellent choice for our needs. However, the output is heavily dependent on the user-specified settings, with poor settings leading to

poor detection results (Holwerda, 2005). The series of steps performed by the SExtractor algorithm are as follows:

1. The program begins by estimating the background signal and RMS noise so that it can detect differences from this background level to identify objects and measure their fluxes. To this end, it breaks the image up into a grid, the size of which is user-specified, and for each piece, it calculates the mean and standard deviation σ of the pixels. Then it discards the most deviant pixels and repeats the process until all remaining pixels are within $\pm 3\sigma$ of the mean. The choice of background size is thus important, since too small a size may lead to an object dominating the area and thus causing the background estimate to be influenced by the object flux, while too large of an area may lead to variations on a small scale not being appropriately accounted for. A manual draft by E. Bertin suggests that a width of 32 to 256 pixels is appropriate for most images, and to ensure that the parameter $BACK\_MESH$ is sufficiently larger than the objects in the fields of view, a value of 175 pixels was selected. The program also has the option to smooth the background to reduce the influence of bright extended objects. The manual-recommended value of 3 was chosen for the $BACK\_FILTERSIZE$ setting (Bertin, 2006).

2. The next step taken by SExtractor is to detect objects. A set of pixels is considered to be an object if a user-specified minimum number of them are adjacent and all above a user-specified detection threshold. The choice of detection threshold is important, since too low a value will result in false detections from noise and too high a value will result in a failure to detect dim objects. After testing several values, it was determined that a value of 3 set for $DETECT\_THRESH$ gave the best results, meaning that an object must be at least 3σ above the background level in order to be detected. It is generally suggested to keep the value of the minimum area small and to allow the detection threshold to be the major factor in influencing the program's sensitivity (Bertin, 2006; Casey, 2006), but it was also important for this work to

have a large enough object area to determine shape and orientation, so a

DETECT_MINAREA of 8 pixels was selected.

3. After detecting objects, SExtractor attempts to deblend overlapping objects. Once again, there are two user-specified parameters that determine how well the program will perform this function. *DEBLEND_NTHRESH* sets the number of levels, spaced exponentially, between the detection threshold and the maximum count in an identified object, so that SExtractor will flag two bright areas with an area of lower flux between them. *DEBLEND_MINCONT* sets the minimum ratio of the number of counts each branch must have relative to the flux of the combined system for both to count as distinct objects. After testing various combinations, a value of 8 for *DEBLEND_NTHRESH* and a value of 0.0005 for *DEBLEND_MINCONT* were determined to give the best results upon visual inspection.

4. SExtractor then determines the shape and position of identified objects, primarily using Kron apertures (Kron, 1980) to determine the geometric parameters. It also cleans the detections by reconsidering whether objects would have been detected if neighboring objects had been masked.

5. The program then performs photometry, measuring the brightness of each object according to the user-specified mode. The five approaches available in SExtractor are isophotal, isophotal-corrected, automatic, best estimate, and aperture. The automatic mode was selected for this work, in which a flexible elliptical aperture known as a Kron radius (Kron, 1980) is defined around each object and the flux within is measured.

6. SExtractor then uses a neural network to examine the "level of fuzziness" of each object and determine whether it is more star-like or galaxy-like, assigning it a *STAR_CLASS* value between 0 and 1, where this is the estimated probability of the object being a star.

22

7. Finally, the program produces an output catalog of objects and their measured parameters as well as a 'check' image that shows the results of the processing and the determined apertures around each object that the user can examine to verify that the settings and detections seem appropriate.

4.3   Data Cuts and Deconvolution

In order to infer the presence of weak gravitational lensing from measured ellipticities, the images must be corrected for distortions from effects such as the point spread function of the atmosphere, telescope, and detector, so that the remaining correlations in the ellipticities of galaxies are more dominantly from the gravitational shear. Since the distortion was expected to vary significantly over the field, the image was first broken up into a 12×12 grid, with each mesh element of the grid being treated separately, then the deconvolution script was run. This was first attempted in the IRAF software environment, but while it successfully returned point spread function (PSF) images and some output files, attempts to produce deconvolved images failed. Unfortunately development and maintenance of the IRAF code was discontinued in 2013, with the last release reported to have many bugs, and the continued use of IRAF is discouraged by the community (IRAF Community, 2021). Another attempt was made with The Astropy Project within the Anaconda Python Distribution software environment. A deconvolution package that utilizes the Richardson-Lucy iterative deconvolution algorithm (Richardson, 1972; Lucy, 1974) was employed here, but while it also was able to successfully create a PSF and use it to deconvolve the image, the results were that it smoothed signal from dim galaxies into the background and caused brighter galaxies to look more like stars. Since the dimmest recognizable galaxies were the "target population" of this study, images produced by this algorithm where they had been effectively smoothed away were not useful for our purposes. A range of 1-50 iterations was tested, but it quickly became clear that increasing
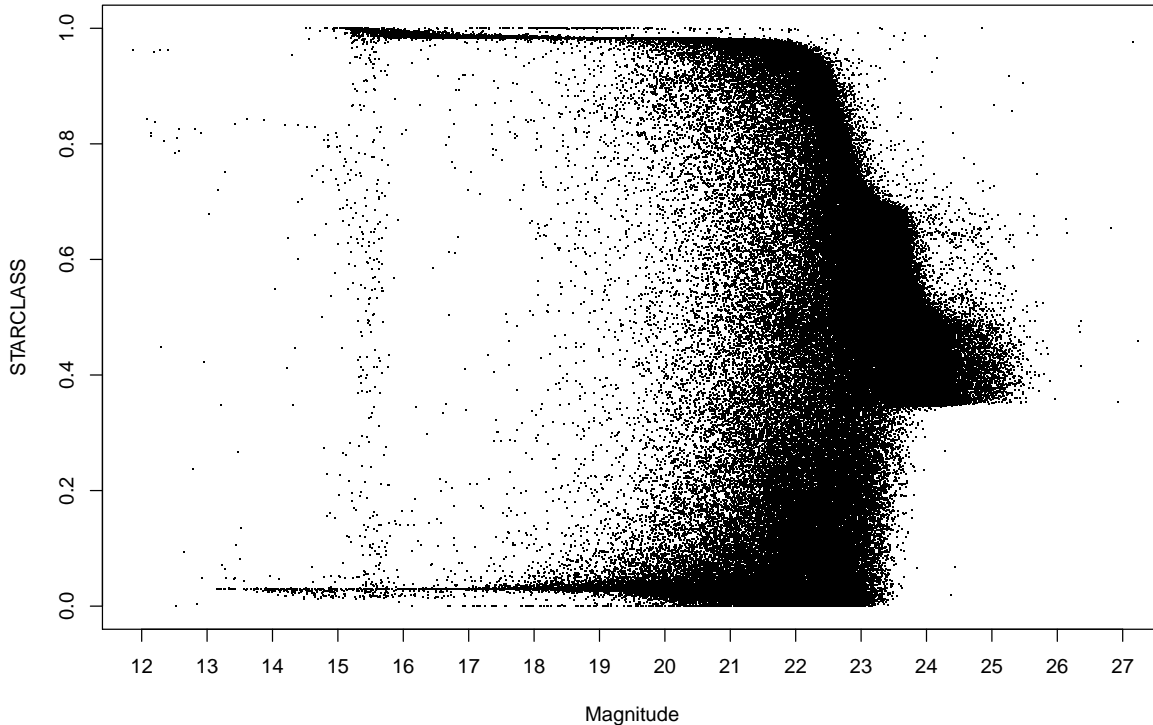
Figure 4.1: Star class as a function of magnitude for the Aquarius Supercluster.

the number of iterations returned worse results, and there was no number of iterations for which the result was an improvement over the raw image.

Since external software packages were not producing the desired deconvolution results, a simple mathematical devolution algorithm was coded instead to use the output catalog from Source Extractor to analyze the patterns of shapes and orientations of stars in the image and apply a mathematical correction to mitigate systematic elongation in any preferred direction. This was performed in R, a software environment for statistical computing.

4.3.1   Data Cuts

Upon examination of the $STAR\_CLASS$ value assigned to each object by SExtractor, it is clear that there is a limit to how faint an object can be before SExtractor

24
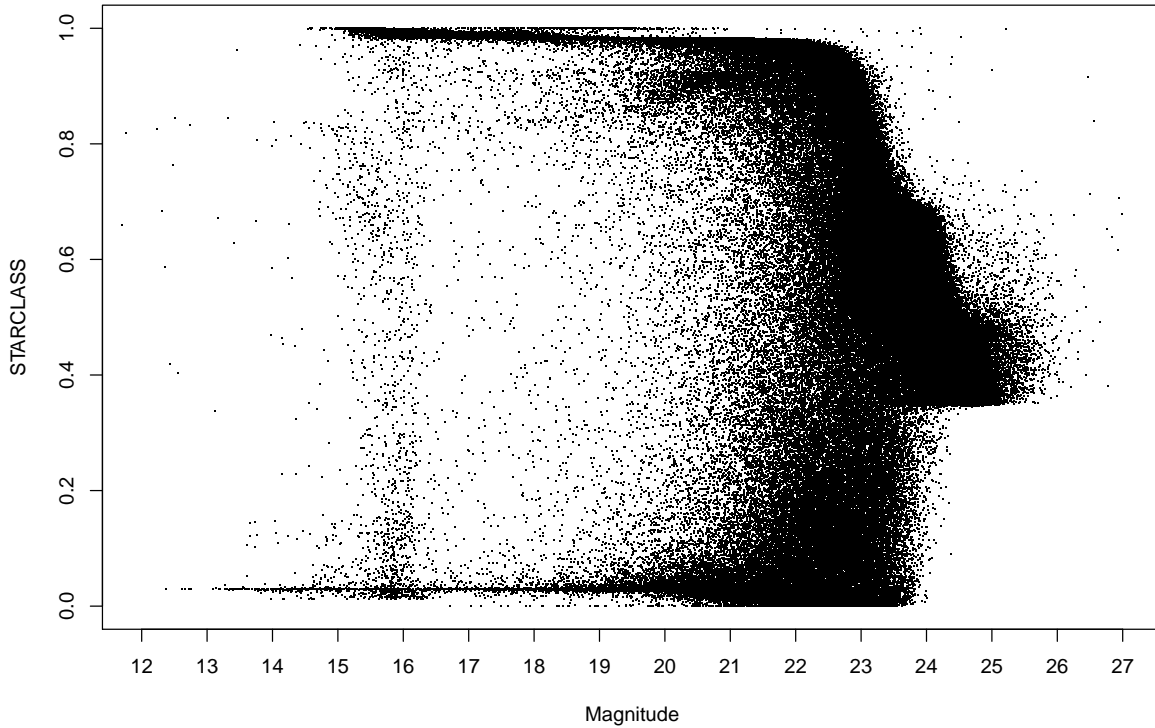
Figure 4.2: Star class as a function of magnitude for the Microscopium Supercluster.

becomes unable to classify it. At bright magnitudes, most objects are clearly classified as highly likely to be either a star or galaxy. However, as objects become fainter, it becomes more uncertain, until it finally starts giving all of the dimmest objects a mid-range value which indicates it cannot determine how to classify the object, as illustrated in Figures 4.1 and 4.2. This breakdown occurs between 23rd and 24th magnitude for each supercluster, thus there exists a built-in limit to the useable depth. There also exists an interesting band of objects between 15th and 16th magnitude that it appears Source Extractor had trouble classifying, but an inspection of these objects on the image did not reveal why. There was nothing obviously different about them to the naked eye, nor did there seem to be any pattern as to their position on the sky. Fortunately, this study is primarily interested in objects on the dim end of the spectrum, so objects brighter than 16th magnitude were not part of the sample used in the analysis.

Due to the dithering pattern of the observing program, the coverage and depth of the telescope image was uneven along the edges, which were therefore trimmed from the study region. The remaining area of the image was divided into meshes of variable size. The choice of mesh size is significant since splitting the image into smaller pieces increases the resolution of results, but decreases the number of objects within each mesh element, which potentially increases the potential amount of error in the results. Breaking the image into fewer pieces means there will be more objects within each piece, which should increase the accuracy of results, but decreases the resolution. A 12×12 mesh was decided upon as being an appropriate balance between accuracy and resolution, but 6×6 and 24×24 options were also encoded to test how the size of the mesh would affect the results. Finally, the empty corners (due to the shape of the DECam) were discarded, leaving the data broken into 96 pieces of the 12×12 grid, 24 pieces of the 6×6 grid, and 492 pieces of the 24×24 grid.

For each supercluster, a set of stars and galaxies was defined using data cuts based on $STAR\_CLASS$ and apparent magnitude. In order to determine what cutoff values gave the best results, each parameter was tested individually to see the effects different values, then the best value kept and the next parameter tested. Then the parameters were re-tested with the new values in an iterative process until the best scores were achieved. For more on this, see Appendix A: Effects of Data Cuts.

The stars were used to measure the amount of distortion of the point spread function for each block. To qualify as a star for this purpose, an object had to have been assigned a $STAR\_CLASS$ value of at least 0.80 by Source Extractor. The MSC is somewhat close to galactic plane of the Milky Way, and thus many stars are included in the field of view, and therefore a magnitude range of $16 < m < 19.5$ returns plenty of stars. The ASC is quite a bit farther from the galactic plane, and thus the field of view contains vastly fewer stars. Due to this, a wider range of $16 < m < 22$ is specified in order to include more stars. Since stars should be fairly round and distortion is expected to produce

only small effect on the shapes, stars with an ellipticity greater than 0.08 were discarded to avoid results being skewed by outliers.

Galaxies of interest were identified in a similar manner, based on $STAR\_CLASS$ and magnitude. Since the ASC region is a rather crowded field in terms of galaxies, aggressive cuts could be made while still keeping an adequate number of galaxies, and thus only objects with a magnitude of $21 < m < 23$ and an assigned $STAR\_CLASS$ value of 0.30 or lower were kept. The MSC field is much more sparsely populated, and thus more lenient cuts of $20 < m < 24$ and an assigned $STAR\_CLASS$ value of 0.50 or lower were used to identify galaxies there. With such lenient cuts, there is naturally the possibility of a small number of unwanted objects creeping into the sample, and there are likely biases present in some of the determinations made by Source Extractor of the characteristics of some objects due to noise rectification or model misspecification, but given the many thousands of objects in the sample, a small number of outliers should have negligible effects on the results. A study by Kling et al. suggests that maximizing the number of objects used for the analysis works best for weak lensing detection that is not influenced by systematic errors (Kling et al., 2005).

4.3.2 "Deconvolution" - Rice Technique

Having determined the inadequacy of standard methods of deconvolution for objects so close to the background noise level, a new method of deconvolution was designed. The stars in each mesh element are binned according to the orientation angle of their major axes in increments of 10 degrees, and two different methods of analysis are employed. In the first method, the number of stars in each orientation bin is counted. In the second method, the ellipticities of the objects in each orientation bin are summed. This procedure was then repeated separately for galaxies. Then the bin with the largest number of stars is identified, and if the number of stars in that bin is at least 2σ above the mean and the mesh element contains at least 10 stars, the deconvolution algorithm is triggered for that
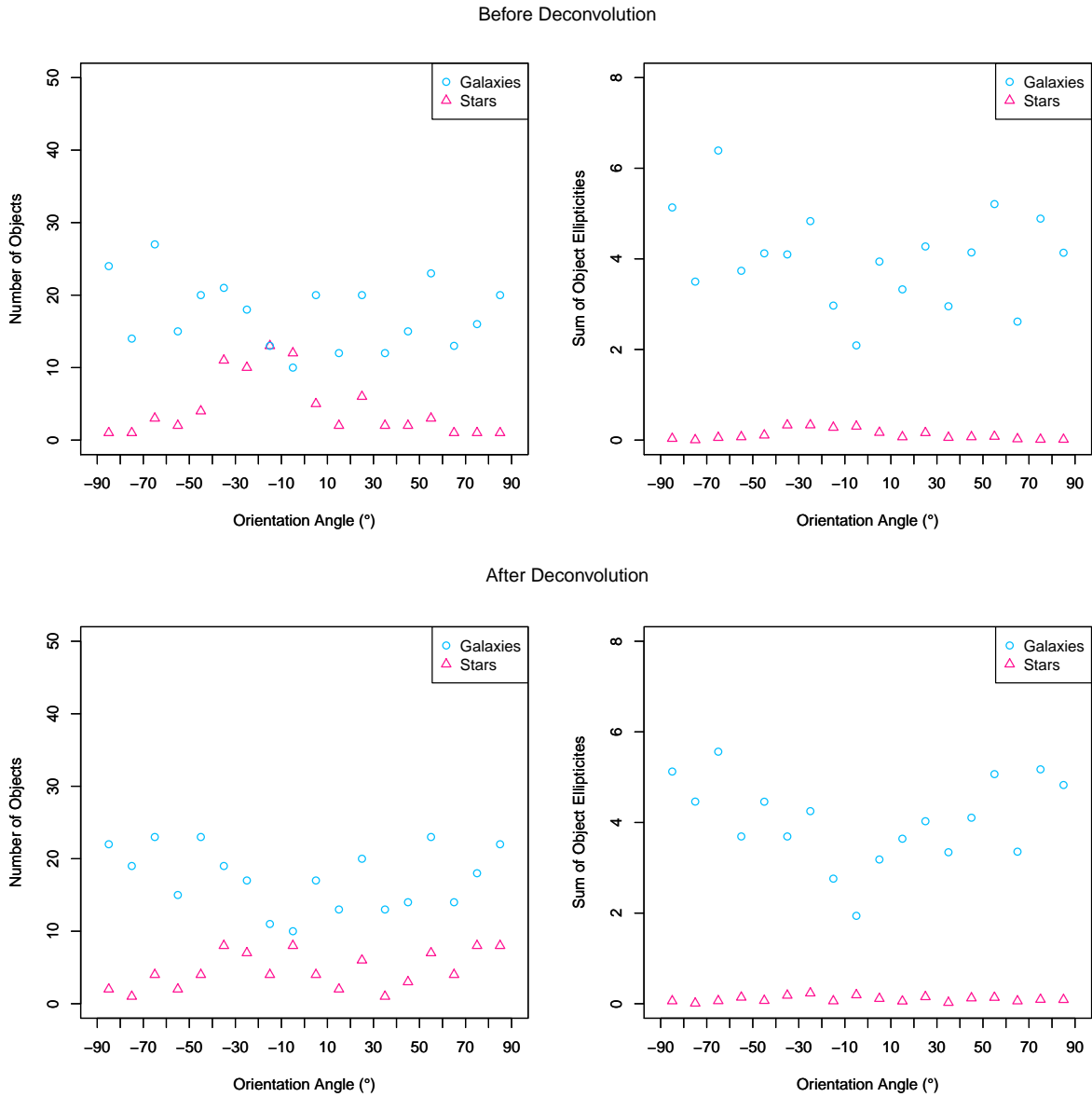
Figure 4.3: An example of the effect of deconvolution on the stars and galaxies in one mesh element. Objects are binned in increments of 10 degrees. The top-left graph shows the number of stars and galaxies per orientation bin before deconvolution; the bottom-left shows the same graph after deconvolution. The top-right graph shows the sum of the ellipticities of the stars and objects per orientation bin before deconvolution; the bottom-right shows the same graph after deconvolution.
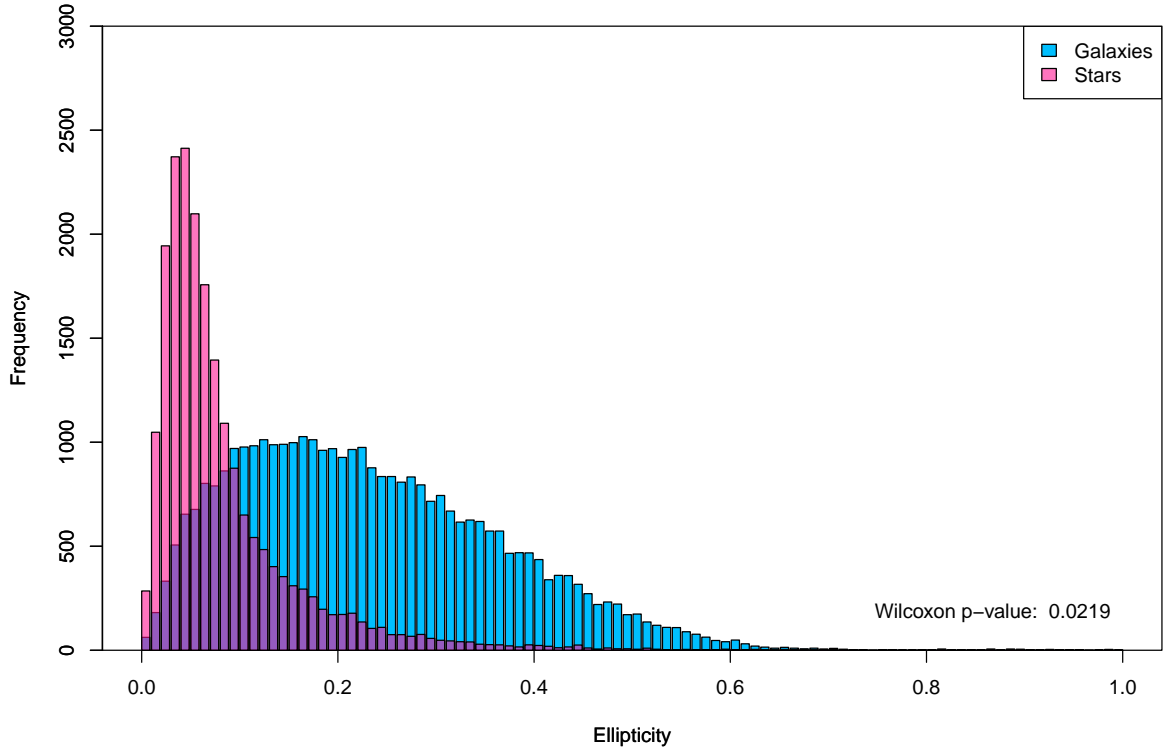
Figure 4.4: A comparison of the ellipticity distribution of stars and galaxies as identified in the image of the ASC region.

element. The deconvolution algorithm begins by looking through the bin with the most stars and its neighboring bin on either side, and finding the median orientation of the stars across these three bins, which is assumed to be the peak orientation. It then calculates the average ratio of minor to major axis for all stars with orientations within five degrees of the peak orientation in order to measure the amount of distortion in that preferred direction, and uses that information to re-calculate the major and minor axes, ellipticity, and orientation angle of every object in that mesh element according to the following equations, where A is the major axis, B is the minor axis, θ_p is the peak orientation, and θ_0 is the orientation angle of the object being deconvolved:

$$A = A_0 * (1 - (1 - \frac{B_0}{A_0})cos(|\theta_p - \theta_0|)) \tag{4.1}$$

29
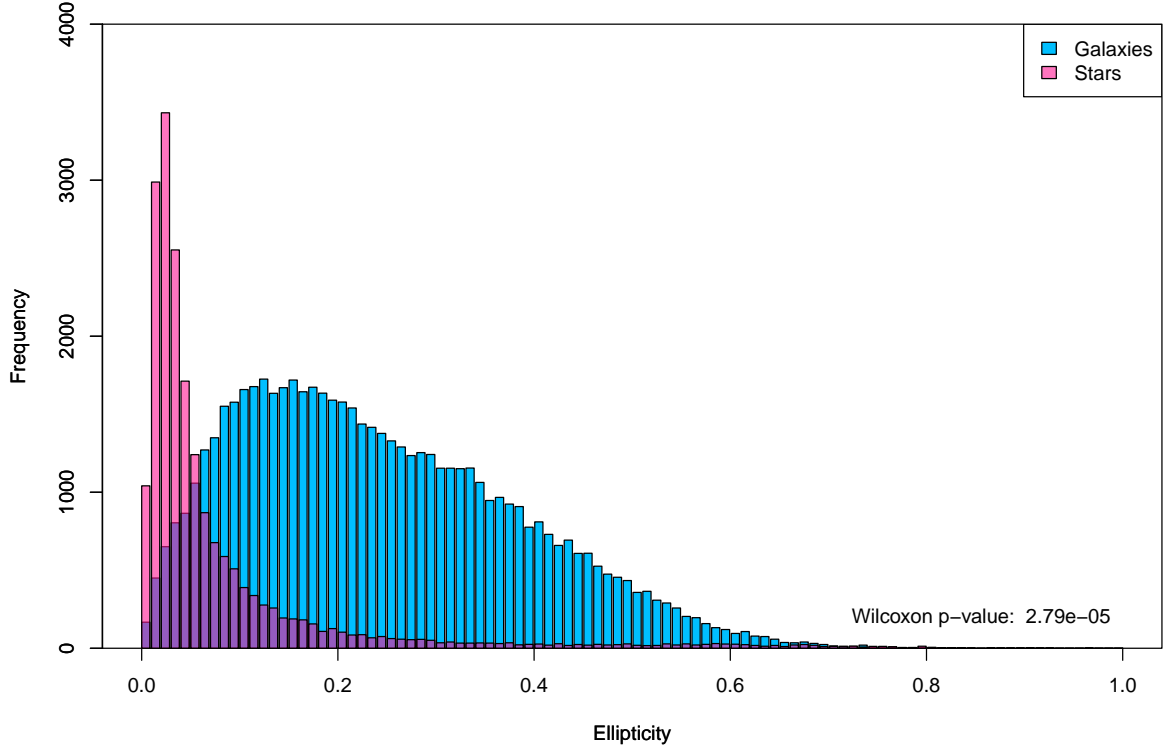
Figure 4.5: A comparison of the ellipticity distribution of stars and galaxies as identified in the image of the MSC region.

$$B = B_0 * (1 - (1 - \frac{B_0}{A_0})sin(|\theta_p - \theta_0|)) \tag{4.2}$$

$$\varepsilon = 1 - B/A \tag{4.3}$$

$$\theta = tan^{-1}(tan(\theta_0 - \theta_p) * \frac{A_0}{B_0}) + \theta_p \tag{4.4}$$

An example of the results of this process can be seen in Figure 4.3, and a brief inspection shows that while the deconvolution process changes the graph for stars quite a bit, the effect on the graph for galaxies is small. This is to be expected, since the ellipticities of the stars is much lower in general than the ellipticities of the vast majority of galaxies, as seen in Figures 4.4 and 4.5. Each of those figures is also fit with a Wilcoxon
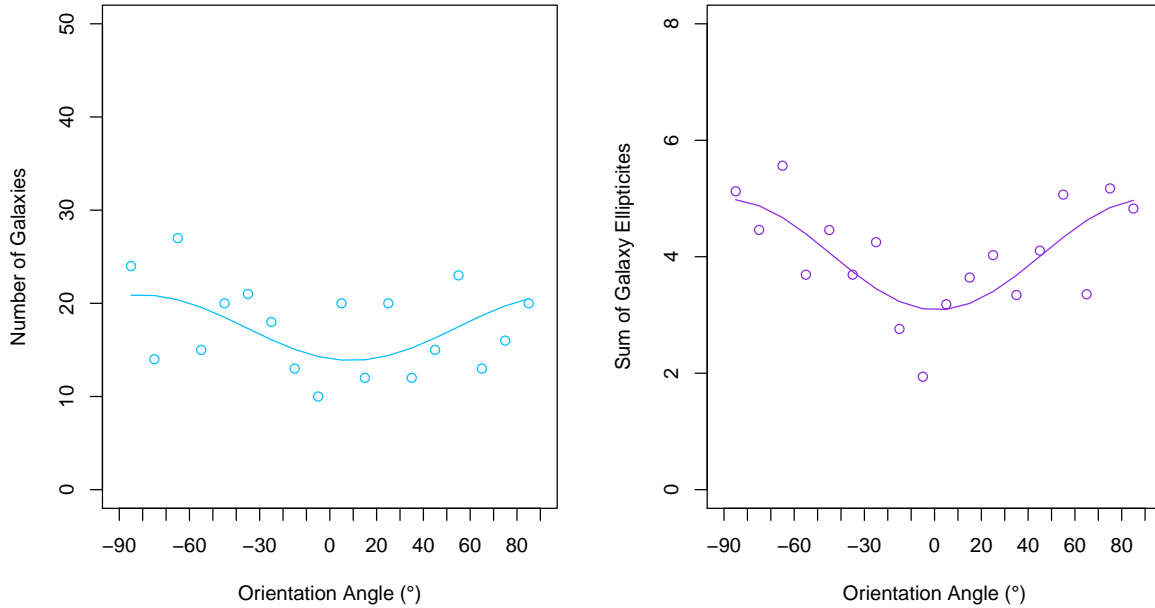
Figure 4.6: R fits a curve to the distribution of galaxy orientations to find the strength and direction of the shear. The fit on the left peaks at $-81°$ and has an amplitude of 3.5, while the graph on the right peaks at $-89°$ and has an amplitude of 0.95. An orientation angle of $0°$ indicates a horizontal shear in the image, whereas an orientation of $±90°$ corresponds to a shear in the vertical direction.

p-value, which compares two data samples (in this case, stars and galaxies) and estimates the likelihood of them being subsets of the same population (Wilcoxon, 1945). The low p-values returned here suggest that the data cuts based on the results from Source Extractor have done a reasonably good job separating galaxies from stars, though it is notably lower for the MSC than the ASC since the magnitude range used for stars and galaxies did not overlap as they did for the ASC.

4.4 Lensing Analysis

Once the deconvolution algorithm has finished running, the stars are re-binned according to the orientation angle of each object. As before, two different sets of bins are created, with one set containing the number of stars per orientation bin, and the other

containing the sum of the ellipticities of the stars in each bin. Galaxies are also re-binned separately once again. The R script then attempts to fit a cosine curve to each of the binned sets of galaxy data in order to gauge the direction and strength of the gravitational shear in that mesh element, as seen in Figure 4.6. This information is then turned into a vector map of the area, with the direction of the vectors showing the direction of galaxy elongation, and the size of the vectors representing the strength of the signal in that region. Such maps depicting the effects of deconvolution on the stars and galaxies in each region can seen in Figures 4.7, 4.8, 4.9, and 4.10.
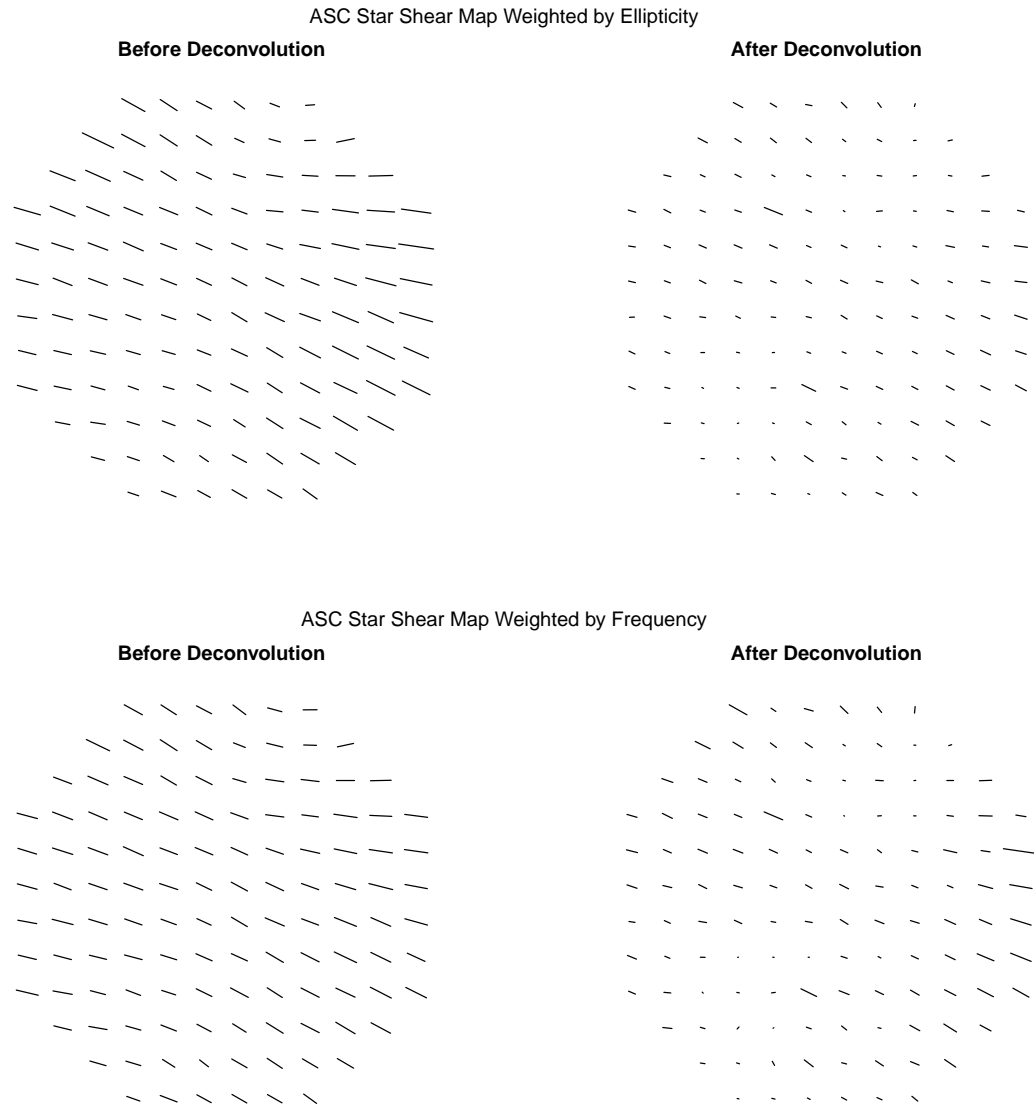
Figure 4.7: A comparison of the star shear maps in the ASC before and after deconvolution. The "before" and "after" version are to the same scale for each set. It is easily observed that the algorithm has reduced the measured shear in the majority of mesh elements.

ASC Galaxy Shear Map Weighted by Ellipticity

Before Deconvolution   **After Deconvolution**

ASC Galaxy Shear Map Weighted by Frequency

Before Deconvolution   **After Deconvolution**
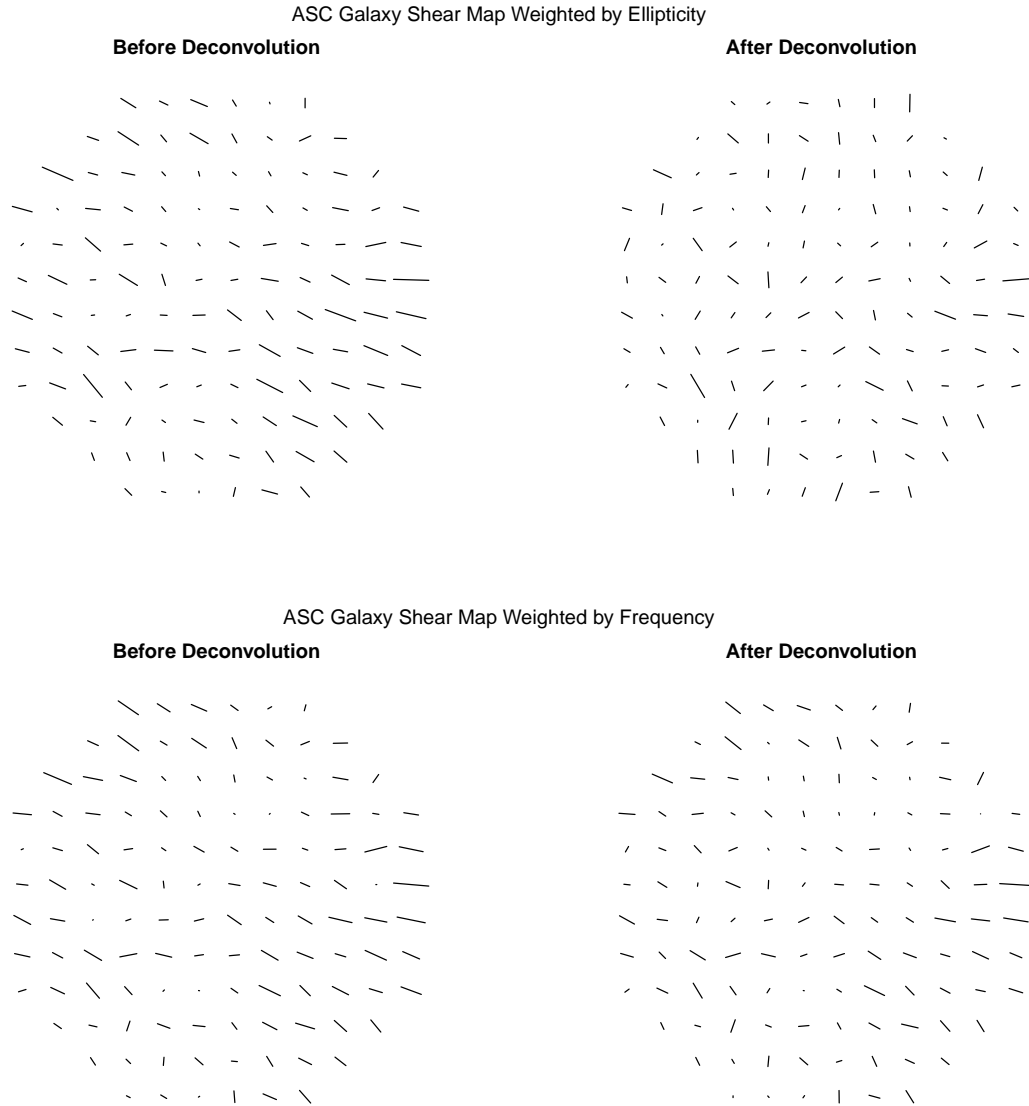
Figure 4.8: A comparison of the galaxy shear maps in the ASC before and after deconvolution. The "before" and "after" version are to the same scale for each set. Deconvolution is seen to have only minor effects on the galaxy shear.

MSC Star Shear Map Weighted by Ellipticity

Before Deconvolution   **After Deconvolution**

MSC Star Shear Map Weighted by Frequency

Before Deconvolution   **After Deconvolution**
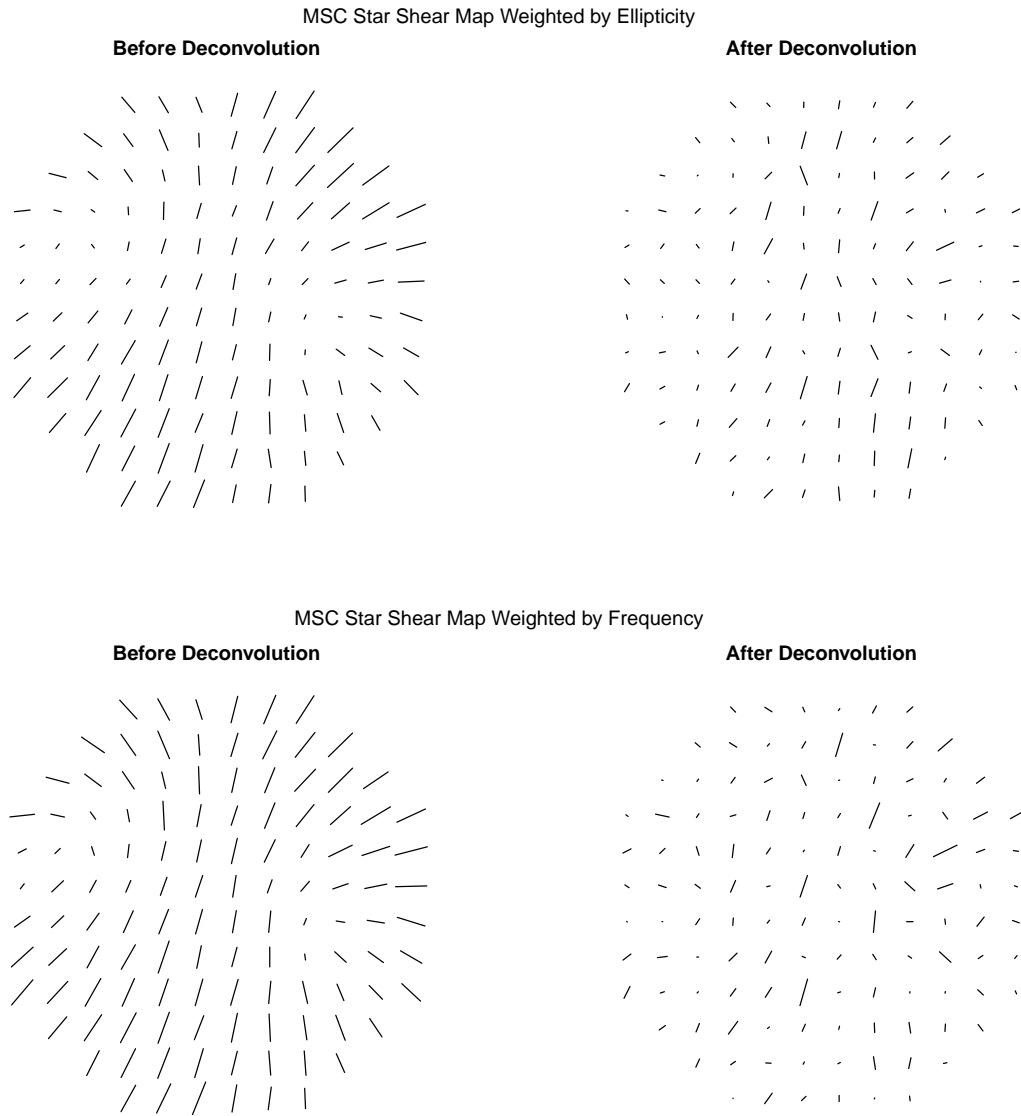
Figure 4.9: A comparison of the star shear maps in the MSC before and after deconvolution. The "before" and "after" version are to the same scale for each set. As was the case with the ASC, once again the algorithm has reduced the measured shear in the majority of mesh elements.

MSC Galaxy Shear Map Weighted by Ellipticity

Before Deconvolution   **After Deconvolution**

MSC Galaxy Shear Map Weighted by Frequency

Before Deconvolution   **After Deconvolution**
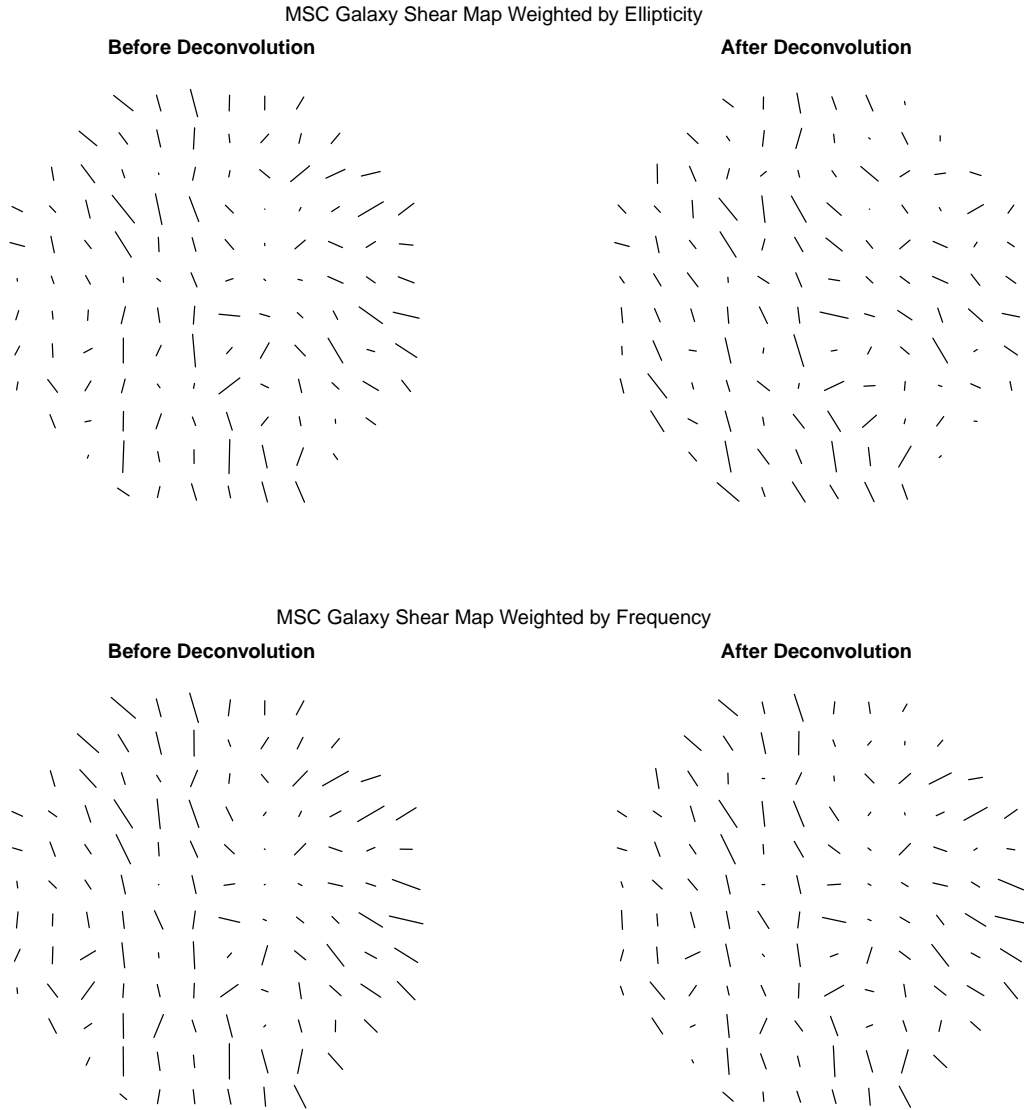
Figure 4.10: A comparison of the galaxy shear maps in the MSC before and after deconvolution. The "before" and "after" version are to the same scale for each set. As with the ASC, deconvolution is seen to have only minor effects on the galaxy shear.

STATISTICS AND RESULTS

In order to interpret the lensing maps, it is necessary to understand how the mass distribution is expected to lens the background galaxies. Therefore, the next step of the process was to create model maps of the expected gravitational shear from the cluster members of the superclusters, which we can then compare to our data maps.

5.1 Modeling the Superclusters

Table 5.1: Cluster positions and masses. RA and Dec are taken from the SIMBAD Astronomical Database (https://simbad.unistra.fr/simbad/), and masses are taken from the values published in Pearson & Batuski (2013).

Supercluster	Cluster	RA (J2000)	Dec (J2000)	Mass($10^{15}h^{-1}M_\odot$)
ASC	A2541	$23^h10^m04^s$	$-22°57'43"$	0.591
	A2546	$23^h10^m46^s$	$-22°39'42"$	0.422
	A2554	$23^h12^m20^s$	$-21°29'50"$	0.660
	A2555	$23^h12^m45^s$	$-22°12'40"$	0.043
MSC	A3693	$20^h34^m22^s$	$-34°29'40"$	0.871
	A3695	$20^h34^m48^s$	$-35°49'39"$	0.652
	A3696	$20^h35^m10^s$	$-34°54'36"$	0.023
	A3705	$20^h41^m42^s$	$-35°14'00"$	0.142

A concentration of matter will lens passing light from background sources such that they appear elongated in the direction tangential to a circle centered on the mass acting as the lens. A model of the expected lensing across each region was created for each supercluster region based on the cluster positions and masses. The cluster locations and approximate masses found by Pearson & Batuski (2013), who calculated virial masses from velocity dispersions of galaxies within the clusters according to methods of Carlberg et al. (1996), are given in Table 5.1. For each cluster, coordinates are first converted from right ascension and declination to the equivalent location on the grid, and the direction tangential to that spot was determined for each mesh element of the grid. For a cluster

that is modeled as an isothermal sphere, the distortion is proportional to r^{-1} (Miralda-Escudé, 1991), and therefore the strength the effect for each element was calculated as $\sim M/r$. Finally, the results from each of the four clusters in the region is combined to create an overall map of the expecting lensing due to the clusters alone. The clusters depicted outside the region of study in Figures 3.4 and 3.5 are not expected to contribute significantly to the lensing within the region of study due to the rapid falloff of signal strength with distance.

5.2   Comparing Data with Models

Three different methods are used to compare the supercluster model with the map generated from the data:

1. For each mesh element of the grid, the orientation of the vectors from the data and model are compared and assigned a score based on their relative alignments. The scale is created such that two vectors that align perfectly in the same direction are given a score of 1, vectors that are 45° apart are assigned a score of zero, and vectors that are 90° apart are assigned a score of -1. (This method was also employed in the selection of data cuts as described in Appendix A: Effects of Data Cuts.)

2. Each mesh element is scored in the same way as method one, but then the score is multiplied by the size of both the data and model vectors (where the scale is such that the largest vector has a value of 1) so that parts of the image with small actual or expected lensing are weighted less than sections with large actual and expected lensing.

3. The effect of method two is that the scores are hugely dominated by the few vectors closest to the most massive clusters. Therefore for method three, each mesh element is scored in the same way as method two, but the areas containing the strongest lensing effect in the model maps are set to zero, and the rest of the vectors are
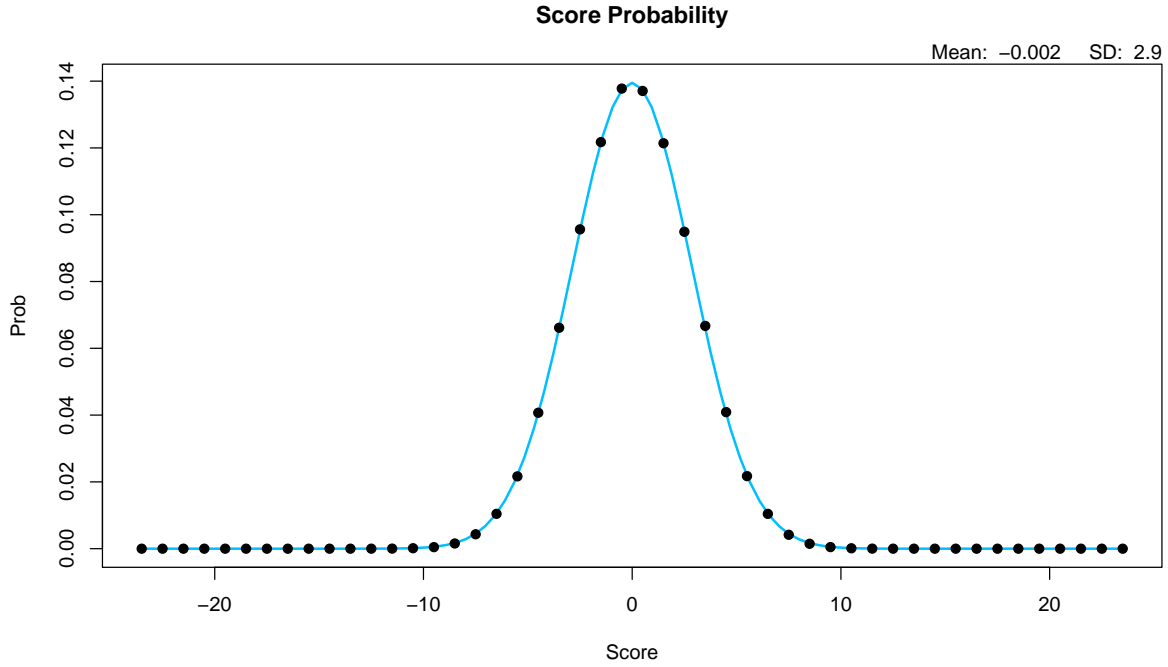
Figure 5.1: A Gaussian distribution curve fitted to scores from randomly generated data.

re-scaled so that the largest again has a value of 1. This allows the score to reflect how well the vectors further from the clusters align with the model, to allow sensitivity to more diffuse dark matter. The limit at which any stronger vectors are set to zero is chosen to maximize the score of each graph.

Diagrams for all three scoring methods for each grid size can be found in Appendix B.

5.3 Statistical Significance

Once the scoring was completed, a method of interpreting the score was needed. To this end, a program was designed to generate one million cases of random vector data for each of the three different grid sizes and score each of them against the model data for the each supercluster region. A Gaussian distribution curve was then fit to the resulting spread of scores (as seen in Figure 5.1) and the standard deviation returned, which was then used to calculate the confidence levels in Tables 5.2 and 5.3.

39

Table 5.2: Scores and statistical significance levels for ASC maps.

Grid	Scoring Method	Std Dev	Ellipticity Map Score	Frequency Map Score	Ellipticity Confidence Level	Frequency Confidence Level
$6x6$	Orientation Only	2.9	5.7	6.1	2.0σ	2.1σ
	Weighted by Vector Size	0.58	0.57	0.71	1.0σ	1.2σ
	Largest Vectors Cut	0.71	1.4	1.6	2.0σ	2.3σ
$12x12$	Orientation Only	6.3	18.5	16.3	2.9σ	2.6σ
	Weighted by Vector Size	0.70	1.5	1.1	2.1σ	1.6σ
	Largest Vectors Cut	1.7	3.5	2.8	2.1σ	1.6σ
$24x24$	Orientation Only	12.8	23.2	14.8	1.8σ	1.2σ
	Weighted by Vector Size	1.2	2.0	1.2	1.7σ	1.0σ
	Largest Vectors Cut	2.3	6.4	4.6	2.8σ	2.0σ

5.4 Discussion of Results

It is immediately clear upon inspection of results summarized in Tables 5.2 and 5.3 that the data and model agree much more strongly for the MSC than the ASC. With a confidence level of 1-3σ for the majority of maps, it seems likely that we are detecting at least some weak gravitational lensing for the ASC, although not at a significant level. The much higher levels of 1-8σ for most of the maps of the MSC region are strong evidence of gravitational lensing in this field. There are a number of possible reasons for the discrepancy in results between the two regions, including possible effects of the inter-cluster matter that was the target of this study. However, it seems much more likely a result of the effects of other foreground and background clusters in the ASC field of view. A catalog of

Table 5.3: Scores and statistical significance levels for MSC maps.

Grid	Scoring Method	Std Dev	Ellipticity Map Score	Frequency Map Score	Ellipticity Confidence Level	Frequency Confidence Level
6x6	Orientation Only	2.9	7.0	11.5	2.4σ	4.0σ
	Weighted by Vector Size	0.39	1.0	1.7	2.6σ	4.4σ
	Largest Vectors Cut	0.81	2.2	2.3	2.7σ	2.8σ
12x12	Orientation Only	6.3	36.8	41.2	5.8σ	6.5σ
	Weighted by Vector Size	0.83	1.3	1.4	1.6σ	1.7σ
	Largest Vectors Cut	1.8	7.4	10.6	4.1σ	5.9σ
24x24	Orientation Only	12.8	88.4	107.9	6.9σ	8.4σ
	Weighted by Vector Size	0.49	0.69	0.58	1.4σ	1.2σ
	Largest Vectors Cut	3.4	19.6	22.3	5.8σ	6.6σ

all identified clusters in both regions was compiled from the SIMBAD Astronomical Database and NASA/IPAC Extragalactic Database (and any listings that seemed likely to be the same object were condensed to a single entry). Objects lying just outside the analysis region were included for completeness. The resulting cluster maps can be seen in Figure 5.2. While the sky offers a fairly clean view of the MSC with only a single identified background cluster (in projection with another cluster member of the MSC), the ASC region is cluttered with various other clusters. It was noted in a couple of previous studies of the region that a second foreground supercluster overlapped on the sky with the ASC (Caretta et al., 2002; Smith et al., 2004), and it has been postulated that the background clusters might be part of extended structure with the ASC, connected by a filament

All Clusters in the Field of the ASC   **All Clusters in the Field of the MSC**
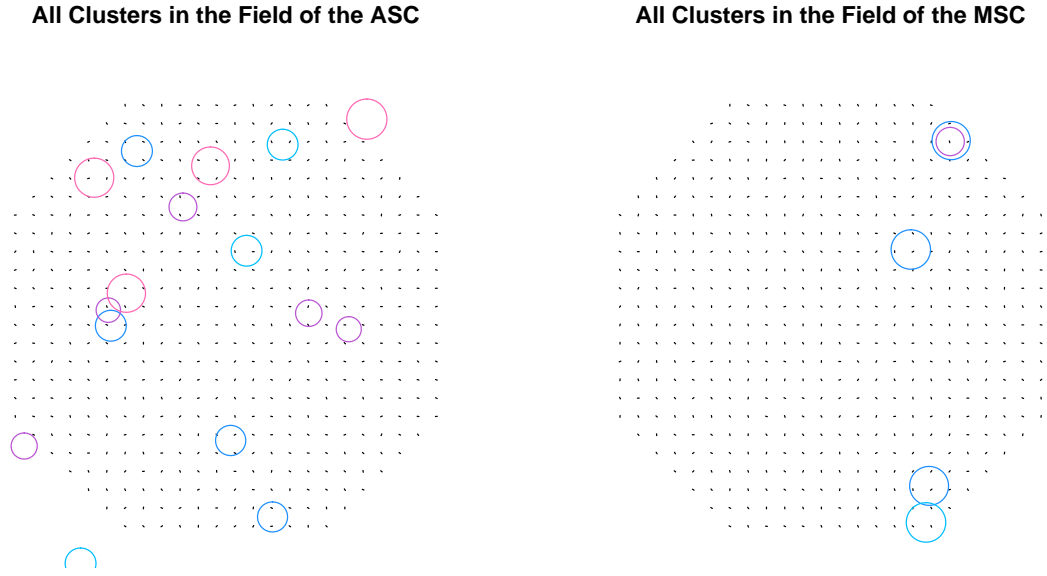
Figure 5.2: A map of all clusters in each of the two supercluster regions. The darker blue circles are the Abell clusters that are formally recognized as part of the supercluster, while the lighter blue circles are lesser clusters at approximately the same z value. The smaller purple circles indicate background clusters in the range of $z \sim 0.12 - 0.14$, while the larger pink circles denote foreground clusters.

(Batuski et al., 1999; Caretta et al., 2002). These additional clusters likely contribute some lensing effect of their own, and especially in the case of the foreground structure, add an additional level of contamination to the sample of dim galaxies. Unfortunately, color information or spectroscopic data would be required to determine the redshift of each galaxy so as to sort distant background sources from dim foreground ones. In addition, little to no information on the masses was available for these extra clusters, thus limiting the ability to include them in the model data to see how they would affect the lensing map.

The difference in the level of agreement between the weighted vector maps and the maps with the largest vectors cut should be considered cautiously. The size limits at which the cuts were made were chosen to maximize the raw map scores, which occurred when not just the clusters themselves were excluded but also much of the areas connecting them.

MSC Shear Map – Weighted by Ellipticity　　　　**MSC Shear Map – Weighted by Frequency**

MSC Shear Map – Weighted by Ellipticity　　　　**MSC Shear Map – Weighted by Frequency**
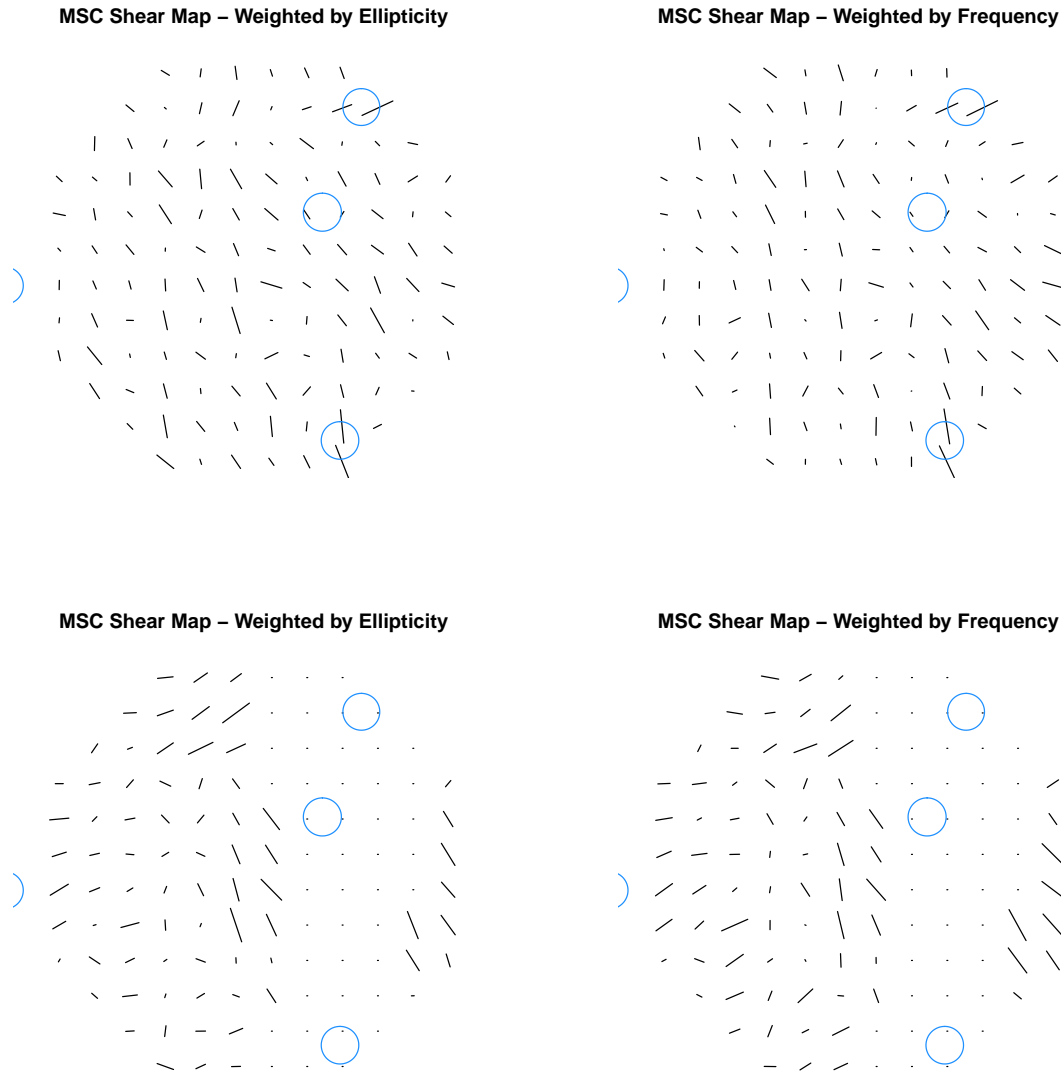
Figure 5.3: Top: The MSC data map with the model map subtracted. Bottom: The core region removed and the remaining map areas re-scaled, then subtracted.

This could suggest that there may be some inter-cluster matter connecting the clusters distributed in the cut regions, creating a local disagreement in those areas between the data and model vectors, but it is more likely that the rescaling of the remaining vectors simply created more large vectors for a higher score. In addition, since the largest vectors dominate the scoring mechanism and there are fewer vectors of this size on the weighted maps with no vector cuts, they become very susceptible to large scoring impacts from a few

erratic vectors, which could be due to errors or biases in the Source Extractor's determined parameters. The areas farther from the clusters generally exhibit a fair level of agreement with the model data, so it seems that lensing from the clusters dominate at large distances.

In an attempt to tease out any other lensing effects not caused by the individual clusters, another algorithm was designed to subtract the model maps from the data map to see if the result would show any remaining systematic patterns. This was performed in two ways. First, the whole model map was subtracted from the data map. However, since the model vectors far from the clusters are quite small, this method of subtraction mainly affected the region closest to the clusters, with little effect on the area further away. Therefore, a second subtraction map was created where the area closest the clusters was cut out and the remaining parts of the maps were rescaled, then subtracted, to see if any large-scale lensing patterns might be revealed in these regions. Due to the cluttered field and the lack information needed to accurately model the other clusters in the area, this exercise yielded little of value in the ASC region. The results of this process for the MSC can be seen in Figure 5.3. A cursory inspection here does reveal what appear to be systematic alignments of vectors in some areas, which hints at a possible larger-scale lensing effect across the region, but a wider field of view would likely be required to see the full scope of such broad patterns.

In summary, the high confidence levels reflected in Table 5.3 is the result of the lensing vectors from the data lining up well with the modeled cluster effects only, with no filamentary structure included. Given this high level of agreement, it is unlikely that any possible inter-cluster filamentary structures in the MSC would be particularly massive compared to the clusters themselves. Unfortunately, the ASC region is too cluttered with foreground and background clusters to give any significant results. We are left with no clear evidence of massive dark matter filaments in either of the two supercluster regions.

CHAPTER 6

CONCLUSIONS

This work constitutes the first analysis of weak gravitational lensing that has been performed for the Aquarius and Microscopium supercluster regions. The data from the ASC and MSC both show evidence of lensing, with the ASC results showing supercluster member domination at the 1-3σ level and the MSC results being in the 2-8σ range.

It is interesting to note that although two different methods of analyzing galaxy shear and three different grid sizes were explored, there was no obvious single best outcome. Measuring the strength of the gravitational shearing signal by fitting a graph of the number of galaxies versus their orientations provided the higher confidence levels for the MSC where there is little other structure (and thus little contamination) in the region, whereas results in the ASC were mixed, with higher confidence levels coming from using the maps created from fitting galaxy ellipticities vs. orientation in many cases. Splitting the regions into differently-sized grids also revealed no clear best choice, as different choices of grid size yielded varying confidence levels with no obvious pattern. They are each of value, however, as the 24×24 grid offers the best resolution at the expense of fewer objects per bin and thus less confidence in the accuracy of each individual resulting vector, while the 6×6 grid offers more certainty about the accuracy of the strength and direction of each individual vector from the larger number of objects per mesh element, but sacrifices resolution and thus sacrifices the ability to detect small-scale fluctuations, and the 12×12 offers a look in-between those two extremes.

The results neither confirm nor preclude the existence of a filamentary structure of inter-cluster matter, but at least in the case of the MSC, they do suggest that any such filaments would likely be significantly less massive than the clusters themselves, which appear to dominate each region. Further study of these regions may be beneficial for characterizing more clearly the distribution of matter in these regions.

6.1 Further Research

As mentioned in Chapter 4, the results of this analysis are largely dependent on the output of Source Extractor, which assesses the shape and orientation of each object, as well as the object's likelihood to be a star or galaxy, and that SExtractor has more difficulty accurately classifying objects on the dim end. A deeper view would therefore be beneficial both in order to increase the number of usable background galaxies and to make it easier for SExtractor to more accurately characterize the objects in the 23-24 magnitude range. It may also be of interest to obtain data for a wider view of each supercluster to look for any possible larger-scale effects of the mass distribution contained within. In addition, color information obtained via observations through different color filters might be useful for identifying and removing foreground galaxies from the galaxy sample, thus lessening contamination of the lensing signal.

The results for the ASC in particular warrant further study of the foreground supercluster structure in this region. Mass information for these clusters from spectroscopic observations would make it possible to include the anticipated lensing effects of those clusters on the model map, or to create a method of subtracting these effects from the data map to see if the result of doing so would agree more strongly with the model map created from just the ASC.

The modeling comparison algorithm could also be further developed, perhaps with Monte Carlo guesses at likely filament locations spanning between clusters and possible mass distributions among them to see if this would result in an increased or decreased agreement with the model maps. Doing so may reveal more insights for the inter-cluster matter structure of both the ASC and MSC.

REFERENCES

Abell, G. O. (1958). The distribution of rich clusters of galaxies. *ApJS*, 3:211.

Abell, G. O. (1961). Evidence regarding second-order clustering of galaxies and interactions between clusters of galaxies. *Astronomical Journal*, 66:607.

Angulo, R. E., Springel, V., White, S. D. M., Jenkins, A., Baugh, C. M., and Frenk, C. S. (2012). Scaling relations for galaxy clusters in the Millennium-XXL simulation. *Monthly Notices of the Royal Astronomical Society*, 426:2046.

Bahcall, N. A. and Soneira, R. M. (1982). Large-scale superclusters surrounding the giant galaxy void in Bootes? *The Astrophysical Journal*, 258:L17.

Bardelli, S., Scaramella, R., Vettolani, G., Zamorani, G., Zucca, E., Collins, C. A., and MacGillivray, H. T. (1993). Study of the Shapley superclusters. *The Messenger*, 71:34.

Bartelmann, M. and Schneider, P. (2001). Weak lensing. *Physics Reports*, 340:291.

Batiste, M. G. (2014). *Dynamical Analyses of Three Candidate Bound Superclusters of Galaxies*. Doctoral dissertation, University of Maine.

Batiste, M. G. and Batuski, D. J. (2013). A dynamical analysis of the Corona Borealis supercluster. *Monthly Notices of the Royal Astronomical Society*, 436:3331.

Batuski, D. J. and Burns, J. O. (1985). A possible 300 megaparsec filament of clusters of galaxies in Perseus-Pegasus. *The Astrophysical Journal*, 299:5.

Batuski, D. J., Maurogordato, S., Balkowski, C., and Olowin, R. P. (1995). Redshift observations of Abell/ACO galaxy clusters in two candidate superclusters. *Astronomy and Astrophysics*, 294:677.

Batuski, D. J., Miller, C. J., Slinglend, K. A., Balkowski, C., Maurigordato, S., Cayatte, V., Felenbok, P., and Olowin, R. (1999). Discovery of extreme examples of superclustering in Aquarius. *The Astrophysical Journal*, 520:491.

Bertin, E. (2006). Sextractor v2.5 user's manual. http://astroa.physics.metu.edu.tr/MANUALS/sextractor/sextractor.pdf.

Boylan-Kolchin, M., Springel, V., White, S. D. M., Jenkins, A., and Lemson, G. (2009). Resolving cosmic structure formation with the Millennium-II simulation. *Monthly Notices of the Royal Astronomical Society*, 398:1150.

Caretta, C. A., Maia, M. A. G., Kawasaki, W., and Willmer, C. N. A. (2002). The Aquarius supercluster - I. Identification of clusters and superclusters. *The Astronomical Journal*, 123:1200.

Carlberg, R. G., Yee, H. K. C., Ellingson, E., Abraham, R., Gravel, P., Morris, S., and Pritchet, C. J. (1996). Galaxy cluster virial masses and omega. *The Astrophysical Journal*, 462:32–49.

Carroll, B. W. and Ostlie, D. A. (2007). *An Introduction to Modern Astrophysics (Second Edition)*. Addison-Wesley, San Franscisco, California.

Casey, C. (2006). Optimizing sextractor parameters for Subaru MACS fields. https://www.ifa.hawaii.edu/reu/reu2006/casey.pdf.

Ciardullo, R., Ford, H., and Harms, R. (1985). Cluster redshifts in five suspected superclusters. *The Astrophysical Journal*, 293:69.

Colless, M., Dalton, G., Maddox, S., Sutherland, W., Norberg, P., Cole, S., Bland-Hawthorn, J., Bridges, T., Cannon, R., Collins, C., Couch, W., Cross, N., Deeley, K., de Propris, R., Driver, S. P., nd Richard S. Ellis, G. E., Frenk, C. S., Glazebrook, K., Jackson, C., Lahav, O., Lewis, I., Lumsden, S., Madgwick, D., Peacock, J. A., Peterson, B. A., Price, I., Seaborn, M., and Taylor, K. (2001). The 2dF galaxy redshift survey: spectra and redshifts. *Monthly Notices of the Royal Astronomical Society*, 328:1039.

de Vaucouleurs, G. (1953). Evidence for a local supergalaxy. *Astronomical Journal*, 58:30.

DES (2021). The Dark Energy Survey. https://www.darkenergysurvey.org/the-des-project/instrument/.

Dietrich, J. P., Schneider, P., Clowe, D., Romano-Diaz, E., and Kerp, J. (2005). Weak lensing study of dark matter filaments and application to the binary cluster A222 and A223. *Astronomy and Astrophysics*, 440(2):453.

Einasto, J., Jôeveer, M., and Saar, E. (1980). Structure of superclusters and supercluster formation. *Monthly Notices of the Royal Astronomical Society*, 193:353.

Favia, A., Batuski, D., and Howell, P. (2014). Mapping dark matter through weak lensing in the extremely overdense Aquarius and Microscopium supercluster cores. NOAO Proposal.

Gatti, M., Sheldon, E., Amon, A., Becker, M., Troxel, M., Choi, A., Doux, C., MacCrann, N., Navarro-Alsina, A., Harrison, I., Gruen, D., Bernstein, G., Jarvis, M., Secco, L. F., Ferté, A., Shin, T., McCullough, J., Rollins, R. P., Chen, R., Chang, C., Pandey, S., Tutusaus, L., Prat, J., Elvin-Poole, J., Sanchez, C., Plazas, A. A., Bacon, D., Bertin, E., Bjargava, S., Brooks, D., Burke, D. L., Rosell, A. C., Kind, M. C., Carretero, J., Castander, F. J., Conselice, C., Costanzi, M., Crocce, M., de Costa, L. N., Davis, T. M., Vicente, J. D., Desai, S., Diehl, H. T., Dietrich, J. P., Doel, P., Drlica-Wagner, A., Eckert, K., Everett, S., Ferrero, I., Frieman, J., García-Bellido, J., Gerdes, D. W., Giannantonio, T., Gruendl, R. A., Gschwend, J., Gutierrez, G., Hartley, W. G., Hinton, S. R., Hollowood, D. L., Honscheid, K., Hoyle, B., Huff, E. M., Huterer, D., Jain, B., James, D. J., Jeltema, T., Krause, E., Kron, R., Kuropatkin, N., Lahav, O., Lima, M., Maia, M. A. G., Marshall, J. L., Miquel, R., Morgan, R., Myles, J., Palmese, A., Paz-Chinchón, F., Rykoff, E. S., Samuroff, S., Sanchez, E., Scarpine, V., Schubnell, M., Serrano, S., Sevilla-Noarbe, I., Smith, M., Soares-Santos, M., Suchyta, E., Swanson, M. E. C., Tarle, G., Thomas, D., To, C., Tucker, D. L., Varga, T. N., Wechsler, R. H., Weller, J., Wester, W., and Wilkinson, R. D. (2021). Dark Energy Survey year 3 results:

Weak lensing shape catalogue. *Monthly Notices of the Royal Astronomical Society*, 504(3):4312.

Geller, M. J. and Huchra, J. P. (1989). Mapping the Universe. *Science*, 246:897–903.

Genel, S., Vogelsberger, M., Springel, V., Sijacki, D., Nelson, D., Snyder, G., Rodriguez-Gomez, V., Torrey, P., and Hernquist, L. (2014). Introducing the Illustris Project: the evolution of galaxy populations across cosmic time. *Monthly Notices of the Royal Astronomical Society*, 445(1):175.

Gray, M. E., Taylor, A. N., Meisenheimer, K., Dye, S., Wolf, C., and Thommes, E. (2002). Probing the distribution of dark matter in the A901/A902 supercluster with weak lensing. *The Astrophysical Journal*, 568:141.

Gregory, S. A. and Thompson, L. A. (1978). The Coma/A1367 supercluster and its environs. *The Astrophysical Journal*, 222:784.

Herschel, W. (1786). Catalogue of one thousand new nebulae and clusters of stars. *Philosophical Transactions of the Royal Society of London*, 76:457.

Heymans, C., Gray, M. E., Peng, C. Y., Waerbeke, L. V., Bell, E. F., Wolf, C., Bacon, D., Balogh, M., Barazza, F. D., Barden, M., Böhm, A., Caldwell, J. A. R., HäuBler, B., Jahnke, K., Jogee, S., van Kampen, E., Lane, K., McIntosh, D. H., Meisenheimer, K., Mellier, Y., Sánchez, S. F., Taylor, A. N., Wisotzki, L., and Zheng, X. (2008). The dark matter environment of the Abell 901/902 supercluster: A weak lensing analysis of the HST STAGES survey. *Monthly Notices of the Royal Astronomical Society*, 385:1431.

Holwerda, B. (2005). Source extractor for dummies. http://star-www.dur.ac.uk/ pdraper/extractor/Guide2source_extractor.pdf.

Horváth, I., Hakkila, J., and Bagoly, Z. (2014). Possible structure in the GRB sky distribution at redshift two. *Astronomy & Astrophysics*, 561:L12.

Horvath, I., Szécsi, D., Hakkila, J., Szabó, A., Racz, I. I., Tóth, L. V., Pinter, S., and Bagoly, Z. (2020). The clustering of gamma-ray bursts in the Hercules–Corona Borealis Great Wall: the largest structure in the Universe? *Monthly Notices of the Royal Astronomical Society*, 498(2):2544.

Hubble, E. (1929a). A relation between distance and radial velocity among extra-galactic nebulae. *Proceedings of the National Academy of Sciences of the United States of America*, 15:168.

Hubble, E. (1929b). A spiral nebula as a stellar system, Messier 31. *The Astrophysical Journal*, 69:103.

Institut d'Astrophysique de Paris (2017). Source extractor user manual. https://sextractor.readthedocs.io/en/latest/.

IRAF Community (2021). IRAF community distribution. https://iraf-community.github.io/.

Jeffrey, N., Gatti, M., Chang, C., Whiteway, L., Demirbozan, U., Kovacs, A., Pollina, G., Bacon, D., Hamaus, N., Kacprzak, T., Lahav, O., Lanusse, F., Mawdsley, B., Nadathur, S., Starck, J. L., Vielzeuf, P., Zeurcher, D., Alarcon, A., Amon, A., Bechtol, K., Bernstein, G. M., Campos, A., Rosell, A. C., Kind, M. C., Cawthon, R., Chen, R., Choi, A., Cordero, J., Davis, C., DeRose, J., Doux, C., Drlica-Wagner, A., Eckert, K., Elsner, F., Elvin-Poole, J., Everett, S., Ferté, A., Giannini, G., Gruen, D., Gruendl, R. A., Harrison, I., Hartley, W. G., Herner, K., Huff, E. M., Huterer, D., Kuropatkin, N., Jarvis, M., Leget, P. F., MacCrann, N., McCullough, J., Muir, J., Myles, J., Navarro-Alsina, A., Pandey, S., Prat, J., Raveri, M., Rollins, R. P., Ross, A. J., Rykoff, E. S., Sánchez, C., Secco, L. F., Sevilla-Noarbe, L., Sheldon, E., Shin, T., Torxel, M. A., Tutusaus, I., Varga, T. N., Yanny, B., Yin, B., Zhang, Y., Zuntz, J., Abbott, T. M. C., Aguena, M., Allam, S., Andrade-Oliveira, F., Becker, M. R., Bertin, E., Bhargava, S., Brooks, D., Burke, D. L., Carretero, J., Castander, F. J., Conselice, C., Costanzi, M., Crocce, M., da Costa, L. N., Pereira, M. E. S., Vicente, J. D., Desai, S., Diehl, H. T., Dietrich, J. P., Doel, P., Ferrero, I., Flaugher, B., Fosalba, P., García-Bellido, J., Gaztanaga, E., Gerdes, D. W., Giannantonio, T., Gschwend, J., Gutierrez, G., Hinton, S. R., Hollowood, D. L., Hoyle, B., Jain, B., James, D. J., Lima, M., Maia, M. A. G., , March, M., Marshall, J. L., Melchior, P., Menanteau, F., Miquel, R., Mohr, J. J., Morgan, R., Ogando, R. L. C., Palmese, A., Paz-Chinchón, F., Plazas, A. A., Rodriguez-Monroy, M., Roodman, A., Sanchez, E., Scarpine, V., Serrano, S., Smith, M., Soares-Santos, M., Suchyta, E., Tarle, G., Thomas, D., To, C., and Weller, J. (2021). Dark Energy Survey year 3 results: curved-sky weak lensing mass map reconstruction. *Monthly Notices of the Royal Astronomical Society*, 505(3):4626.

Katgert, P., Mazure, A., Perea, J., den Hartog, R., Moles, M., Fèvre, O. L., Dubath, P., Focardi, P., Rhee, G., Jones, B., Escalera, E., Biviano, A., Gerbal, D., and Giuricin, G. (1996). The ESO nearby Abell cluster survey I. *Astronomy and Astrophysics*, 310:8.

Kirshner, R. P., Oemler, A., Schechter, P. L., and Shectman, S. A. (1981). A million cubic megaparsec void in Boötes? *The Astrophysical Journal*, 248:57.

Kling, T. P., Antonio, I. D., Wittman, D., and Tyson, J. A. (2005). Wide-field weak lensing by RX J1347-1145. *The Astrophysical Journal*, 625:643.

Kopylova, F. G. and Kopylov, A. I. (1998). Structure and dynamic state of the Corona Borealis supercluster. *Astronomy Letters*, 24:491.

Kron, R. G. (1980). Photometry of a complete sample of faint galaxies. *The Astrophysical Journal Supplement Series*, 43:305.

Lucy, L. B. (1974). An iterative technique for the rectification of observed distributions. *The Astronomical Journal*, 79(6):745.

Miralda-Escudé, J. (1991). Gravitational lensing by clusters of galaxies: Constraining the mass distribution. *The Astrophysical Journal*, 370:1.

Monet, D. G., Levine, S. E., Canzian, B., Ables, H. D., Bird, A. R., Dahn, C. C., Guetter, H. H., Harris, H. C., Henden, A. A., Leggett, S. K., Levison, H. F., Luginbuhl, C. B., Martini, J., Monet, A. K. B., Munn, J. A., Pier, J. R., Rhodes, A. R., Riepe, B., Sell, S., Stone, R. C., Vrba, F. J., Walker, R. L., and Westerhout, G. (2003). The USNO-B catalog. *The Astronomical Journal*, 125(2):984.

Morganson, E., Gruendl, R. A., Menanteau, F., Kind, M. C., Chen, Y.-C., Daues, G., Drlica-Wagner, A., Friedel, D. N., Gower, M., Johnson, M. W. G., Johnson, M. D., Kessler, R., Paz-Chinchón, F., Petravick, D., Pond, C., Yanny, B., Allam, S., Armstrong, R., Barkhouse, W., Bechtol, K., Benoit-Lévy, A., Bernstein, G. M., Bertin, E., Buckley-Geer, E., Covarrubias, R., Desai, S., Diehl, H. T., GoldStein, D. A., Gruen, D., Li, T. S., Lin, H., Marriner, J., Mohr, J. J., Neilsen, E., Ngeow, C.-C., Paech, K., Rykoff, E. S., Sako, M., Sevilla-Noarbe, I., Sheldon, E., Sobreira, F., Tucker, D. L., and Wester, W. (2018). The Dark Energy Survey image processing pipeline. *Publications of the Astronomical Society of the Pacific*, 130(989):074501.

Muñoz, J. A. and Loeb, A. (2008). The density contrast of the Shapley supercluster. *Monthly Notices of the Royal Astronomical Society*, 391:1341.

Navarro, J. F., Frenk, C. S., and White, S. D. M. (1997). A universal density profile from hierarchical clustering. *The Astrophysical Journal*, 490(2):493.

NOIRLab (2014). DECam data handbook. https://noirlab.edu/science/sites/default/files/media/archives/documents/scidoc0436.pdf.

Oort, J. (1932). The force exerted by the stellar system in the direction perpendicular to the galactic plane and some related problems. *Bulletin of the Astronomical Institutes of the Netherlands*, 6:249.

Ostriker, J. P. and Peebles, P. J. E. (1973). A numerical study of the stability of flattened galaxies: or, can cold galaxies survive? *The Astrophysical Journal*, 186:467.

Pearson, D. W., Batiste, M. G., and Batuski, D. J. (2014). The largest gravitationally bound structures: The Corona Borealis supercluster - mass and bound extent. *Monthly Notices of the Royal Astronomical Society*, 441:1601.

Pearson, D. W. and Batuski, D. J. (2013). Locating bound structure in an accelerating universe. *Monthly Notices of the Royal Astronomical Society*, 436:796.

Postman, M., Geller, M. J., and Huchra, J. P. (1988). The dynamics of the Corona Borealis supercluster. *The Astronomical Journal*, 95:267.

Proust, D., Quintana, H., Carrasco, E. R., Reisenegger, A., Slezak, E., Muriel, H., Dünner, R., Sodré, L., Drinkwater, M. J., Parker, Q. A., and Ragone, C. J. (2006). Structure and dynamics of the Shapley supercluster. *Astronomy and Astrophysics*, 447:133.

Reisenegger, A., Quintana, H., Carrasco, E. R., and Maze, J. (2000). The Shapley supercluster - III. Collapse dynamics and mass of the central concentration. *The Astonomical Journal*, 120:523.

Richardson, W. H. (1972). Bayesian-based iterative method of image restoration. *Journal of the Optical Society of America*, 62:55.

Rood, H. J., Page, T. L., Kintner, E. C., and King, I. R. (1972). The structure of the Coma cluster of galaxies. *The Astrophysical Journal*, 175:627.

Rubin, V., Burstein, D., Ford, W. K., and Thonnard, N. (1985). Rotation velocities of 16 Sa galaxies and a comparison of Sa, Sb, and Sc rotation properties. *The Astrophysical Journal*, 289:81.

Rubin, V. and Ford, W. K. (1970). Rotation of the Andromeda nebula from a spectroscopic survey of emission regions. *The Astrophysical Journal*, 159:379.

Rubin, V., Ford, W. K., and Thonnard, N. (1980). Rotational properties of 21 Sc galaxies with a large range of luminosities and radii, from NGC 4605 (R = 4kpc) to UGC 2885 (R = 122kpc). *The Astrophysical Journal*, 238:471.

Rubin, V., Ford, W. K., Thonnard, N., and Burstein, D. (1982). Rotational properties of 23 Sb galaxies. *The Astrophysical Journal*, 261:439.

Ryden, B. (2003). *Introduction to Cosmology (Second Edition)*. Cambridge University Press, Cambridge, United Kingdom.

Skrutskie, M. F., Cutri, R. M., Stiening, R., Weinberg, M. D., Schneider, S., Carpenter, J. M., Beichman, C., Capps, R., Chester, T., Elias, J., Huchra, J., Liebert, J., Lonsdale, C., Monet, D. G., Price, S., Seitzer, P., Jarrett, T., Kirkpatrick, J. D., Gizis, J. E., Howard, E., Evans, T., Fowler, J., Fullmer, L., Hurt, R., Light, R., Kopan, E. L., Marsh, K. A., McCallon, H. L., Tam, R., Dyk, S. V., and Wheelock, S. (2006). The Two Micron All Sky Survey (2MASS). *The Astronomical Journal*, 131:1163.

Slipher, V. (1917). Nebulae. *Proceedings of the American Philosphical Society*, 56:403.

Small, T. A., Ma, C.-P., Sargent, W. L. W., and Hamilton, D. (1998). The Norris survey of the Corona Borealis supercluster - III. Structure and mass of the supercluster. *The Astrophysical Journal*, 492:45.

Smith, R. E., Dahle, H., Maddox, S., and Lilje, P. B. (2004). Spectrophotometric and weak lensing survey of a supercluster and typical field region - I. Spectroscopic redshift measurements. *The Astrophysical Journal*, 617:811.

Smith, S. (1936). The mass of the Virgo cluster. *The Astrophysical Journal*, 83:23.

Smoot, G. F., Bennett, C. L., Kogut, A., Wright, E. L., Aymon, J., Boggess, N. W., Cheng, E. S., de Amici, G., Gulkis, S., Hauser, M. G., Hinshaw, G., Jackson, P. D., Janssen, M., Kaita, E., Kelsall, T., Keegstra, P., Lineweaver, C., Loewenstein, K., Lubin, P., Mather, J., Meyer, S. S., Moseley, S. H., Murdock, T., Rokke, L., Silverberg, R. F., Tenorio, L., Weiss, R., and Wilkinson, D. T. (1992). Structure in the COBE differential microwave radiometer first-year maps. *The Astrophysical Journal*, 396:1.

Springel, V., White, S. D. M., Jenkins, A., Frenk, C. S., Yoshida, N., Gao, L., Navarro, J., Thacker, R., Croton, D., Helly, J., Peacock, J. A., Cole, S., Thomas, P., Couchman, H., Evrard, A., Colberg, J., and Pearce, F. (2005). Simulating the joint evolution of quasars, galaxies, and their large-scale distribution. *Nature*, 435(7042):629.

Tody, D. (1986). The IRAF data reduction and analysis system. *Proceedings of Instrumentation in Astronomy VI*, 627:733.

Tully, R. B. (1986). Alignment of clusters and galaxies on scales up to 0.1c. *The Astrophysical Journal*, 303:25.

Valdes, F., Gruendl, R., and the DES Project (2014). The DECam community pipeline. *Astronomical Society of the Pacific Conference Series*, 485:379.

Vogelsberger, M., Genel, S., Springel, V., Torrey, P., Sijacki, D., Xu, D., Snyder, G. F., Nelson, D., and Hernquist, L. (2014). Introducing the Illustris Project: Simulating the coevolution of dark and visible matter in the Universe. *Monthly Notices of the Royal Astronomical Society,*, 444(2):1518.

Walsh, D., Carswell, R. F., and Weymann, R. J. (1979). 0957+561 A, B: twin quasistellar objects or gravitational lens? *Nature*, 279:381.

Wilcoxon, F. (1945). Individual comparisons by ranking methods. *Biometrics Bulletin*, 1(6):80–83.

Zucca, E., Zamorani, G., Scaramella, R., and Vettolani, G. (1993). All-sky catalogs of superclusters of Abell-ACO clusters. *The Astrophysical Journal*, 407:470.

Zwicky, F. (1937). On the masses of nebulae and of clusters of nebulae. *The Astrophysical Journal*, 86:217.

APPENDICES
APPENDIX A
EFFECTS OF DATA CUTS

In order to determine what cutoff values gave the best results, each parameter was tested to see the effects different values. For each of the following tables, only the variable being tested is changed, and the rest are held constant. In all cases, a 12×12 grid was used. The reported scores are from method 1 in section 5.2, where the orientation of the vectors from the data and model are compared and assigned a score based on their relative alignments for each mesh element of the grid. The scale is created such that two vectors that align perfectly in the same direction are given a score of 1, vectors that are 45° apart are assigned a score of zero, and vectors that are 90° apart are assigned a score of -1.

A.1 Data Cuts for the ASC

For stars, the default value is 0.80 for $STAR\_CLASS$, and the apparent magnitude range is $17 < m < 22$. For galaxies, the default magnitude range is $21 < m < 23$ and the default $STAR\_CLASS$ cutoff is 0.4.

Table A.1: Effect of *STAR_ CLASS* cutoff for star determination in the ASC. Only objects above this threshold are counted as stars.

Minimum *STAR_ CLASS*	Number of Stars	Ellipticity Map Score	Frequency Map Score
0	13291	15.8	16.5
0.50	10597	16.6	14.9
0.60	10420	17.3	15.1
0.70	10215	16.8	15.4
0.80	9948	18.1	16.5
0.90	9494	17.6	14.9
0.95	8962	17.1	14.8

Table A.2: Effect of minimum magnitude cutoff for star determination in the ASC. The apparent magnitude range is $m_{min} < m < 22$.

Minimum m	Number of Stars	Ellipticity Map Score	Frequency Map Score
15	10890	18.6	16.2
16	10429	18.5	16.3
17	9948	18.1	16.5
18	9262	14.6	16.1
19	8336	13.8	15.8

Table A.3: Effect of maximum magnitude cutoff for star determination in the ASC. The apparent magnitude range is $16 < m < m_{max}$.

Maximum m	Number of Stars	Ellipticity Map Score	Frequency Map Score
19	1612	12.5	12.2
20	2989	16.7	13.5
21	5567	16.9	17.0
22	9948	18.1	16.5
23	13318	17.3	16.8

Table A.4: Effect of $STAR\_CLASS$ cutoff for galaxy determination in the ASC. Only objects below this threshold are counted as galaxies.

Maximum $STAR\_CLASS$	Number of Galaxies	Ellipticity Map Score	Frequency Map Score
0.10	13022	12.7	14.4
0.20	19099	15.5	16.4
0.30	22632	16.1	16.2
0.40	25292	18.1	16.5
0.50	27905	17.7	13.2
0.60	31706	17.0	12.2

Table A.5: Effect of minimum magnitude cutoff for galaxy determination in the ASC. The apparent magnitude range is $m_{min} < m < 23$.

Minimum m	Number of Galaxies	Ellipticity Map Score	Frequency Map Score
16	35062	9.9	14.3
17	34888	9.4	15.7
18	34339	8.2	16.5
19	33133	11.1	15.1
20	30504	14.1	12.7
21	25292	18.1	16.5
22	15101	10.6	13.8

Table A.6: Effect of maximum magnitude cutoff for galaxy determination in the ASC. The apparent magnitude range is $21 < m < m_{max}$.

Maximum m	Number of Galaxies	Ellipticity Map Score	Frequency Map Score
22.0	10191	11.0	8.4
22.5	17773	13.8	12.5
23.0	25292	18.1	16.5
23.5	28615	16.2	12.2
24.0	32274	17.4	12.5

While tables A.1, A.4, A.5, and A.6 each clearly show which single value gives the best result, tables A.2 and A.3 do not reveal an obvious best choice of magnitude range for star selection in the ASC. However, for the lensing analysis, a minimum apparent magnitude of 16 was selected for star determination in the ASC, as this includes more stars than a choice of 17, and avoids the odd band of stars that was noted between magnitude 15 and 16 in Figure 4.1. A maximum apparent magnitude of 22 was chosen since the score

increase on the map weighted by ellipticity outweighed the minored score decrease on the map weighted by frequency when comparing to a cutoff of 21 or 23.

A.2   Data Cuts for the MSC

For stars, the default value is 0.80 for $STAR\_CLASS$, and the apparent magnitude range is $16 < m < 20$. For galaxies, the default magnitude range is $20 < m < 24$ and the default $STAR\_CLASS$ cutoff is 0.5.

Table A.7: Effect of $STAR\_CLASS$ cutoff for star determination in the MSC. Only objects above this threshold are counted as stars.

Minimum $STAR\_CLASS$	Number of Stars	Ellipticity Map Score	Frequency Map Score
0	13877	34.7	40.5
0.50	13444	35.6	40.1
0.70	13383	35.2	39.9
0.80	13355	35.2	39.9
0.90	13292	34.2	39.8
0.95	13247	34.1	39.1

Table A.8: Effect of minimum magnitude cutoff for star determination in the MSC. The apparent magnitude range is $m_{min} < m < 20$.

Minimum m	Number of Stars	Ellipticity Map Score	Frequency Map Score
14	14448	31.5	39.9
15	14440	31.2	39.8
16	13355	35.2	39.9
17	11563	33.5	39.6
18	8808	31.0	37.5
19	5065	30.9	38.6

Table A.9: Effect of maximum magnitude cutoff for star determination in the MSC. The apparent magnitude range is $16 < m < m_{max}$.

Maximum m	Number of Stars	Ellipticity Map Score	Frequency Map Score
17	1792	37.7	43.4
18	4547	35.8	44.3
19	8288	31.7	39.6
20	13355	35.2	39.9
21	21064	31.2	39.1
22	33393	28.2	39.8
23	50284	26.7	39.3

Table A.10: Effect of $STAR\_CLASS$ cutoff for galaxy determination in the MSC. Only objects below this threshold are counted as galaxies.

Maximum $STAR\_CLASS$	Number of Galaxies	Ellipticity Map Score	Frequency Map Score
0.10	14259	21.7	29.9
0.20	20481	23.6	24.5
0.30	24642	26.6	31.0
0.40	28717	29.1	26.9
0.50	41938	35.2	39.9
0.60	69999	30.8	33.9

Table A.11: Effect of minimum magnitude cutoff for galaxy determination in the MSC. The apparent magnitude range is $m_{min} < m < 24$.

Minimum m	Number of Galaxies	Ellipticity Map Score	Frequency Map Score
15	45657	32.3	39.3
16	45135	33.1	39.4
17	44828	32.2	39.5
18	44448	29.8	38.1
19	43688	31.3	38.8
20	41938	35.2	39.9
21	38285	29.8	37.5
22	31034	25.2	29.9

Table A.12: Effect of maximum magnitude cutoff for galaxy determination in the MSC. The apparent magnitude range is $20 < m < m_{max}$.

Maximum m	Number of Galaxies	Ellipticity Map Score	Frequency Map Score
22.0	10903	22.9	32.9
22.5	16411	25.0	34.1
23.0	23263	29.4	35.0
23.5	30313	28.9	34.1
24.0	41938	35.2	39.9

While tables A.8, A.10, A.11, and A.12 each clearly show which single value gives the best result, tables A.7 and A.9 do not reveal an obvious best choice of $STAR\_CLASS$ or maximum apparent magnitude for star selection in the MSC. Since the difference in scores for a minimum of $STAR\_CLASS$ of 0.5 and 0.7 or 0.8 was small for the star selection, the value of 0.8 was chosen for the lensing analysis in order to minimize galaxy

contamination of the star sample. While a maximum apparent magnitude of 17 or 18 for star selection returned better map scores, the number of stars in the sample was insufficient to ensure that the deconvolution algorithm would run in the majority of mesh grid elements, and thus the next best value of 20 was chosen in order to include a larger sample of stars.

APPENDIX B

SCORING DIAGRAMS

Each supercluster is broken into three different grid sizes, and each grid is scored in three different ways, as specified in Section 5.2. The resulting maps are presented here.
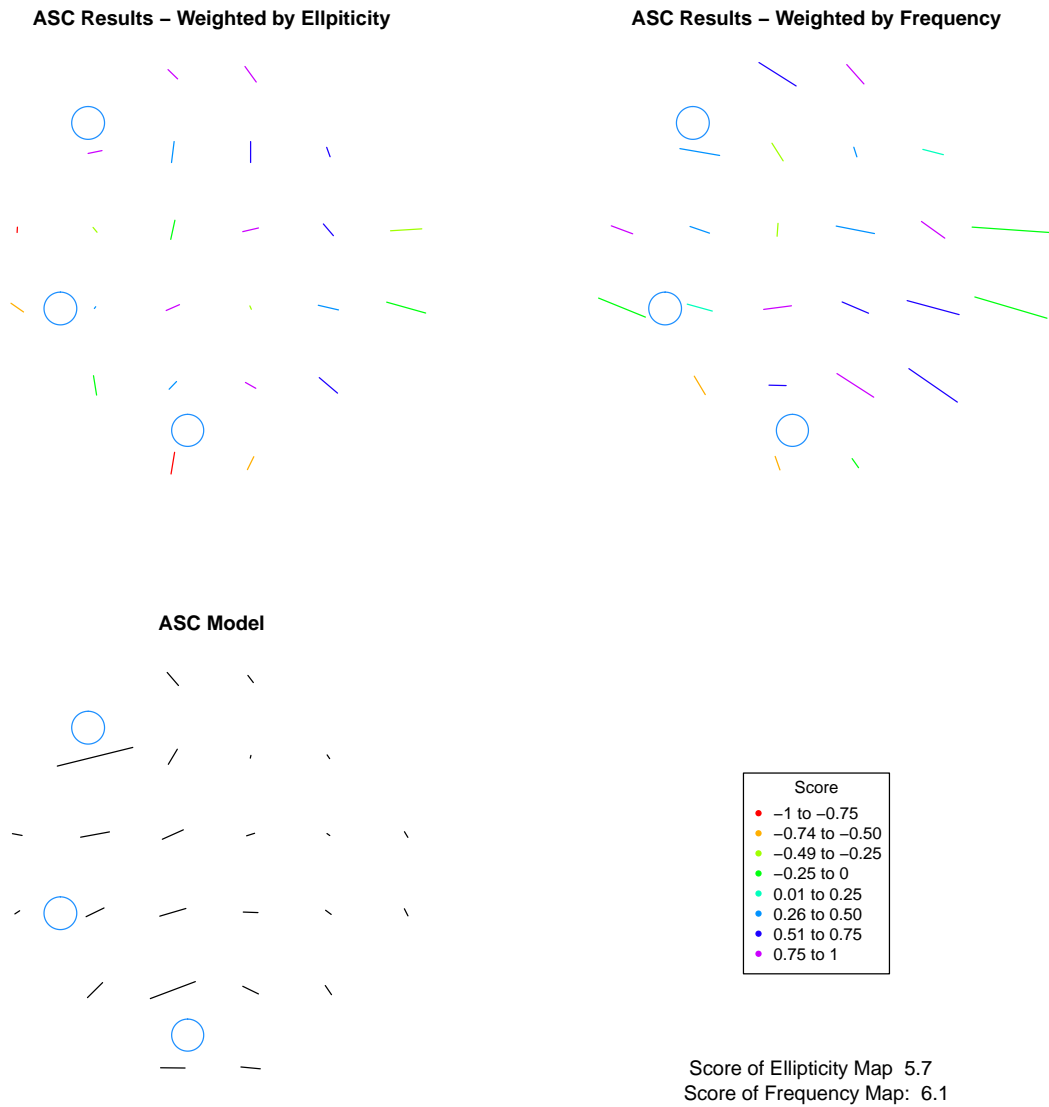
Figure B.1: The model of the ASC region broken into a 6×6 grid and comparison of data maps. Each vector is scored by how well it aligns with the direction of the vector in the same cell on the model map, with two vectors having the same alignment being given a score of 1 and two perpendicular vectors given a score of -1.

ASC Results – Weighted by Ellpiticity

ASC Results – Weighted by Frequency

ASC Model

Score
- −1 to −0.75
- −0.74 to −0.50
- −0.49 to −0.25
- −0.25 to 0
- 0.01 to 0.25
- 0.26 to 0.50
- 0.51 to 0.75
- 0.75 to 1

Score of Ellipticity Map 0.6
Score of Frequency Map: 0.7
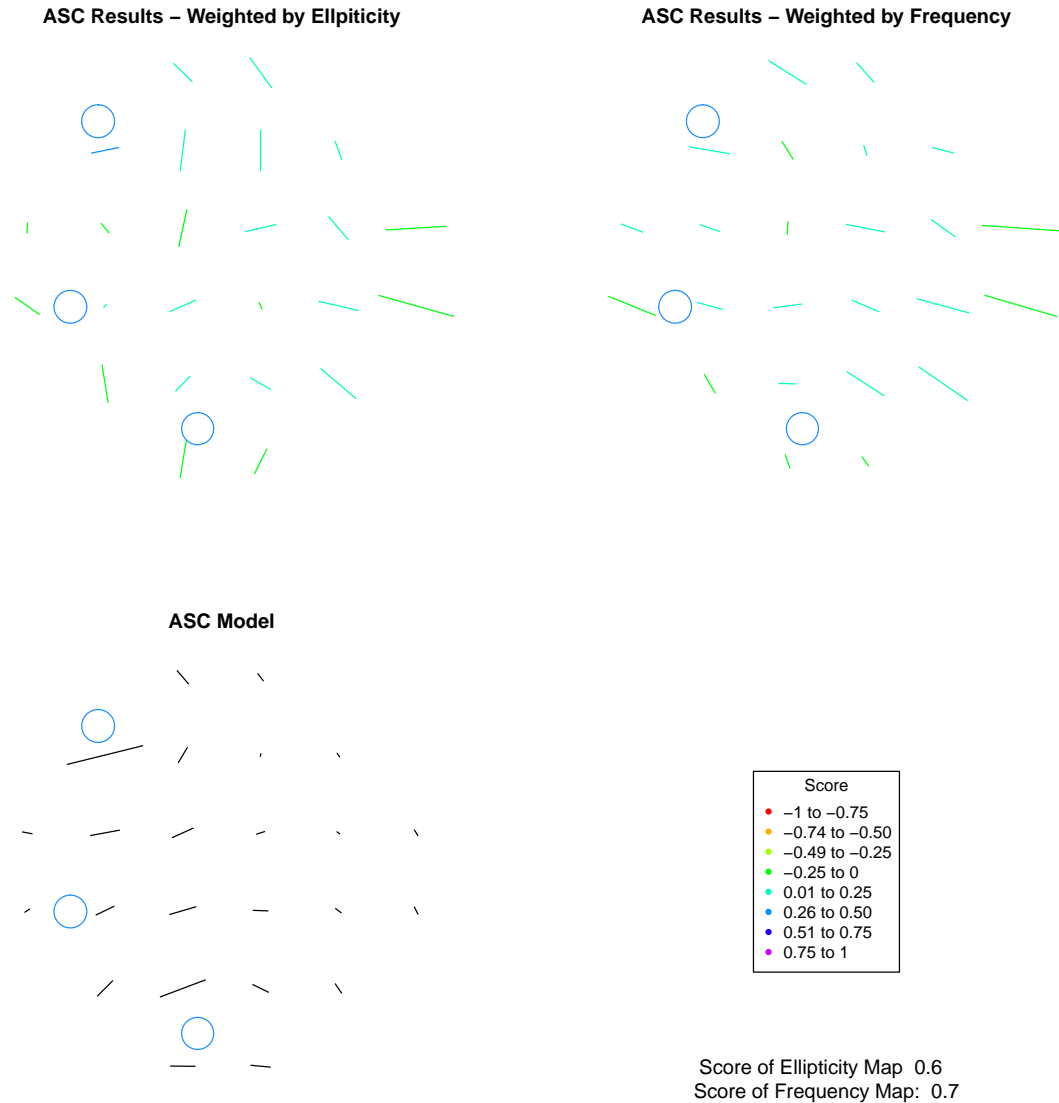
Figure B.2: The ASC region again broken into 6×6 grid. Each vector is scored by how well it aligns with the direction of the vector in the same cell on the model map, with two vectors having the same alignment being given a score of 1 and two perpendicular vectors given a score of -1, then the score is weighted by the product of the size of both vectors, where the largest vector on each graph has a size of 1.

ASC Results – Weighted by Ellpiticity

ASC Results – Weighted by Frequency

ASC Model

Score
● −1 to −0.75
● −0.74 to −0.50
● −0.49 to −0.25
● −0.25 to 0
● 0.01 to 0.25
● 0.26 to 0.50
● 0.51 to 0.75
● 0.75 to 1

Score of Ellipticity Map 1.4
Score of Frequency Map: 1.6
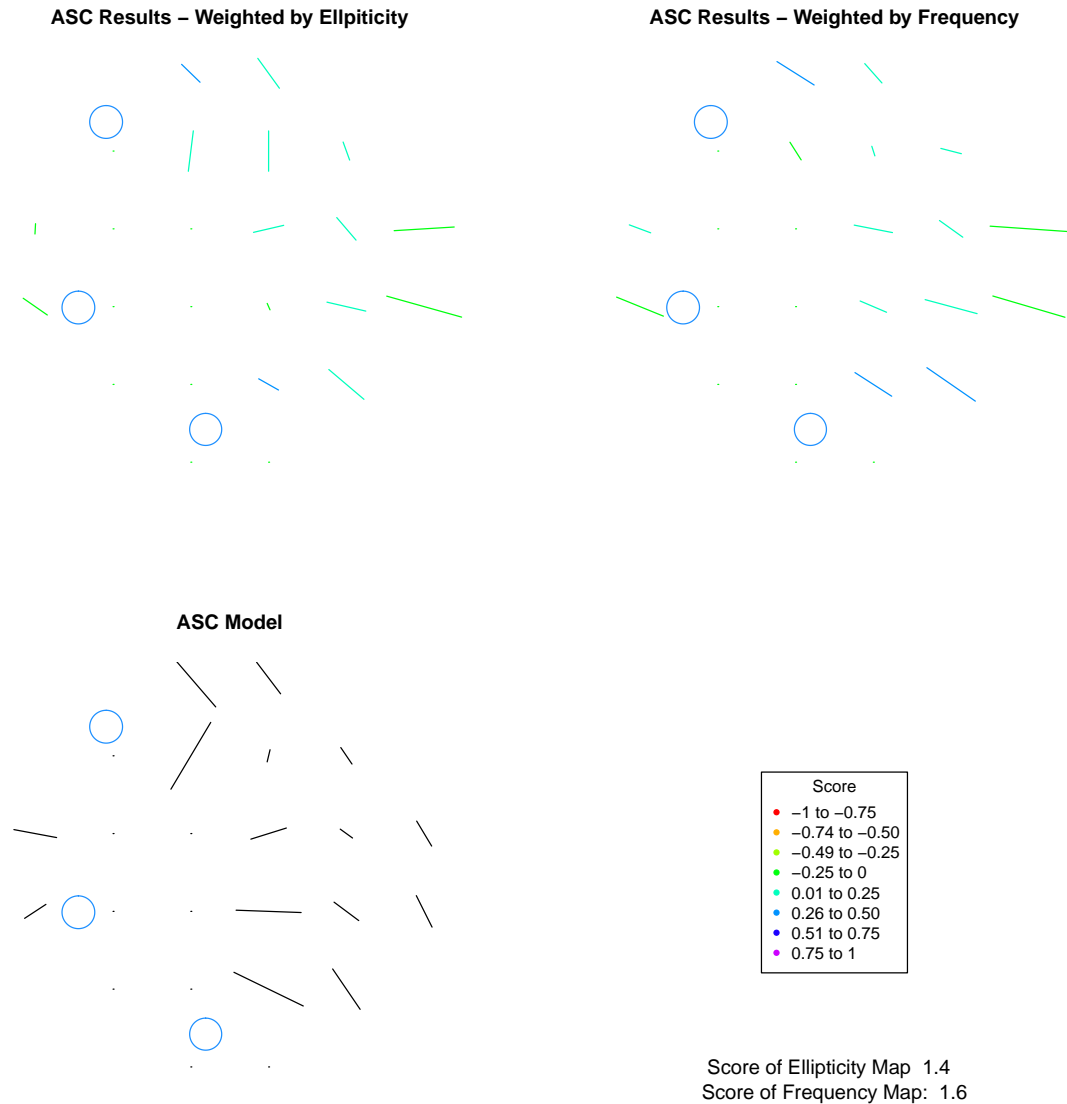
Figure B.3: The ASC region once again broken into 6×6 grid. This time the largest vectors on the model map are set to zero, and the rest of the vectors are re-scaled so that the largest again has a value of 1. Each vector is again scored by how well it aligns with the direction of the vector in the same cell on the model map, with two vectors having the same alignment being given a score of 1 and two perpendicular vectors given a score of -1, then the score is weighted by the product of the size of both vectors.

ASC Results – Weighted by Ellpiticity

ASC Results – Weighted by Frequency

ASC Model

Score
- −1 to −0.75
- −0.74 to −0.50
- −0.49 to −0.25
- −0.25 to 0
- 0.01 to 0.25
- 0.26 to 0.50
- 0.51 to 0.75
- 0.75 to 1
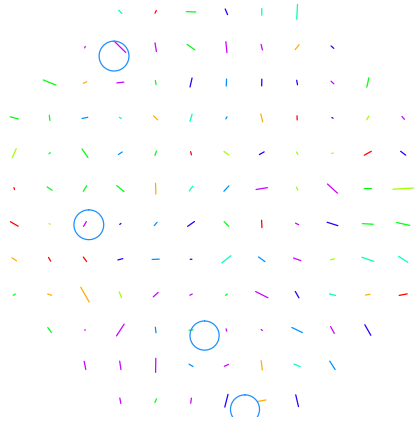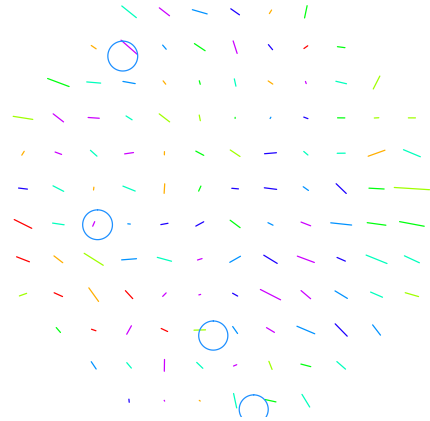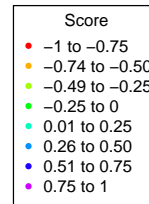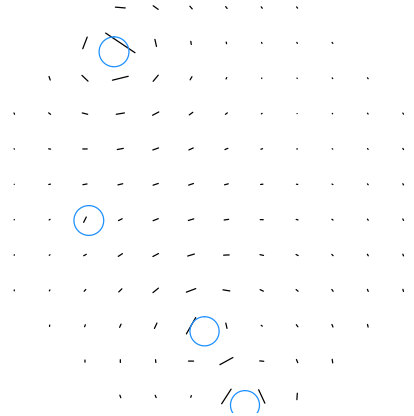
Score of Ellipticity Map 18.5
Score of Frequency Map: 16.3

Figure B.4: The model of the ASC region broken into a 12×12 grid and comparison of data maps. Each vector is scored by how well it aligns with the direction of the vector in the same cell on the model map, with two vectors having the same alignment being given a score of 1 and two perpendicular vectors given a score of -1.
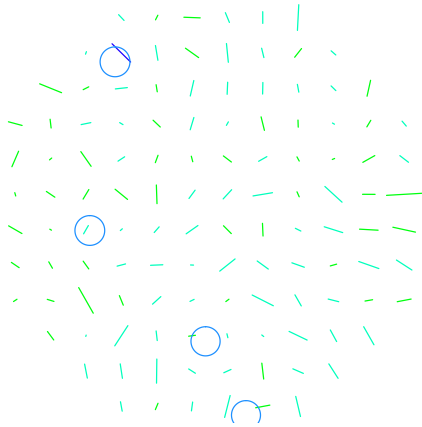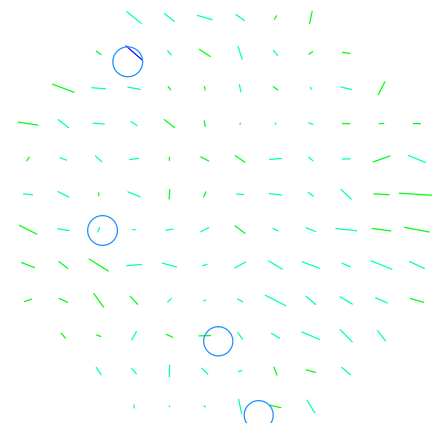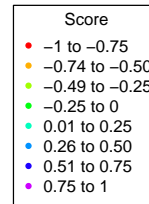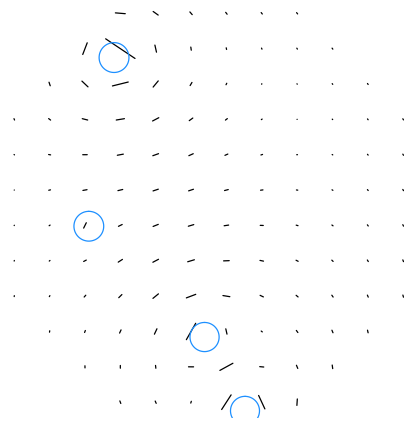
Figure B.5: The ASC region again broken into 12×12 grid. Each vector is scored by how well it aligns with the direction of the vector in the same cell on the model map, with two vectors having the same alignment being given a score of 1 and two perpendicular vectors given a score of -1, then the score is weighted by the product of the size of both vectors, where the largest vector on each graph has a size of 1.

ASC Results – Weighted by Ellpiticity

ASC Results – Weighted by Frequency

ASC Model

Score
- −1 to −0.75
- −0.74 to −0.50
- −0.49 to −0.25
- −0.25 to 0
- 0.01 to 0.25
- 0.26 to 0.50
- 0.51 to 0.75
- 0.75 to 1

Score of Ellipticity Map 3.5
Score of Frequency Map: 2.8
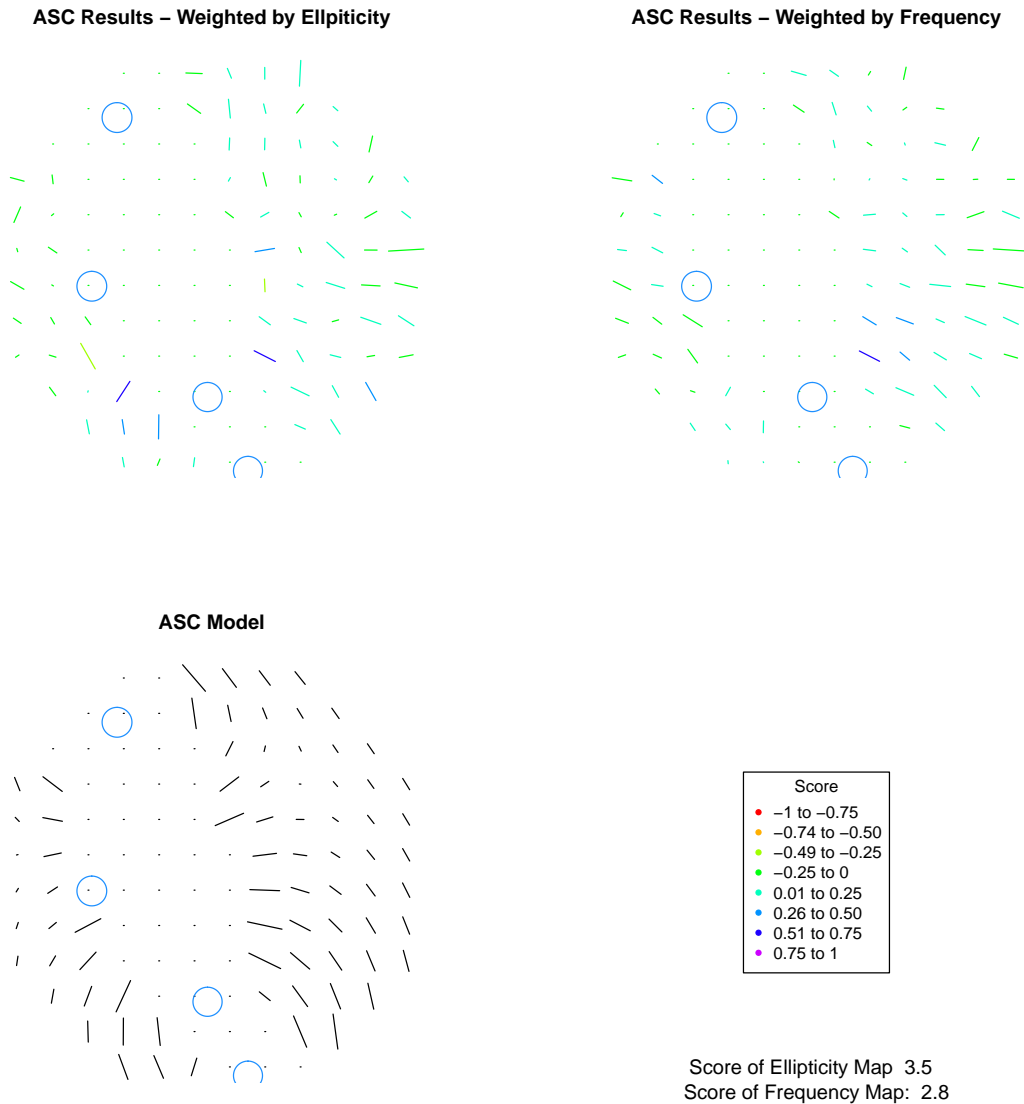
Figure B.6: The ASC region once again broken into 12×12 grid. This time the largest vectors on the model map are set to zero, and the rest of the vectors are re-scaled so that the largest again has a value of 1. Each vector is again scored by how well it aligns with the direction of the vector in the same cell on the model map, with two vectors having the same alignment being given a score of 1 and two perpendicular vectors given a score of -1, then the score is weighted by the product of the size of both vectors.

ASC Results – Weighted by Ellpiticity

ASC Results – Weighted by Frequency

ASC Model

Score
- −1 to −0.75
- −0.74 to −0.50
- −0.49 to −0.25
- −0.25 to 0
- 0.01 to 0.25
- 0.26 to 0.50
- 0.51 to 0.75
- 0.75 to 1
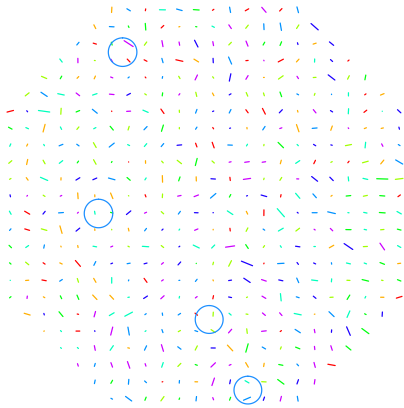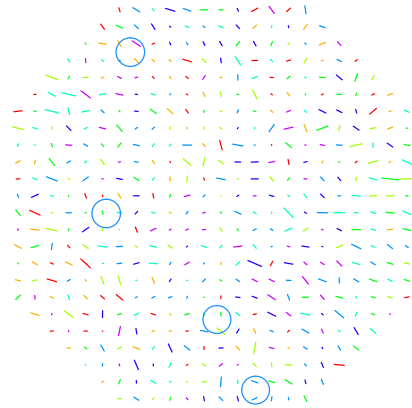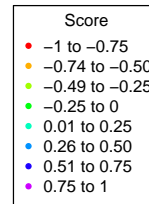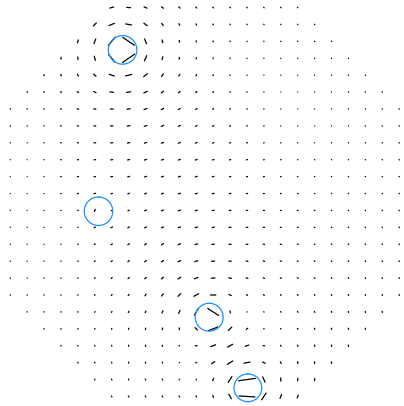
Score of Ellipticity Map 23.2
Score of Frequency Map: 14.8

Figure B.7: The model of the ASC region broken into a 24×24 grid and comparison of data maps. Each vector is scored by how well it aligns with the direction of the vector in the same cell on the model map, with two vectors having the same alignment being given a score of 1 and two perpendicular vectors given a score of -1.

ASC Results – Weighted by Ellpiticity

ASC Results – Weighted by Frequency

ASC Model

Score
- −1 to −0.75
- −0.74 to −0.50
- −0.49 to −0.25
- −0.25 to 0
- 0.01 to 0.25
- 0.26 to 0.50
- 0.51 to 0.75
- 0.75 to 1
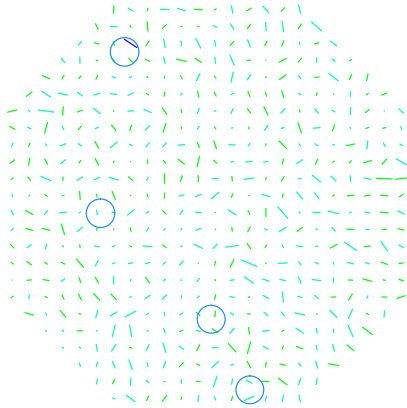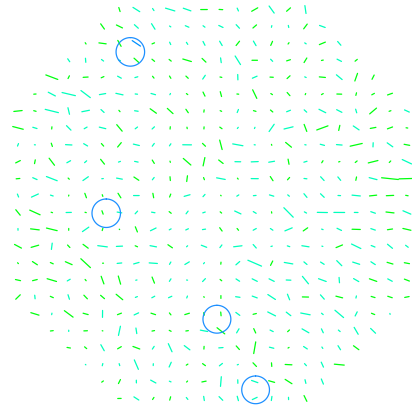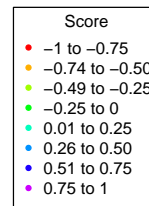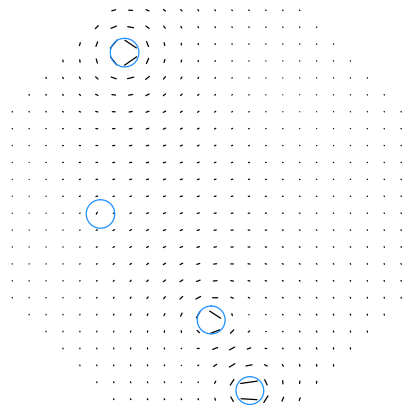
Score of Ellipticity Map 2
Score of Frequency Map: 1.2

Figure B.8: The ASC region again broken into 24 × 24 grid. Each vector is scored by how well it aligns with the direction of the vector in the same cell on the model map, with two vectors having the same alignment being given a score of 1 and two perpendicular vectors given a score of -1, then the score is weighted by the product of the size of both vectors, where the largest vector on each graph has a size of 1.

ASC Results – Weighted by Ellpiticity

ASC Results – Weighted by Frequency

ASC Model

Score
−1 to −0.75
−0.74 to −0.50
−0.49 to −0.25
−0.25 to 0
0.01 to 0.25
0.26 to 0.50
0.51 to 0.75
0.75 to 1
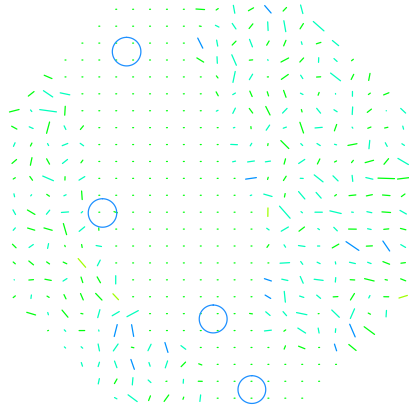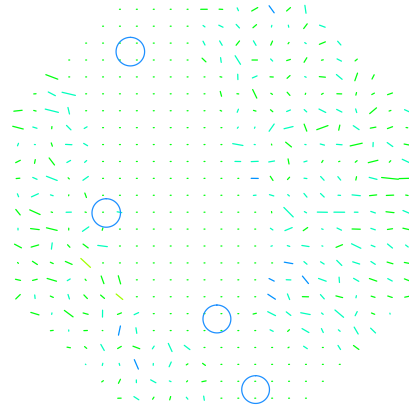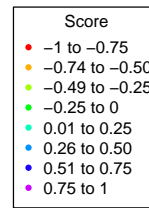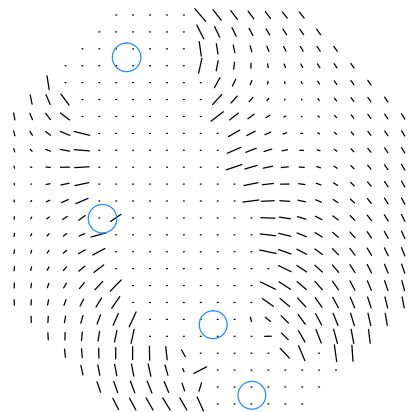
Score of Ellipticity Map 6.4
Score of Frequency Map: 4.6

Figure B.9: The ASC region once again broken into 24×24 grid. This time the largest vectors on the model map are set to zero, and the rest of the vectors are re-scaled so that the largest again has a value of 1. Each vector is again scored by how well it aligns with the direction of the vector in the same cell on the model map, with two vectors having the same alignment being given a score of 1 and two perpendicular vectors given a score of -1, then the score is weighted by the product of the size of both vectors.
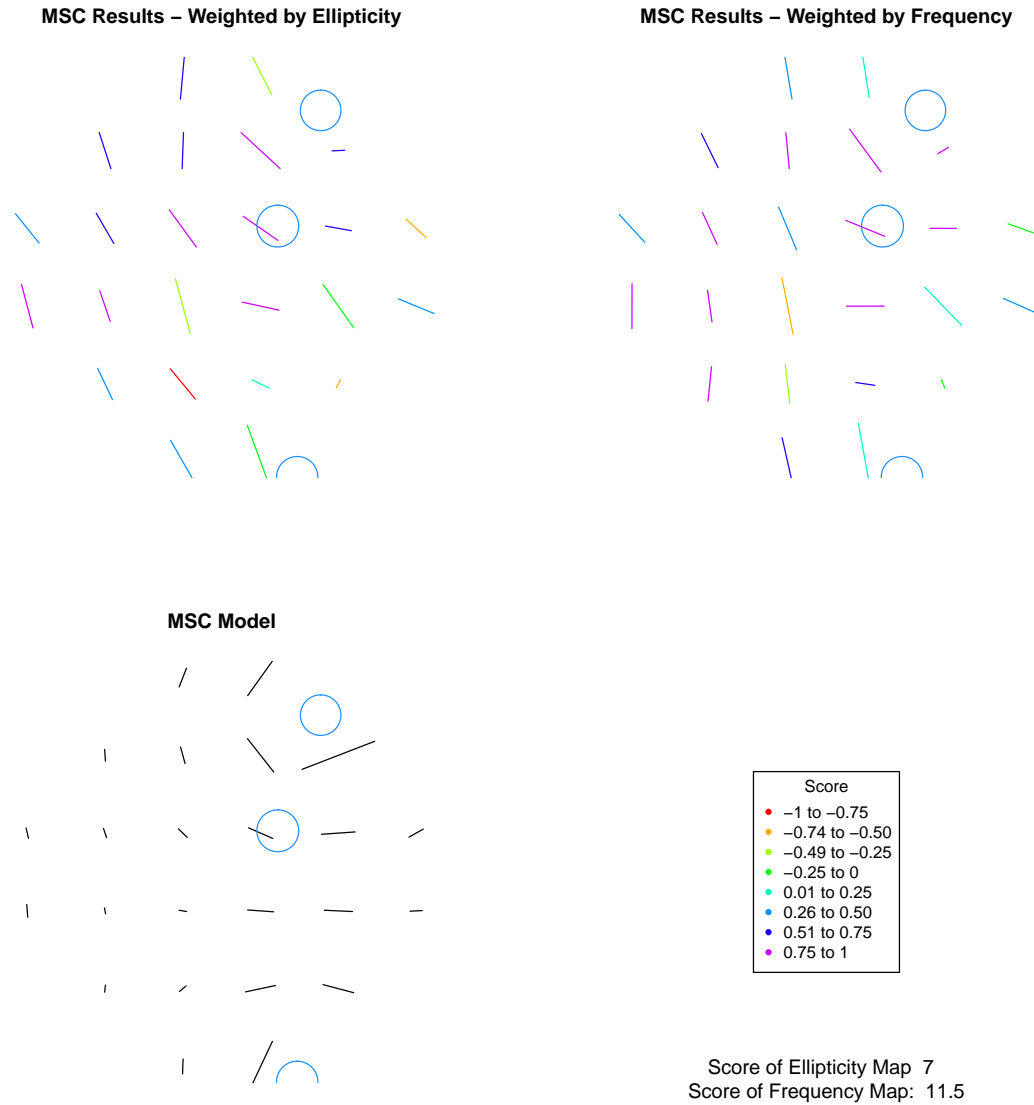
Figure B.10: The model of the MSC region broken into a 6×6 grid and comparison of data maps. Each vector is scored by how well it aligns with the direction of the vector in the same cell on the model map, with two vectors having the same alignment being given a score of 1 and two perpendicular vectors given a score of -1.

MSC Results – Weighted by Ellipticity

MSC Results – Weighted by Frequency

MSC Model

Score
- −1 to −0.75
- −0.74 to −0.50
- −0.49 to −0.25
- −0.25 to 0
- 0.01 to 0.25
- 0.26 to 0.50
- 0.51 to 0.75
- 0.75 to 1

Score of Ellipticity Map 1
Score of Frequency Map: 1.7
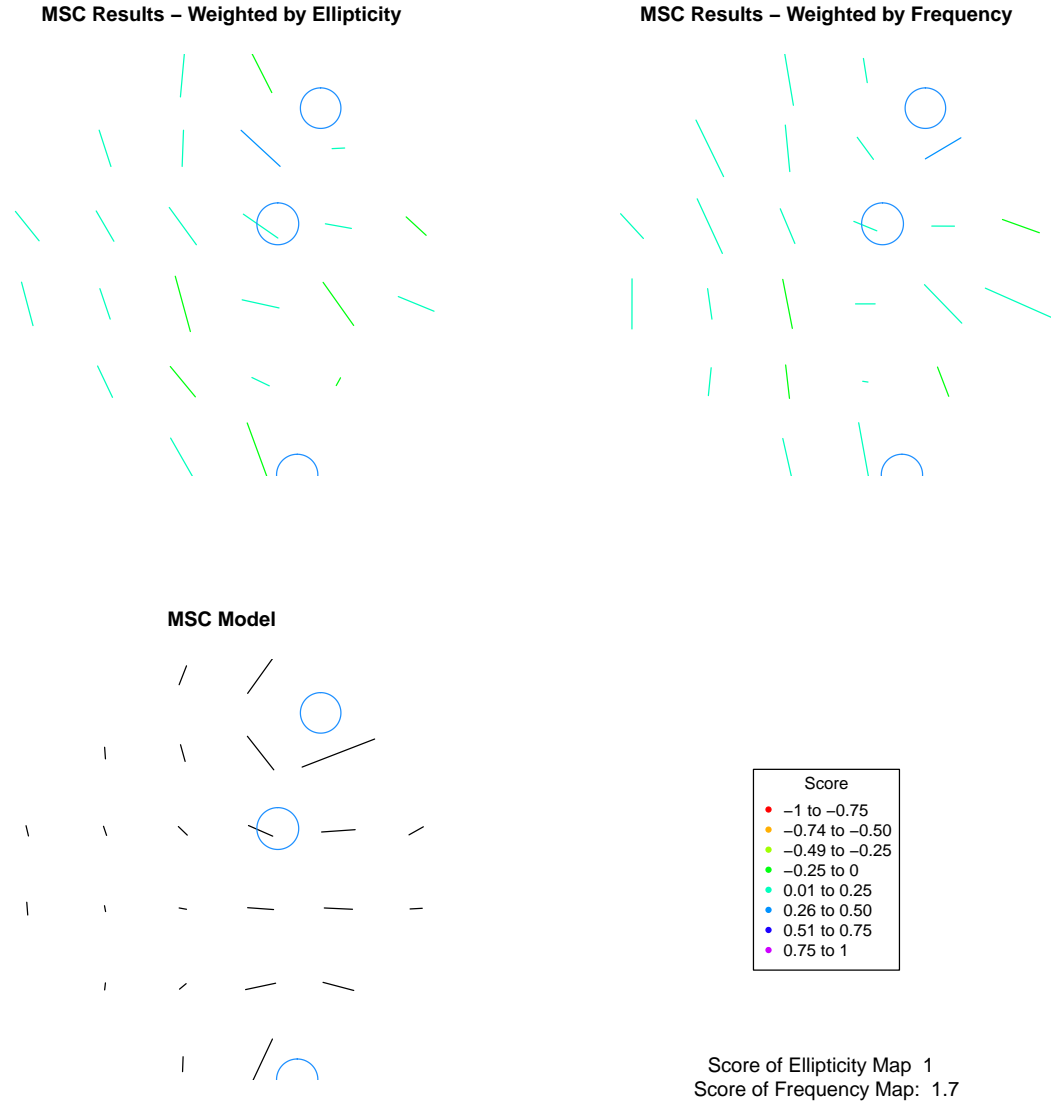
Figure B.11: The MSC region again broken into 6×6 grid. Each vector is scored by how well it aligns with the direction of the vector in the same cell on the model map, with two vectors having the same alignment being given a score of 1 and two perpendicular vectors given a score of -1, then the score is weighted by the product of the size of both vectors, where the largest vector on each graph has a size of 1.

MSC Results – Weighted by Ellipticity

MSC Results – Weighted by Frequency

MSC Model

Score
- −1 to −0.75
- −0.74 to −0.50
- −0.49 to −0.25
- −0.25 to 0
- 0.01 to 0.25
- 0.26 to 0.50
- 0.51 to 0.75
- 0.75 to 1

Score of Ellipticity Map 2
Score of Frequency Map: 2.3
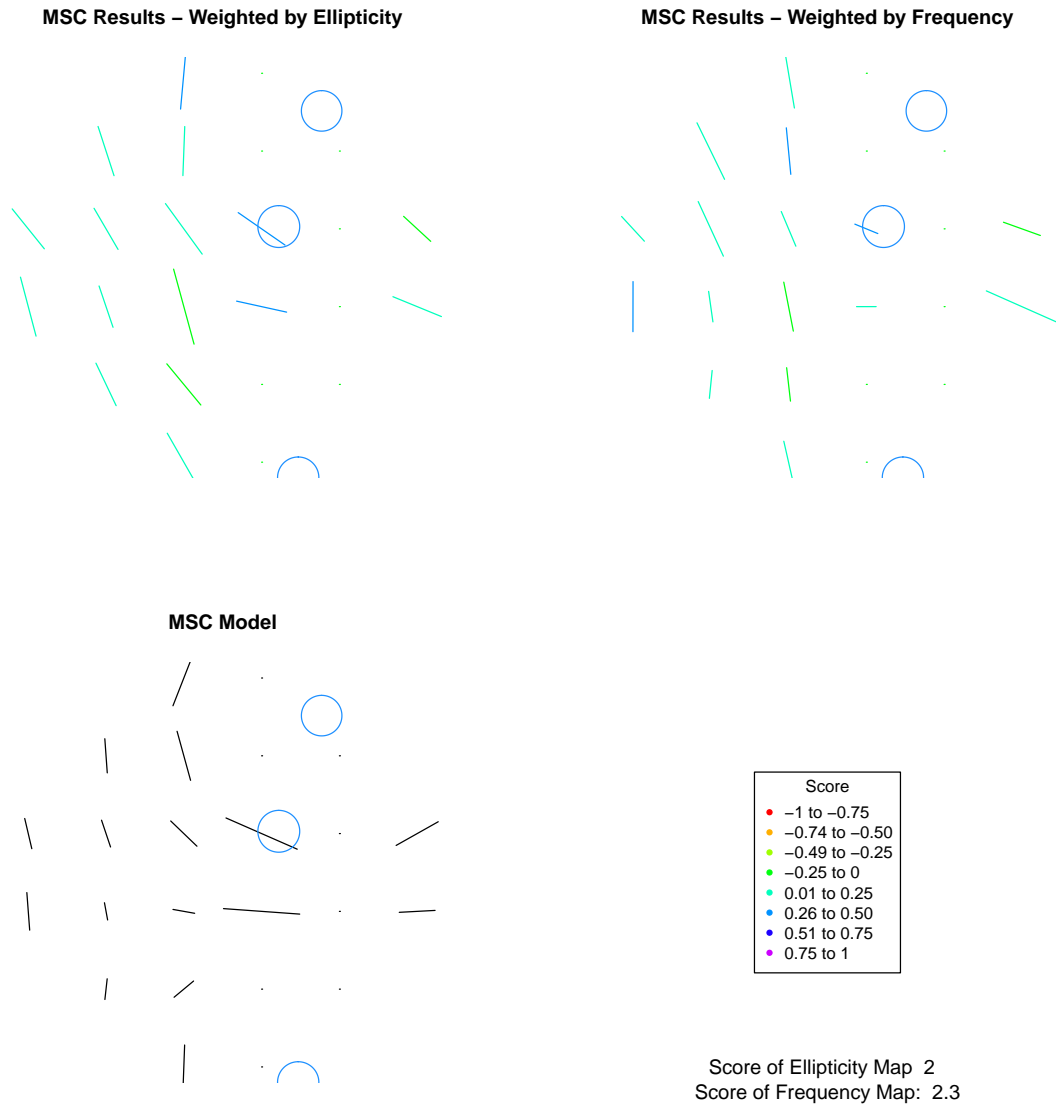
Figure B.12: The MSC region once again broken into 6x6 grid. This time the largest vectors on the model map are set to zero, and the rest of the vectors are re-scaled so that the largest again has a value of 1. Each vector is again scored by how well it aligns with the direction of the vector in the same cell on the model map, with two vectors having the same alignment being given a score of 1 and two perpendicular vectors given a score of -1, then the score is weighted by the product of the size of both vectors.

MSC Results – Weighted by Ellipticity

MSC Results – Weighted by Frequency

MSC Model

Score
- −1 to −0.75
- −0.74 to −0.50
- −0.49 to −0.25
- −0.25 to 0
- 0.01 to 0.25
- 0.26 to 0.50
- 0.51 to 0.75
- 0.75 to 1

Score of Ellipticity Map 36.8
Score of Frequency Map: 41.2
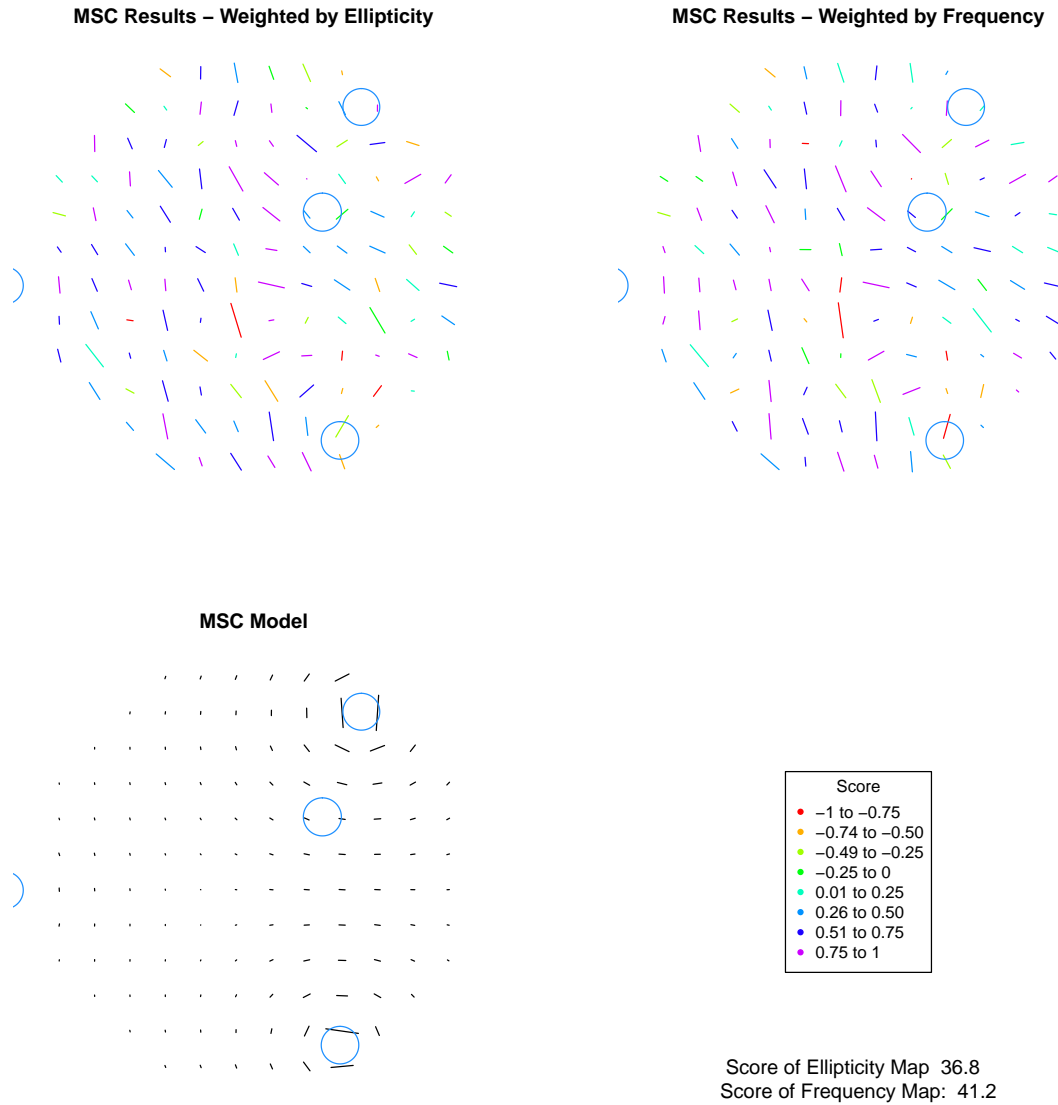
Figure B.13: The model of the MSC region broken into a 12×12 grid and comparison of data maps. Each vector is scored by how well it aligns with the direction of the vector in the same cell on the model map, with two vectors having the same alignment being given a score of 1 and two perpendicular vectors given a score of -1.

MSC Results – Weighted by Ellipticity

MSC Results – Weighted by Frequency

MSC Model

Score
- −1 to −0.75
- −0.74 to −0.50
- −0.49 to −0.25
- −0.25 to 0
- 0.01 to 0.25
- 0.26 to 0.50
- 0.51 to 0.75
- 0.75 to 1

Score of Ellipticity Map 1.3
Score of Frequency Map: 1.4
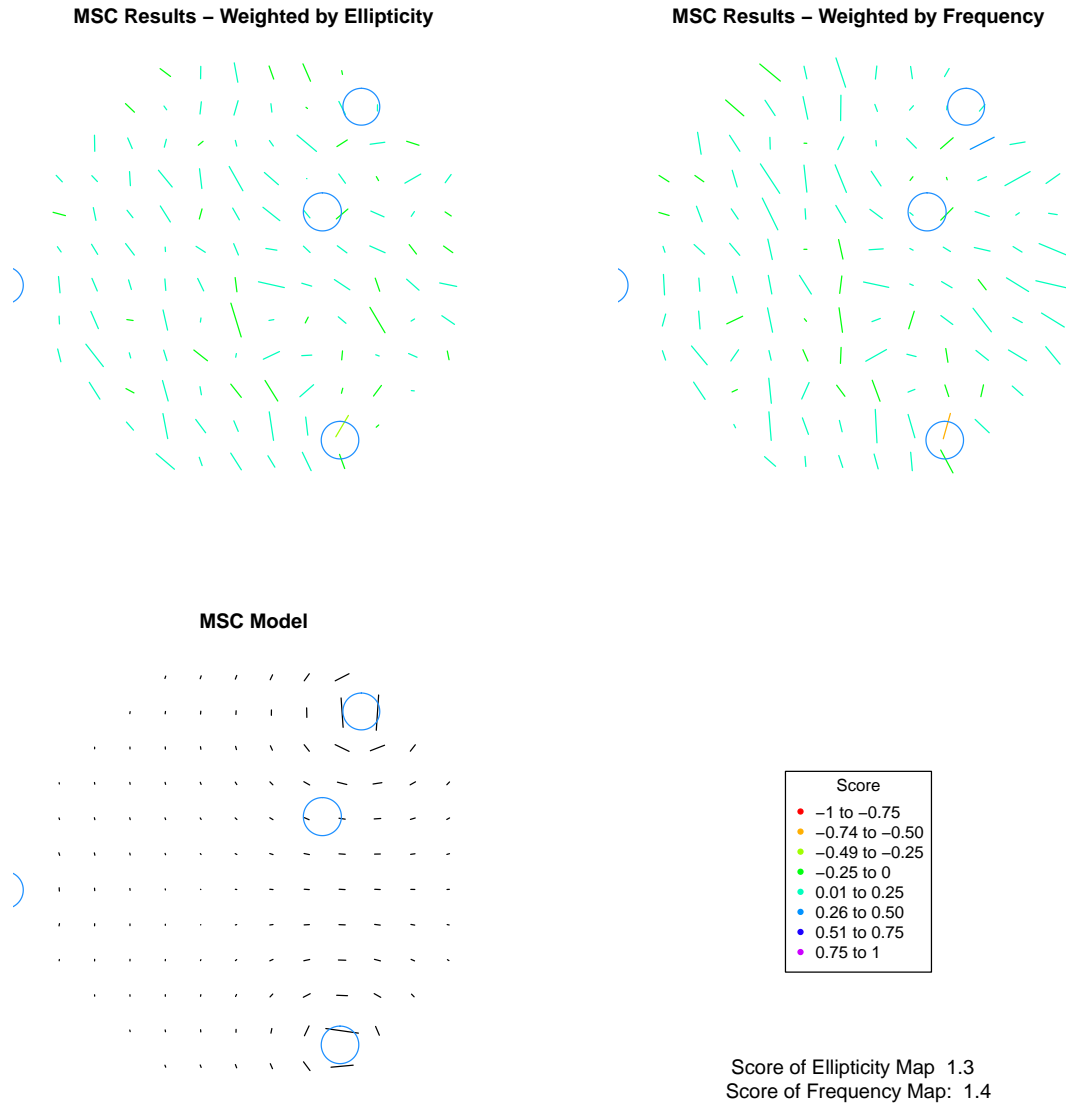
Figure B.14: The MSC region again broken into 12×12 grid. Each vector is scored by how well it aligns with the direction of the vector in the same cell on the model map, with two vectors having the same alignment being given a score of 1 and two perpendicular vectors given a score of -1, then the score is weighted by the product of the size of both vectors, where the largest vector on each graph has a size of 1.
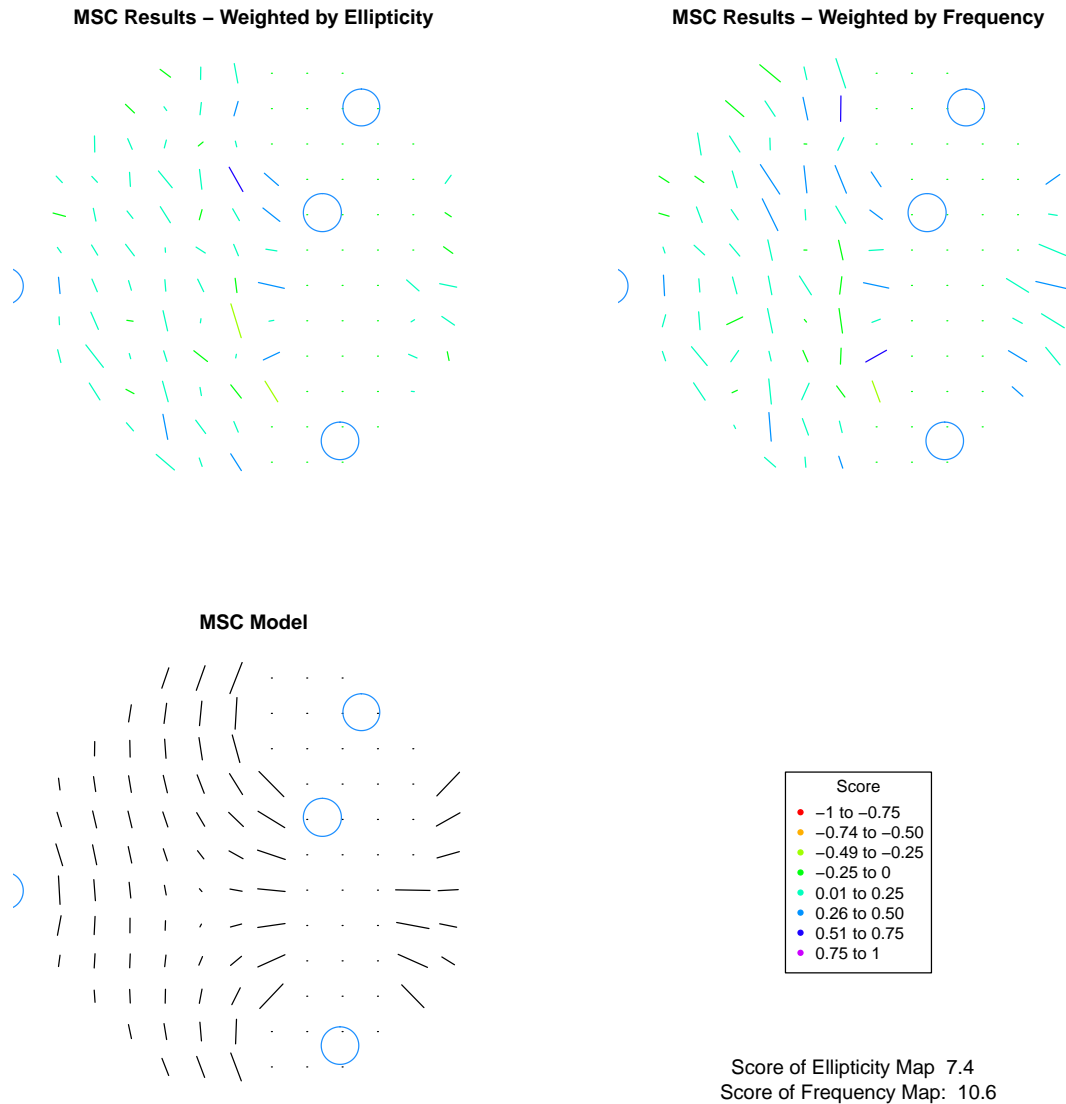
Figure B.15: The MSC region once again broken into 12×12 grid. This time the largest vectors on the model map are set to zero, and the rest of the vectors are re-scaled so that the largest again has a value of 1. Each vector is again scored by how well it aligns with the direction of the vector in the same cell on the model map, with two vectors having the same alignment being given a score of 1 and two perpendicular vectors given a score of -1, then the score is weighted by the product of the size of both vectors.

MSC Results – Weighted by Ellipticity

MSC Results – Weighted by Frequency

MSC Model

Score
- −1 to −0.75
- −0.74 to −0.50
- −0.49 to −0.25
- −0.25 to 0
- 0.01 to 0.25
- 0.26 to 0.50
- 0.51 to 0.75
- 0.75 to 1

Score of Ellipticity Map 88.4
Score of Frequency Map: 107.9
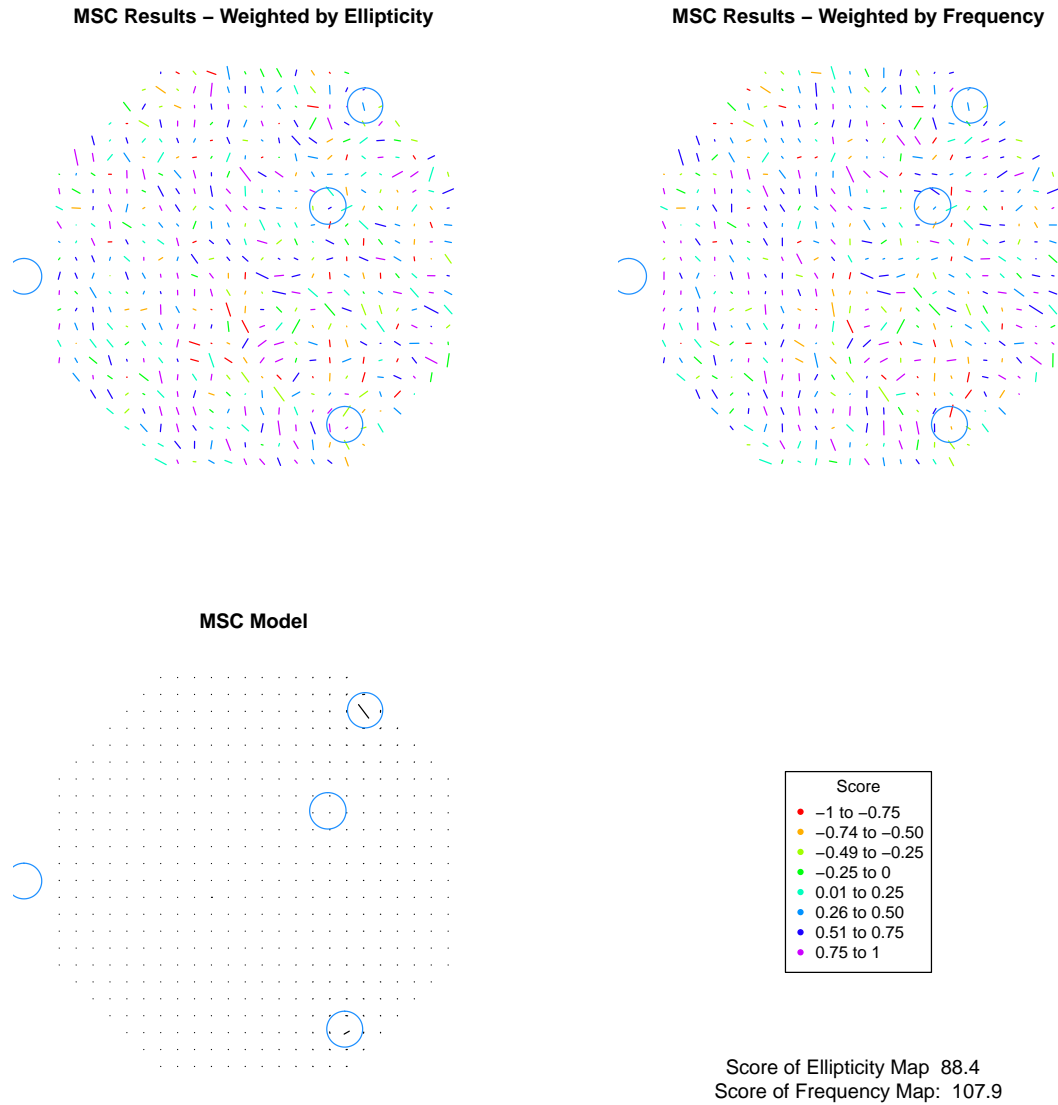
Figure B.16: The model of the MSC region broken into a 24×24 grid and comparison of data maps. Each vector is scored by how well it aligns with the direction of the vector in the same cell on the model map, with two vectors having the same alignment being given a score of 1 and two perpendicular vectors given a score of -1.
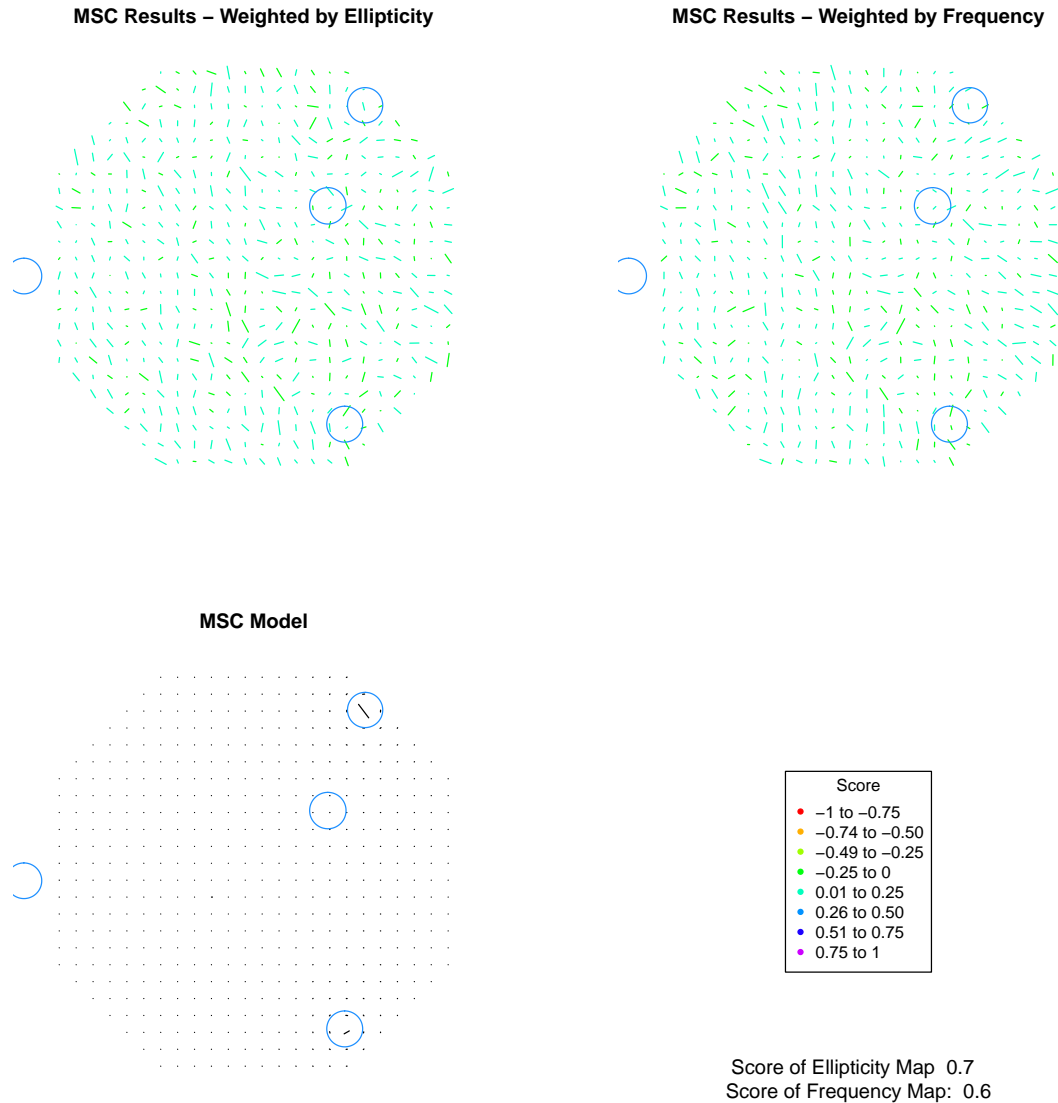
Figure B.17: The MSC region again broken into 24 × 24 grid. Each vector is scored by how well it aligns with the direction of the vector in the same cell on the model map, with two vectors having the same alignment being given a score of 1 and two perpendicular vectors given a score of -1, then the score is weighted by the product of the size of both vectors, where the largest vector on each graph has a size of 1.

MSC Results – Weighted by Ellipticity

MSC Results – Weighted by Frequency

MSC Model

Score
- −1 to −0.75
- −0.74 to −0.50
- −0.49 to −0.25
- −0.25 to 0
- 0.01 to 0.25
- 0.26 to 0.50
- 0.51 to 0.75
- 0.75 to 1

Score of Ellipticity Map 19.6
Score of Frequency Map: 22.3
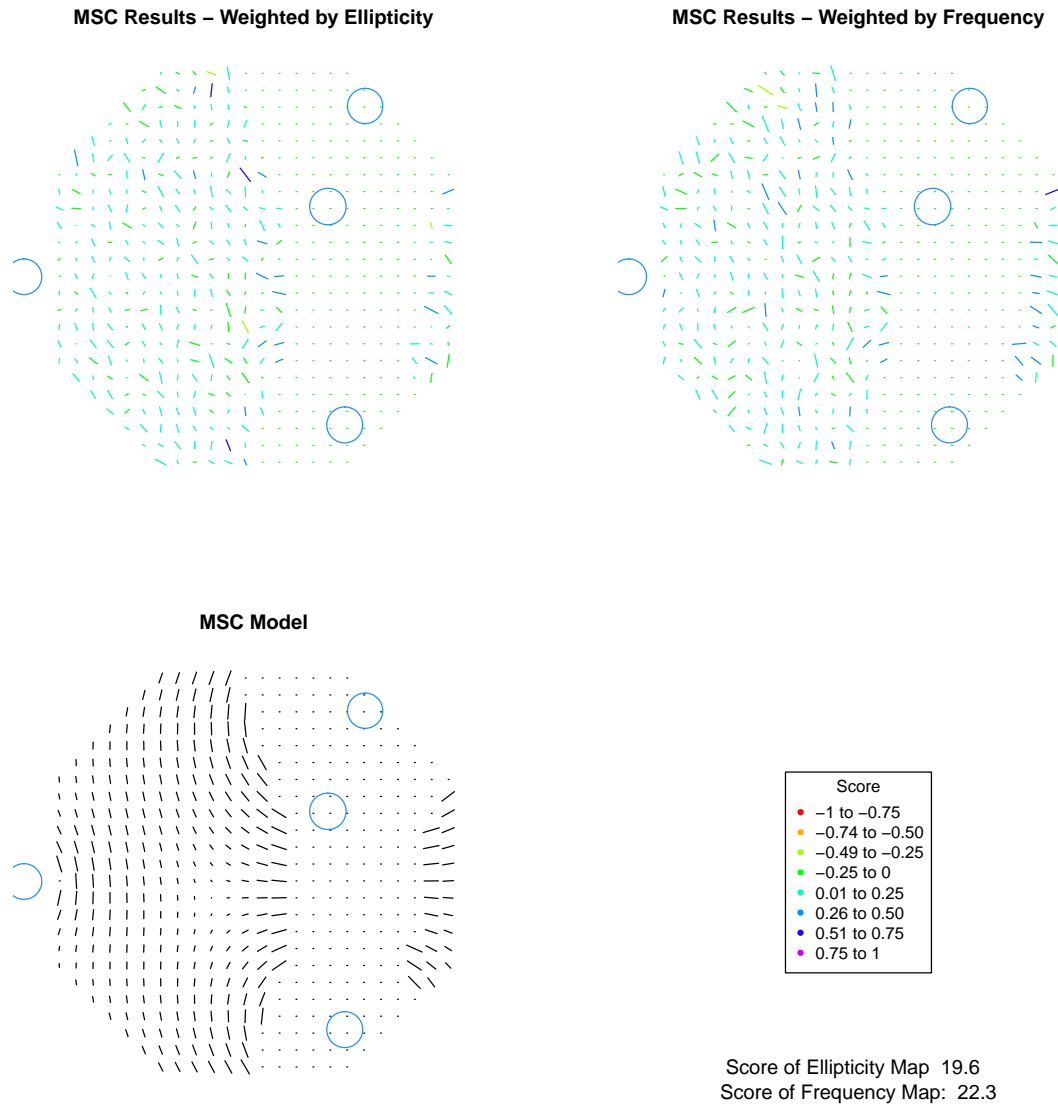
Figure B.18: The MSC region once again broken into 24×24 grid. This time the largest vectors on the model map are set to zero, and the rest of the vectors are re-scaled so that the largest again has a value of 1. Each vector is again scored by how well it aligns with the direction of the vector in the same cell on the model map, with two vectors having the same alignment being given a score of 1 and two perpendicular vectors given a score of -1, then the score is weighted by the product of the size of both vectors.

BIOGRAPHY OF THE AUTHOR

Sarah Beth Rice was born in Sidney, New York on February 1st, 1988. She grew up in the small town of Afton, New York, where she attended Afton Central School and graduated in 2006. After high school, she went on to study astrophysics at Ohio Wesleyan University in Delaware, Ohio, from which she graduated with a B.A. in 2010. She then entered graduate school in the Department of Physics and Astronomy at the University of Maine in 2011, where she decided to join the research group studying the Large-Scale Structure of the Universe with Dr. David Batuski. While a graduate student at the University of Maine, Sarah submitted an online presentation for the 2021 UMaine Student Symposium. She was also employed as a teaching assistant, granting her a wealth of experience teaching a variety of introductory level physics and astronomy courses. Sarah Beth Rice is a candidate for the Doctor of Philosophy degree in Physics from the University of Maine in December 2022.